

**Constellation-X Spectroscopy X-Ray Telescope Segmented Optic Alignment using
Piezoelectric Actuators**

by

Thomas F. Meagher

B.S. in Mechanical Engineering, June 2004, United States Air Force Academy

A Thesis submitted to

The Faculty of

The School of Engineering and Applied Science
of The George Washington University in partial satisfaction
of the requirement for the degree of Master of Science

November 18, 2005

Thesis directed by

R. Ryan Vallance

Assistant Professor of Engineering and Applied Science, Ph.D.

Report Documentation Page

Form Approved
OMB No. 0704-0188

Public reporting burden for the collection of information is estimated to average 1 hour per response, including the time for reviewing instructions, searching existing data sources, gathering and maintaining the data needed, and completing and reviewing the collection of information. Send comments regarding this burden estimate or any other aspect of this collection of information, including suggestions for reducing this burden, to Washington Headquarters Services, Directorate for Information Operations and Reports, 1215 Jefferson Davis Highway, Suite 1204, Arlington VA 22202-4302. Respondents should be aware that notwithstanding any other provision of law, no person shall be subject to a penalty for failing to comply with a collection of information if it does not display a currently valid OMB control number.

1. REPORT DATE 18 NOV 2005	2. REPORT TYPE N/A	3. DATES COVERED -	
4. TITLE AND SUBTITLE Constellation-X Spectroscopy X-Ray Telescope Segmented Optic Alignment using Piezoelectric Actuators		5a. CONTRACT NUMBER	
		5b. GRANT NUMBER	
		5c. PROGRAM ELEMENT NUMBER	
6. AUTHOR(S)		5d. PROJECT NUMBER	
		5e. TASK NUMBER	
		5f. WORK UNIT NUMBER	
7. PERFORMING ORGANIZATION NAME(S) AND ADDRESS(ES) The George Washington University		8. PERFORMING ORGANIZATION REPORT NUMBER	
9. SPONSORING/MONITORING AGENCY NAME(S) AND ADDRESS(ES)		10. SPONSOR/MONITOR'S ACRONYM(S)	
		11. SPONSOR/MONITOR'S REPORT NUMBER(S)	
12. DISTRIBUTION/AVAILABILITY STATEMENT Approved for public release, distribution unlimited			
13. SUPPLEMENTARY NOTES The original document contains color images.			
14. ABSTRACT			
15. SUBJECT TERMS			
16. SECURITY CLASSIFICATION OF:			17. LIMITATION OF ABSTRACT UU
a. REPORT unclassified	b. ABSTRACT unclassified	c. THIS PAGE unclassified	
19a. NAME OF RESPONSIBLE PERSON			

The views expressed in this article are those of the author and do not reflect the official policy or position of the United States Air Force, Department of Defense, or the U.S. Government.

ABSTRACT

The main instrument for the NASA Constellation-X x-ray observatory is the Spectroscopy X-Ray Telescope (SXT). The SXT is comprised of many thin foil closely nested segmented mirror segments. The mission design requires precise mirror alignment. The contribution of this research is towards the development of the alignment and assembly methods for the SXT optics. The method of alignment uses piezoelectric bending actuators at ten actuation points along the mirror to correct non-rigid body deformations and align the mirror segment. The design considerations of an alignment system for thin foil segmented optics using piezoelectric actuators are detailed, leading to the development of two alignment assemblies for the alignment of a single mirror segment and a mirror segment pair. The analysis of flexure design, contact stresses, piezoelectric performance, and stiffness models relating to the alignment of thin foil segmented optics is presented. The thin foil segmented optic alignment methods utilizing piezoelectric actuators are presented, including coordinate measuring machine (CMM) placement, collimated light testing, Centroid Detector Assembly (CDA) alignment, and axial interferometry. The experimental results of precise alignment using Centroid Detector Assembly feedback and piezoelectric actuators for a single mirror segment are presented. Axial interferometry is used to demonstrate the minimization of installation induced axial sag errors near the actuation points for a single mirror segment.

ACKNOWLEDGEMENTS

I would like to thank my thesis advisor, Dr. R. Ryan Vallance for his guidance, support, and knowledge throughout this project. His guidance has helped focus my efforts throughout my time and involvement at The George Washington University. I would also like to thank my academic advisor, Dr. Yin-Lin Shen, as he has provided insight and guidance throughout my Master's program.

I would like to thank all of those that have been involved with this work, as you have all helped make this possible. I would like to thank the members of the NASA Constellation-X Spectroscopy X-Ray Telescope Mechanical Design Team, including Jeff Stewart, Bobby Nanan, Ian Walker, Burt Squires, and Janet Squires. Chris Kolos allowed these designs to become a reality through all of the machining work and assembly knowledge he contributed. Dr. Scott Owens helped make the alignment work possible by working with me and passing on lessons learned from previous work. Rob Brown devoted a great deal of his time to the CMM work and alignment. Don Rencher provided support in the CAD design of the first generation assembly. Janet Squires provided finite element analysis for the reflector stiffness. Dr. Timo Saha provided insight into the optical design and application. Many other people involved with Constellation-X have provided important contributions throughout the work as well, including Dr. Will Zhang, Dr. Kai-Wing Chan, Dr. Rob Petre, Dr. Bill Podgorski, Dr. Paul Reid, Dr. John Lehan, Dave Colella, Josh Schneider, and Luis Santos. I would like to thank John Klausen of Noliac A/S for his help with the piezoelectric actuators. I would also like to thank the Diffraction Gratings Evaluation Facility (NASA/GSFC) for the use of their facilities and interferometry equipment during portions of testing.

TABLE OF CONTENTS

	<u>Page</u>
Abstract.....	iii
Acknowledgements.....	iv
Table of Contents.....	v
List of Figures.....	vii
List of Tables.....	xi
List of Acronyms.....	xii
Glossary.....	xiii
Chapter 1 Introduction.....	1
1.1 Constellation-X Mission Overview.....	1
1.2 X-ray Optics.....	2
1.3 Piezoelectric Actuators.....	10
1.4 Mirror Segment Alignment.....	17
1.5 Flexural Bearings.....	19
1.6 Thesis Overview.....	23
1.6.1 Thesis Hypothesis.....	23
1.6.2 Research Objectives.....	23
1.6.3 Research Contributions.....	24
1.6.4 Methodology.....	25
1.6.5 Remaining Chapter Summary.....	25
Chapter 2 Alignment Assembly Conceptual Design.....	27
2.1 Previous Assembly Research.....	27
2.2 Functional Requirements.....	32
2.3 Actuation Points.....	33
2.4 Actuation Stages.....	35
2.4.1 Independent Strut Design.....	36
2.4.2 Monolithic Strut Design.....	38
2.4.3 Piezoelectric Actuator Canister Assembly.....	40
2.5 Other Design Considerations.....	44
2.6 First Generation Piezoelectric Actuator Assembly.....	47
2.7 Second Generation Piezoelectric Actuator Assembly Design.....	48
Chapter 3 Mechanical Design Analysis.....	51
3.1 Glass Failure Overview.....	52
3.2 Hertzian Contact Mechanics.....	53

3.2.1 Hertzian Contact between Curved Surfaces of General Profiles.....	54
3.2.2 Force Determination for Contact Analysis.....	61
3.2.3 Glass Interface Hertzian Contact.....	62
3.2.4 Coarse Flexure Drive Coupling Hertzian Contact.....	73
3.3 Flexural Bearing Strut Design.....	76
3.4 Multilayer Piezoelectric Bender Actuators.....	83
3.5 Actuation Stage Stiffness Modeling.....	89
Chapter 4 Optical Alignment And Testing.....	98
4.1 Coordinate Measuring Machine (CMM) Alignment.....	98
4.2 Collimated Beam Testing.....	100
4.2.1 Collimated Beam Test Setup.....	101
4.2.2 Collimated Beam Test Results.....	104
4.3 Centroid Detector Assembly (CDA) Alignment.....	108
4.3.1 Mirror Segment Actuation.....	109
4.3.2 CDA Test Setup.....	112
4.3.3 CDA Alignment Test Results.....	114
4.4 Axial Interferometry.....	119
4.4.1 Axial Interferometry Test Setup.....	119
4.4.2 Axial Interferometry Test Results.....	121
4.4.3 Future Alignment Characterization.....	129
Chapter 5 Conclusions.....	130
5.1 Recommendations.....	130
5.2 Future Work.....	131
Appendix A: Matlab Scripts.....	133
A.1 Tip Design for Crossed Cylinders.....	133
A.2 Tip Design for a Sphere within a Cylindrical Race.....	135
A.3 Parallel Two-beam Flexure Strut Design.....	138
Appendix B: Actuator Movements for CDA Alignment Steps.....	141
B.1 CDA Alignment Trial 1 Movements.....	141
B.2 CDA Alignment Trial 2 Movements.....	142
Appendix C: Wiring Schematic for PPI and PPII Actuators.....	144
Appendix D: Finite Element Analysis for Azimuthal Stiffness.....	146
References.....	148

LIST OF FIGURES

	<u>Page</u>
Figure 1-1. Focusing of incident x-rays using a reflector pair.....	2
Figure 1-2. Equal-Curvature telescope design.....	3
Figure 1-3. Radial distances for 485, 489, and 494 series mirrors.....	5
Figure 1-4. Axial sag for 485, 489, and 494 series mirrors.....	6
Figure 1-5. Parameters for focal length approximation of a secondary mirror segment for a light source parallel with the optical axis.....	7
Figure 1-6. Gold-coated mirror segment pair.....	9
Figure 1-7. Constellation-X SXT modular schematic.....	10
Figure 1-8. Serial and parallel configurations of piezoelectric bending actuators.....	12
Figure 1-9. Piezoelectric bender actuator using differential voltage control.....	13
Figure 1-10. Hysteresis loop for a piezoelectric actuator.....	15
Figure 1-11. Rigid body alignment errors.....	18
Figure 1-12. Double compound rectilinear planar flexure schematic for mobility analysis.....	22
Figure 2-1. Astro-E2 telescope segmented mirror assembly.....	28
Figure 2-2. Flat glass substrate between microcombs.....	29
Figure 2-3. OAP-1 alignment assembly.....	30
Figure 2-4. OAP-2 housing with radial struts.....	31
Figure 2-5. Mirror actuation point locations.....	34
Figure 2-6. Flexure strut with integrated bonding slots.....	35

Figure 2-7. Independent strut design within a strut frame.....	37
Figure 2-8. Monolithic strut frame utilizing flexural elements.....	38
Figure 2-9. Fine-pitch adjuster interface for strut movement.....	40
Figure 2-10. Piezoelectric bender actuator canister assemblies.....	41
Figure 2-11. Test tips utilizing opposing spheres for mirror manipulation.....	42
Figure 2-12. Second generation test tips utilizing an opposing sphere and cylinder.....	43
Figure 2-13. Kinematic mount featuring three spheres within vee grooves.....	46
Figure 2-14. Vee-groove orientation with co-located optical axis and coupling centroid...	47
Figure 2-15. First generation piezoelectric actuator alignment assembly.....	48
Figure 2-16. Second generation piezoelectric actuator alignment assembly.....	49
Figure 3-1. Alignment assembly design analysis representation.....	51
Figure 3-2. Curvatures of two bodies in contact.....	55
Figure 3-3. Actuator to mirror interface tip with point contact.....	62
Figure 3-4. Hertzian contact of cylinders crossed at right angles.....	63
Figure 3-5. Maximum contact pressure for Hertzian contact of crossed cylinders.....	68
Figure 3-6. Glass tensile stress at the semimajor axis end for crossed cylinder Hertzian contact.....	68
Figure 3-7. Glass tensile stress at the semiminor axis end for crossed cylinder Hertzian contact.....	69
Figure 3-8. Hertzian contact of a sphere in a cylindrical race.....	69
Figure 3-9. Maximum contact pressure for Hertzian contact of a sphere within a cylindrical race.....	71

Figure 3-10. Tensile stress at the semiminor axis for Hertzian contact of a sphere within a cylindrical race.....	72
Figure 3-11. Sphere in spherical socket.....	73
Figure 3-12. Deformation due to an applied load for Hertzian contact of a sphere within a spherical socket.....	75
Figure 3-13. Flexural translation stage schematic utilizing two-beam, two-axis hinges....	78
Figure 3-14. Design parameters for a two-beam, two-axis flexure.....	78
Figure 3-15. Design space for the selection of the beam dimensions used in the parallel axis flexure struts for PPII.....	82
Figure 3-16. Parameters for multilayer piezoelectric actuators and the stiffness opposing actuator movement.....	86
Figure 3-17. Equivalent stiffness model for screw adjuster movement of the mirror at a single strut location.....	89
Figure 3-18. Equivalent stiffness model for CMM placement of the mirror.....	91
Figure 4-1. PPI assembly during CMM placement.....	99
Figure 4-2. Collimated beam test setup.....	102
Figure 4-3. PPI in collimated beam testing.....	102
Figure 4-4. Mirror initialization and alignment sequence.....	105
Figure 4-5. Collimated beam projections during alignment at one meter in front of the focal point.....	106
Figure 4-6. Focused and unfocused collimated beam projections at the focal point.....	108
Figure 4-7. Mirror segment coordinate system for actuator movements.....	110
Figure 4-8. Differential mode actuator movement for local cone angle change.....	111

Figure 4-9. Schematic of bench layout for CDA testing with inset of the metrology tower layout demonstrating various azimuth beam locations across an optic surface.....	113
Figure 4-10. PPI in the CDA metrology tower.....	114
Figure 4-11. Alignment trial 1 CDA spot locations for several alignment steps.....	116
Figure 4-12. Alignment trial 2 CDA spot locations for several alignment steps.....	117
Figure 4-13. Collimated beam interferometry schematic.....	120
Figure 4-14. PPI during interferometry testing.....	120
Figure 4-15. Common mode adjustment of actuators for axial figure manipulation.....	122
Figure 4-16. Axial interferometry plots for point P2.....	124
Figure 4-17. Axial interferometry plots for point P3.....	125
Figure 4-18. Axial interferometry plots for point P4.....	126
Figure 4-19. Axial interferometry plots for point P5.....	127
Figure 4-20. Axial profiles of intermediate positions.....	128

LIST OF TABLES

	<u>Page</u>
Table 1-1. Constant telescope parameters.....	4
Table 1-2. Equal-Curvature design parameters for radial distances.....	5
Table 2-1. Thermal properties of assembly materials.....	45
Table 2-2. Rigid body adjustment resolution for PPII.....	50
Table 3-1. Mirror segment stiffness results from finite element analysis (494 series secondary mirror).....	61
Table 3-2. Constants for use in contact equations [44].....	64
Table 3-3. Parameters for coefficient curve-fit equations.....	66
Table 3-4. Selected flexural element parameters for PPII flexure struts.....	83
Table 3-5. Piezoelectric actuator initial performance estimates.....	85
Table 3-6. Stiffness modeling summary for PPII actuation points.....	96
Table 4-1. Radial and axial distance values for CMM placement of the PPI 494 secondary mirror segment.....	100
Table 4-2. Focal length comparison for cone angle approximation and ray-trace analysis.	104
Table 4-3. Comparison of r_{RMS} for CDA spot returns.....	118
Table 4-4. Observed dynamic error on CDA points.....	119

LIST OF ACRONYMS

CDA	Centroid Detector Assembly
CTE	Coefficient of Thermal Expansion
EQC	Equal Curvature Design
GSFC	Goddard Space Flight Center
H	Hyperbolic (Secondary)
HXT	Hard X-ray Telescope
NASA	National Aeronautics and Space Administration
OAP	Optical Alignment Pathfinder
P	Primary (Parabolic)
P-V	Peak-to-valley
PPI	First Generation Piezo Prototype Alignment Assembly
PPII	Second Generation Piezo Prototype Alignment Assembly
SXT	Spectroscopy X-Ray Telescope
UV	Ultraviolet

GLOSSARY

1 st Order Axial Figure	- Cone angle of the optical segment
2 nd Order Axial Figure	- Curvature of the optical segment in the direction of the optical axis
Angstrom	- Measurement of length equal to 1×10^{-10} meters
Cone Angle	- Angle between the axis of rotational symmetry (optical axis) and the mirror surface
Mirror Segment	- A reflector which is an angular portion of a circular section
Optical Axis	- Central axis in the design and alignment of optical elements which are segments of a circle
Substrate	- See Mirror Segment
X-ray	- Electromagnetic radiation with wavelengths between 0.01 and 100 Angstroms

CHAPTER 1

INTRODUCTION

As the search for scientific answers about the universe continues to expand, the importance of x-ray science has in-turn increased. High-resolution x-ray spectroscopy is able to interpret cataclysmic events in the universe in ways that would not be possible with visible light alone. The study of the formation of distant stars, black holes, and galaxies will in time give us insight into the life cycle of our own planet and the matter that binds the universe.

1.1 Constellation-X Mission Overview

The Constellation-X mission is the next major x-ray observatory being developed by NASA. The purpose of the x-ray observatory is to study “black holes, Einstein's Theory of General Relativity, galaxy formation, the evolution of the universe on the largest scales, the recycling of matter and energy, and the nature of dark matter and dark energy” [1]. The spectroscopy x-ray telescope (SXT) is the main instrument portion of the Constellation-X mission. As the Constellation-X mission is the next generation of x-ray observatories, it will require capabilities 100 times that of Chandra, the last x-ray observatory from NASA, and operate in the 0.25-40 KeV band pass [2,3]. This will be achieved through large collecting areas created by many highly nested mirror segments. In order to meet the mission imaging requirements, the SXT mirror assembly requires alignment of 15 arc seconds, with a goal of 5 arc seconds [4]. In addition to the SXT, the science instruments that will be operating on the Constellation-X spacecraft include the hard x-ray telescope (HXT), x-ray micro-calorimeter spectrometer (XMS), and reflective grating spectrometer (RGS)[5, 6, 7].

1.2 X-ray Optics

The purpose of the x-ray optics is to deflect x-rays at small grazing incidence angles of less than 4° in order to focus the x-rays at a detector located at the optical focal length. The Wolter Type I design has been proven throughout x-ray astronomy as being an effective method in achieving a precise focus of x-rays and excellent image quality which utilizes parabolic and hyperbolic mirror segment pairs. Figure 1-1 demonstrates the collection of incident x-rays using this design.

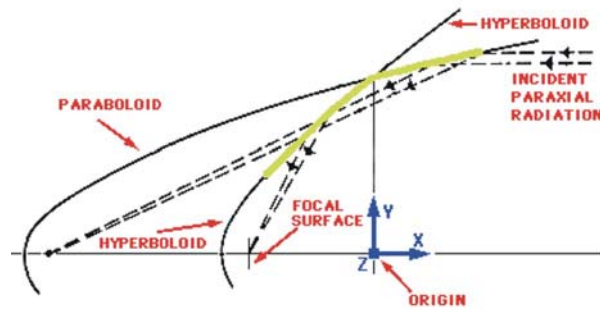


Figure 1-1. Focusing of incident x-rays using a reflector pair

The drawback to this approach is that the geometry for each of the mirrors is fairly complex and therefore increases the difficulty of creating accurate mandrels for the formation of mirror segments. Also, the on-axis image quality is typically limited by telescope manufacturing errors [8,9].

A second type of design that simplifies the mirror geometry slightly to facilitate mirror formation is the Equal-Curvature (EQC) grazing incidence telescope design. The design is a modification of the Wolter design, which still contains a primary and secondary mirror and focuses x-rays as shown in Figure 1-1, except that the mirrors are surfaces of revolution. The axial surfaces of the mirrors contain polynomial terms up to

Table 1-1. Constant telescope parameters

L_{int} (mm)	L_1 (mm)	L_2 (mm)	C_1 (mm)	C_2 (mm)
8400	200	200	26	24

The EQC telescope design is defined by spherical cross-sections, which are dependent on the axial coordinate, z_j . The radial distance from the optical axis to the mirror surface, h_j , as a function of z_j is defined by Equation (1-1) [9]. The subscript j refers to the definition of the primary ($j=1$) or secondary ($j=2$) mirror segment. The radial distance at the intersection of the primary and secondary mirror is designated as h_0 . The slope angle of the primary or secondary mirror at the primary-secondary intersection is designated as i_{0j} . R is the radius of curvature of the mirrors.

$$h_j = h_0 - R \cos(i_{0j})z_j + [R^2 - (z_j + R \sin(i_{0j}))^2]^{1/2} \quad (1-1)$$

By expanding the square root and using only up to second order terms, the surface of the mirror can be defined by a polynomial, given in Equation (1-2).

$$h_j = h_0 - \tan(i_{0j})z_j - \frac{z_j^2}{2R \cos(i_{0j})^3} \cong a_{0j} + a_{1j}z_j + a_{2j}cz_j^2 \quad (1-2)$$

The curvature of the surfaces is represented by c , which is equal to the inverse of the radius of curvature. The terms a_{0j} , a_{1j} , and a_{2j} are constants. The current mirror sizes used for alignment are designated as 485, 489, and 494 series mirrors. The designation is approximately the diameter of the circle defining the radial distance of the mirrors at the intersection of the primary and secondary mirror. Table 1-2 shows the constants necessary to determine the radial distance of a mirror using a CMM at any axial distance.

Table 1-2. Equal-Curvature design parameters for radial distances

Series Designation	485	489	494
h_o (mm)	242.7077961827	244.9221615162	247.1500617834
L_{int} (mm)	8400	8400	8400
a_{01}	2.42707941E+02	2.44922162E+02	2.47150118E+02
a_{11}	-7.22144003E-03	-7.28728629E-03	-7.35354004E-03
a_{21}	-5.00039112E-01	-5.00039829E-01	-5.00040556E-01
a_{02}	2.42707941E+02	2.44922162E+02	2.47150118E+02
a_{12}	-2.16673333E-02	-2.18649553E-02	-2.20638018E-02
a_{22}	-5.00352146E-01	-5.00358600E-01	-5.00365153E-01
C (mm^{-1})= $1/R$	2.17246397E-07	2.19225523E-07	2.21216849E-07

Figure 1-3 shows a plot of the radial distances, h_j , of the 485, 489, and 494 series mirrors corresponding to the axial distance, z_j .

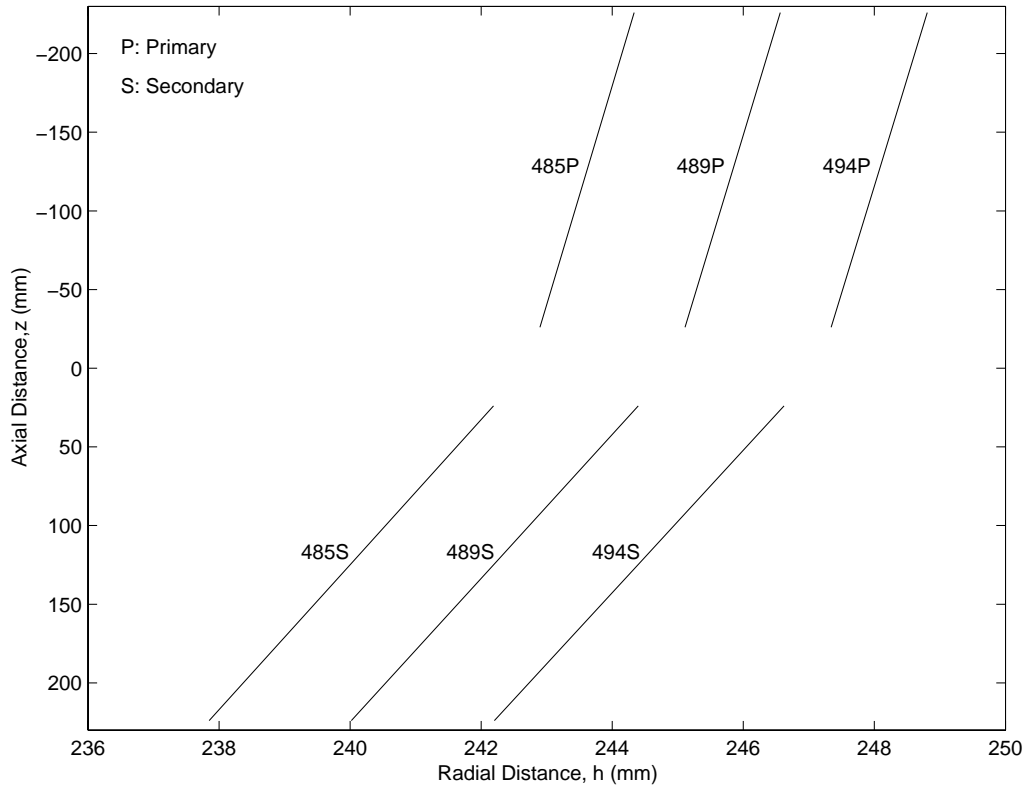


Figure 1-3. Radial distances for 485, 489, and 494 series mirrors

Figure 1-4 shows a plot of the axial sag of the 485, 489, and 494 series mirrors as a function of the axial distance, z_j . The peak to valley (P-V) of the sag is very similar for each of the mirrors, though it slightly increases from the 485 to 494 series.

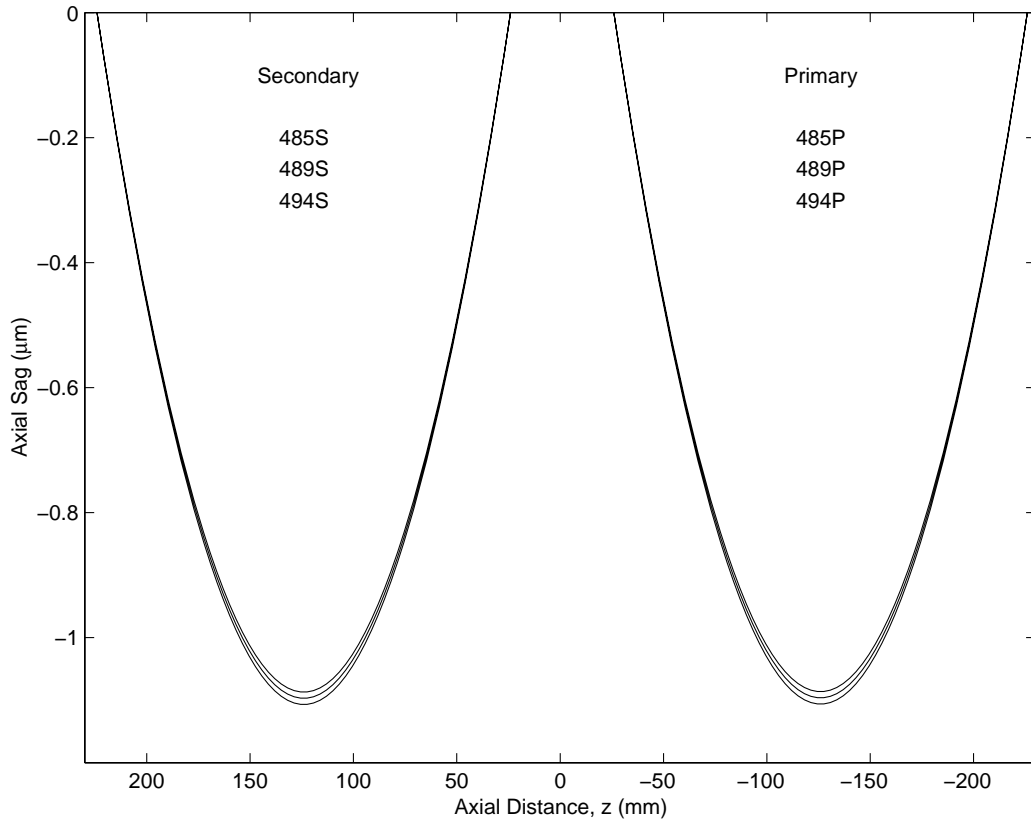


Figure 1-4. Axial sag for 485, 489, and 494 series mirrors

Since the mirror segments have axial sag of only $\sim 1.1 \mu\text{m}$ over the 200 mm axial length, they are similar to a section of a cone. A close approximation of the focal length of a single grazing-incidence mirror is related to the cone angle, ϕ , of the mirror segment and the angle of incidence of the light reflected off of it, assuming a flat mirror surface. The cone angle is the angle between the axis of rotational symmetry (optical axis) and the mirror surface. Figure 1-5 shows the parameters used for the focal length approximation using the cone angle of the optic.

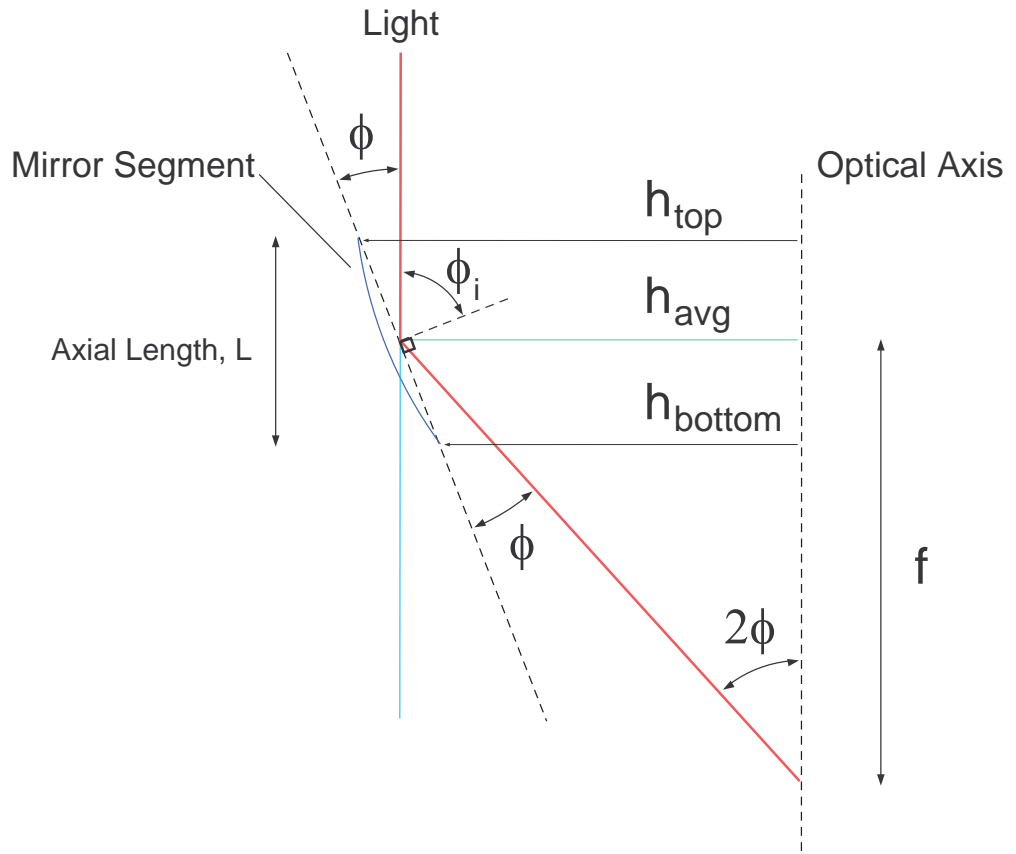


Figure 1-5. Parameters for focal length approximation of a secondary mirror segment for a light source parallel with the optical axis

The cone angle of the optic is determined by Equation (1-3), with h_{top} and h_{bottom} denoting the radial heights at the top and bottom of the mirror segment, respectively. L is the axial length of the mirror segment. The optic cone angle, ϕ , and the angle of incidence from the incoming beam, ϕ_i , are complementary angles.

$$\phi = \tan^{-1}\left(\frac{h_{top} - h_{bottom}}{L}\right) \quad (1-3)$$

Equation (1-4) is used to determine the average radial distance, which is used as the point from which the focal length is calculated.

$$h_{avg} = \left(\frac{h_{top} + h_{bottom}}{2} \right) \quad (1-4)$$

Assuming that the angle of reflection is equal to the angle of incidence, geometry then dictates that the angle of the reflected beam is 2ϕ , and the focal length can then be determined using Equation (1-5).

$$f = \frac{h_{avg}}{\tan(2\phi)} \quad (1-5)$$

The mirror segments are made of Schott D263 glass substrates with a thickness of 400 μm [10]. The mirror segments are formed through two main steps. The first step is the slumping of a flat glass sample over a convex forming mandrel made of commercial grade fused quartz by using a slow heat forming process. The second step is the epoxy-replication stage. A thin layer of epoxy (currently less than 5 μm) is uniformly sprayed over the surface of the mirror with a robotic sprayer. The epoxy layer is meant to recover surface errors produced in the initial heat forming process. The substrate with the epoxy layer is then applied in a vacuum against a replication mandrel that has been coated with a layer of gold to create the final mirror surface. The gold is used to serve as a release layer in the replication process and to act as the x-ray reflecting surface. As the forming process is refined and produces more precisely shaped mirrors, the necessary epoxy layer thickness will decrease. [11]. Figure 1-6 shows a gold-coated mirror segment pair, referring to a set of primary and secondary mirrors.

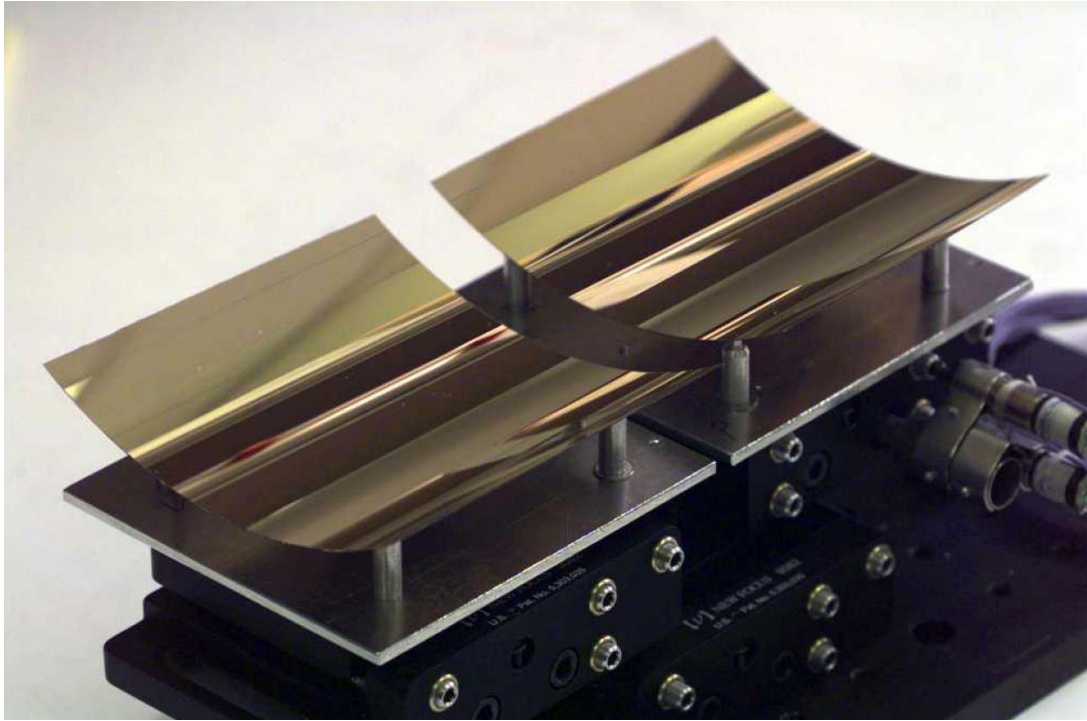


Figure 1-6. Gold-coated mirror segment pair [12]

The nested mirror segments for x-ray collection are often assembled into a housing structure for the development of the spacecraft. For the Constellation-X mission, the SXT mirror assembly is a segmented design used to house the reflections. In accordance with x-ray optics designs, the SXT is comprised of primary and secondary mirror pairs that are closely nested. Within the 1.6 m diameter of the reference design SXT, there are approximately 4000 mirror segments, which are housed in either 30-degree outer modules or 60-degree inner modules. Figure 1-7 shows the SXT mirror assembly of the segmented optics modules.

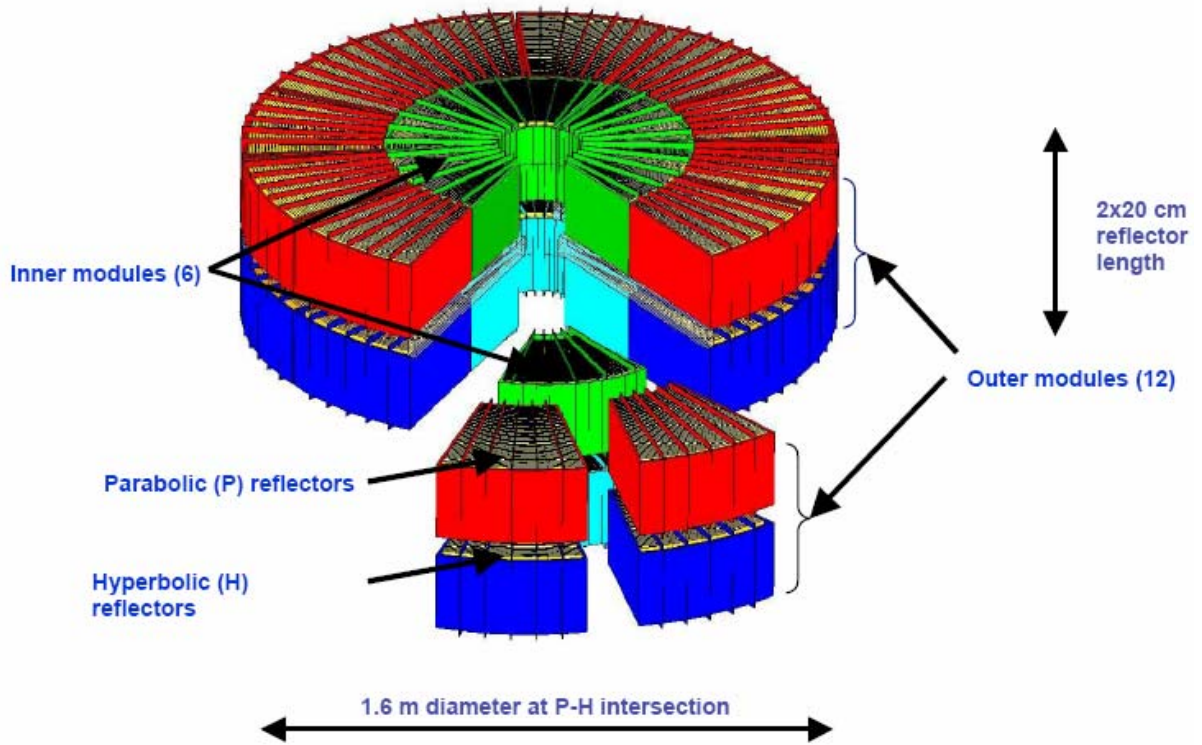


Figure 1-7. Constellation-X SXT modular schematic [13]

The reason for the modular design is to facilitate the mass production of reflectors, especially in the case of multiple spacecraft. In addition, modularity allows one section of mirrors to be installed and aligned while another module of mirrors is being assembled. As can be seen from the design, the sheer number of reflectors requires an alignment process that can be completed in a timely manner and in a closed loop fashion before the mirrors are bonded or held in the housings.

1.3 Piezoelectric Actuators

Piezoelectric actuators are based on the piezoelectric effect, which was first discovered by Jacques and Pierre Curie in 1880 when it was observed that a pressure applied to a quartz crystal created an electrical charge [14]. The inverse piezoelectric effect can also be applied, which leads to a deformation of the crystal when an electrical

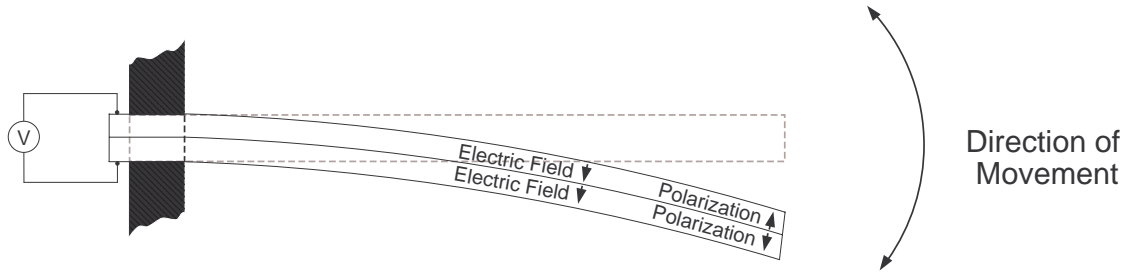
charge is applied. Since the discovery of the piezoelectric effect, many advances in piezoelectric devices have occurred, including man-made materials, uses, and configurations. Various shapes of crystals are commercially available and include plates, discs, rings, bars, rods, stacks, and plate benders.

Current piezoelectric actuators are often made of a ceramic material, such as lead-zirconate-titanate (PZT). In the formation of piezoelectric devices, the ceramic must be polarized so that the material will expand in a predictable manner and direction. This alignment of the electric dipoles is accomplished by applying a strong electric field to the piezoelectric ceramic. After the polarization is completed and the electric field is removed, the electric dipoles will remain closely aligned, which is known as the remnant polarization. When an electric field is applied by applying a voltage in the direction of polarization, the piezoelectric ceramic will expand in the direction of polarization.

The type of piezoelectric actuator used in this research is a multilayer ceramic plate bender. This is similar to a cantilever beam, as one end remains fixed, while the opposite end exhibits a deflection proportional to the applied voltage. The direction of the deflection is determined by the polarization from the applied voltage. The multilayer construction is comprised of several internal layers of piezoelectric material which is separated by internal electrodes. Piezoelectric benders are typically available in a parallel or serial configuration. In the serial configuration with two electrodes, the layers have opposite polarizations. When a voltage is applied between the piezoelectric layers, one polarization direction expands and the other contracts, which results in the bending of the beam. In the parallel configuration with three electrodes, the piezoelectric layers are polarized in the same direction. While the upper and bottom layer electrodes are

grounded, a bipolar driving voltage is applied to the middle electrode which causes the expansion and contraction of layers [15]. Figure 1-8 shows the serial and parallel configurations of a piezoelectric bender actuator with displacement.

Serial Bender Configuration



Parallel Bender Configuration

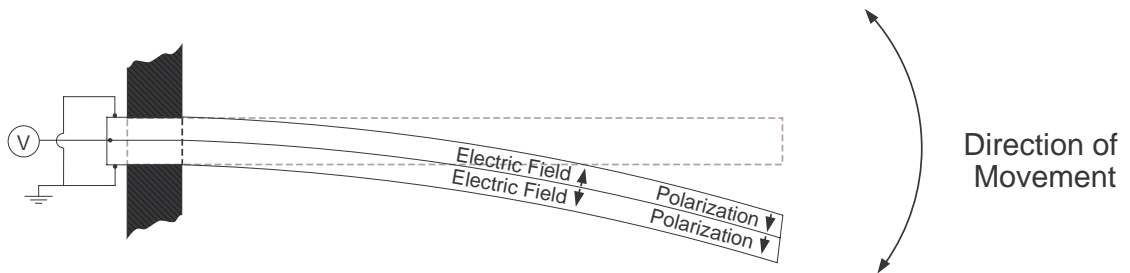


Figure 1-8. Serial and parallel configurations of piezoelectric bending actuators

In the absence of a bipolar driving voltage, differential voltage control can achieve the same effect for a parallel multilayer bender. In this configuration, two voltage sources are used. The output from one voltage source is fixed and remains on the top electrode. The output from a second source is adjustable and is placed on the middle electrode. Both of the voltage sources share a common ground on the third electrode. For a condition of zero deflection, the adjustable voltage source is set at half of the voltage for the constant voltage source and an electric field is present in the piezoelectric material. Figure 1-9 shows the motion of a parallel multilayer bender actuator operated using differential voltage control.

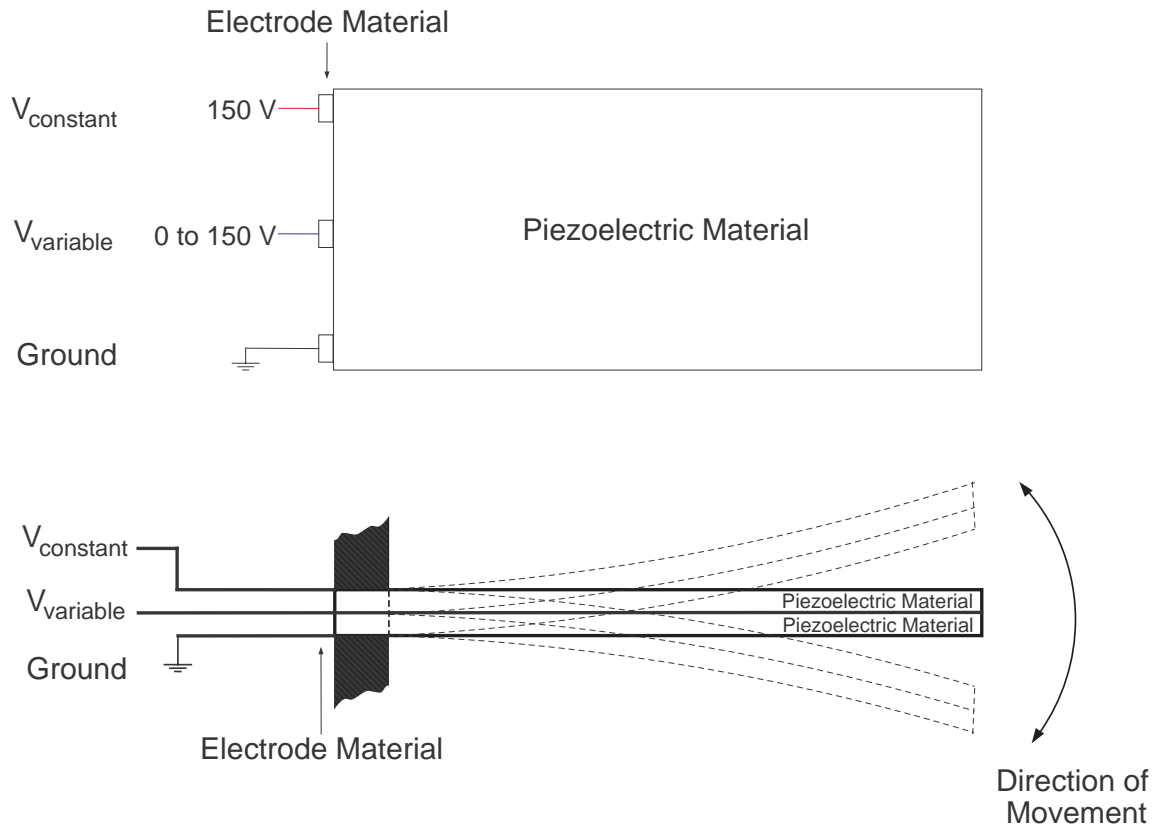


Figure 1-9. Piezoelectric bender actuator using differential voltage control

The output of a multilayer piezoelectric bender actuator that is cantilevered can be characterized by the boundary conditions imposed, tangential force opposing motion, axial load, moment applied at the end, and the voltage applied which results in an electric field across the piezoelectric material. A closer look at the governing equations to the static performance of a multilayer bender actuator will be included in a discussion in Chapter 3.

In the operation of piezoelectric actuators, a typical application may be for a desired displacement. However, the amount of force needed to generate a displacement when acting against another object results in a decrease in the maximum displacement. As a result, the amount of displacement and force produced by an actuator is dependent on the stiffness of the object opposing the force. At the maximum unconstrained

displacement, the force produced by the actuator is zero. If the piezoelectric actuator is constrained to zero displacement, the maximum amount of force, known as blocking force, is produced. The maximum effective displacement, ΔL , and force, F_{max} , that can be generated by an actuator against an object with a stiffness of k_s are given in Equations (1-6) and (1-7), respectively, where ΔL_o is the unconstrained displacement and k_{piezo} is the stiffness of the piezoelectric actuator [14]. The resulting displacement shown in Equation (1-6) is due to the stiffness of the piezoelectric actuator and stiffness of the opposing object acting as springs in parallel.

$$\Delta L = \Delta L_o \left(\frac{k_{piezo}}{k_{piezo} + k_s} \right) \quad (1-6)$$

$$F_{max} \approx k_{piezo} \Delta L_o \left(1 - \frac{k_{piezo}}{k_{piezo} + k_s} \right) \quad (1-7)$$

There are two characteristics of piezoelectric actuators that are important in precision manipulation. In open-loop operation of piezoelectric actuators, hysteresis is a characteristic that results in a motion deviation loop of up to 15% from the commanded motion. This characteristic is due to the remnant polarization of the piezoelectric actuator, which is related to the electric field applied. Therefore, the deflection and hysteretic effects depends on the field strength that the actuator was previously operated at. Figure 1-10 shows a representative hysteresis loop in the actuation of a piezoelectric actuator. A second characteristic is creep. After a voltage change, the remnant polarization continues to change and results in a slow change in displacement. The rate of creep decreases logarithmically with time and the maximum creep can amount to a few percent of the commanded motion [14].

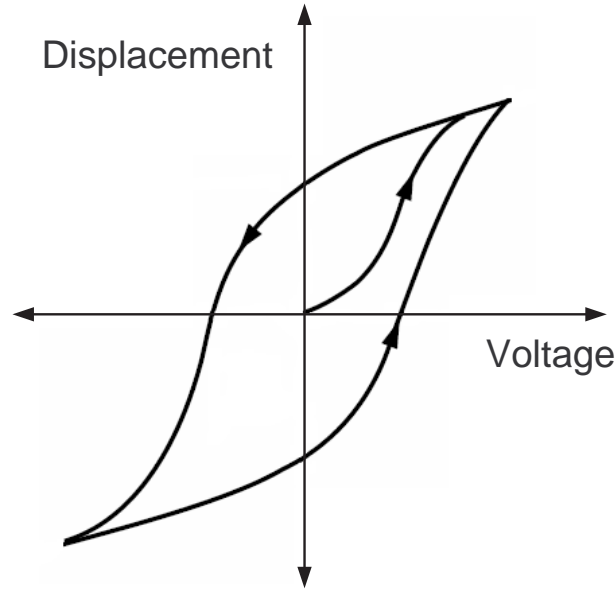


Figure 1-10. Hysteresis loop for a piezoelectric actuator

These nonlinear characteristics have an impact on their use in mirror alignment in open-loop operation. The first impact of hysteresis is that if a proper alignment is achieved, the voltage settings must remain applied. If the voltages and resulting electric field are relaxed, the actuators will not return to the same positions exactly when the original voltages are applied. The impact of creep on alignment is that the actuators position will continue to move in position after the initial position has been set. The creep as a function of time may be estimated by the displacement 0.1 s after a voltage change by Equation (1-8), where γ is the creep factor from the properties of the actuator, which is typically 0.01 to 0.02 [14].

$$\Delta L(t) \approx \Delta L_{t=0.1} \left[1 + \gamma \cdot \log\left(\frac{t}{0.1}\right) \right] \quad (1-8)$$

For optical alignments, the adverse characteristics of creep and hysteresis can be compensated for during closed-loop operation by monitoring the feedback and adjusting the piezoelectric voltages accordingly.

The alignment of thin foil optics is sensitive to thermal changes. As a result, the heat generation of any alignment mechanism should be considered. For the case of piezoelectric actuators, the power that is converted to heat is dependent on the frequency and amplitude of the voltage changes needed for actuation. Equation (1-9) shows the power converted to heat for a given dynamic voltage change, where $\tan \delta$ is the dielectric loss factor for the actuator, f is the frequency, C is the actuator capacitance, and U_{p-p} is the peak to peak voltage [14]. Since the loss factor is typically on the order of 1-2% and the frequency of driving voltages was limited by the user input of movements every several minutes, the heat generation was negligible for the testing completed. However, for a closed-loop operation with multiple mirror segments and actuators running simultaneously, the heat generation should be investigated further, keeping in mind that the resulting temperature distribution will be a function of the thermal resistance and boundary conditions for conduction, convection, and radiation heat transfer during ground assembly.

$$P \approx \frac{\pi}{4} \tan \delta \cdot f \cdot C \cdot U_{p-p}^2 \quad (1-9)$$

The resolution of a piezoelectric actuator is typically limited by a few factors, including the voltage noise of the controlling amplifier, which creates unwanted movement. Also, the sensors used for positioning feedback will have a noise level and sensitivity that will limit the positioning resolution. For the testing completed in aligning a mirror segment, the smallest positioning feedback voltage step size was 0.1 volts, whereas the error noise from the Thor Labs MDT693A voltage sources is only 1.5

millivolts RMS [16]. Therefore, the controlling amplifier error noise was negligible, as the alignment capability was limited by the alignment and positioning feedback.

1.4 Mirror Segment Alignment

The alignment of thin foil mirror segments is comprised of the correction of rigid body and optical segment (non-rigid body) errors. The rigid body errors deal with the misalignment of the entire optic with relation to the optical axis and the other optical elements. The first rigid body error is axial position error which occurs when interfaces supporting the optic are not at the correct axial positions. The second rigid body error is a radial position error, which occurs when the radial centers of the optics are not at the correct placement from the optical axis. This is also referred to as a de-center error. The tangential tilt error is when the cone angle of the entire optic is incorrect with respect to the optical axis for a given segment. For future references, the adjustment made for the correction of tangential tilt will be referred to as the *tip* of the optic. There are two radial tilt errors. The first radial tilt error is for a single optic about the center of the optic. The second radial tilt is a relative tilt error, which is when the tilt of one segment relative to the other differs. The rotation for a relative tilt error can result from a single optic radial tilt or from a rotation about the intersection between the primary and secondary mirror, as shown. Figure 1-11 shows a diagram representing the rigid body alignment errors [12]. The other possible rigid-body errors, as shown, are the axial tilt error and tangential position error.

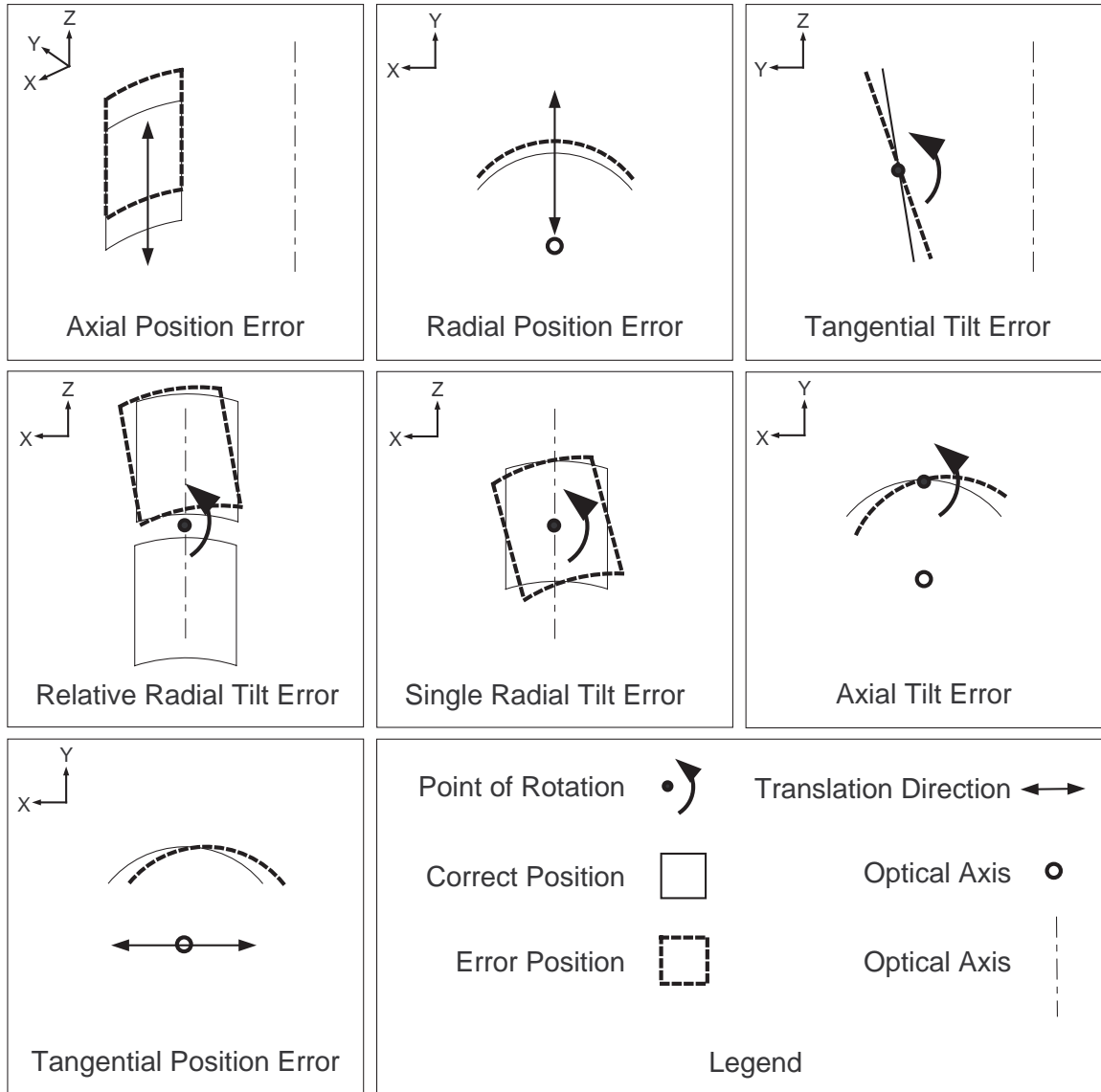


Figure 1-11. Rigid body alignment errors

The optical segment errors represent the second set of alignment errors due to installation. The first segment error is an average radius error. This error is the difference between the average segment radii when compared with the optical design of the mirror segment. The second segment error is a delta radius error, which is a difference in the average radii between the top positioning points on the mirror and the bottom positioning points. These errors are errors in the cone angle on the optic. The third segment error is the random radial errors of the positioning points with respect to

the optical axis. This is the difference between the design radius and the actual radius at each of the positioning points [12]. Another important error within the segment with regards to the alignment is the axial figure error. The axial figure error is primarily determined during the mirror formation. However, current SXT work has shown that the axial figure is likely affected by the installation of the optics as well as the manner in which it is held.

The correction of rigid body and figure alignment errors is necessary for an effective functioning assembly. The primary purpose of the piezoelectric actuators is to correct the optical segment errors. The use of actuators at the center top and bottom actuators of the mirror also allows for small corrections in rigid body errors, such as the radial position and tangential tilt error. The axial position error and radial tilt errors are controlled by the adjustment of the support points for the housings of the mirror segments. The initial radius placement is used to minimize axial tilt and tangential position error.

1.5 Flexural Bearings

The use of piezoelectric actuators for the mirror alignment allows very precise motions as allowed by the resolution of the power supplies and positioning feedback. However, this precise motion comes at a cost of limited travel. Therefore, it is necessary to have a coarse actuation stage which allows for greater travel in the positioning of the actuators and mirror. This coarse travel is desired to be linear and only translate in the radial direction with respect to the mirrors. Flexure design provides a novel approach to creating a coarse alignment stage which allows for straight line motion. Flexural bearings take advantage of the bending and/or torsion of solid elements throughout the

material's elastic range to provide precise and predictable motions [43]. Several advantages and disadvantages of flexures include [46]:

Advantages

- Simple and easier assembly
- Allows for a monolithic design, eliminating the need for tight tolerances
- Are wear-free as long as fatigue cracks do not develop
- Smooth, continuous, and repeatable displacements
- Symmetric designs allows for thermal stability
- Linear relationship between force and displacement
- No friction
- No hysteresis

Disadvantages

- Potential for discrepancies between predicted and actual performance due to manufacturing tolerances
- High stresses may induce hysteresis in the stress-strain behavior
- Restricted translation for a given flexure size
- Out of plane stiffness may be low compared with other bearing systems
- Flexures may exhibit complete failure from overloading

In the design of flexure systems, it is useful to analyze the mobility of a given system in order to ensure that the desired degrees of freedom are achieved. This mobility analysis is accomplished by modeling the flexural system as a number of links and joints with a certain number of degrees of freedom. It is important to keep in mind that mobility analysis is a generalization and cannot account necessarily for a specific geometric configuration [17]. Actual manufacturing of the part will greatly influence the

accuracy of the modeling. In addition, deformations will exist in all members of an actual assembly, whereas mobility analysis assumes that links are infinitely rigid.

For a three-dimensional flexure system, there are six possible degrees of freedom relating to three translations and three rotations. The mobility of a flexure system with n links, j joints, and f degrees of freedom in the i^{th} joint is given as Equation (1-10) [46].

$$M_6 = 6(n - j - 1) + \sum_{i=1}^j f_i \quad (1-10)$$

For a planar mechanism which is assumed to have joints with only three degrees of freedom, the mobility can be written as Equation (1-11) [46]. It should be noted that reducing mobility analysis for planar analysis comes with the assumption that the system is ideal and constant throughout the depth of the part.

$$M = 3(n - j - 1) + \sum_{i=1}^j f_i \quad (1-11)$$

A final simplification which may often result applies when a planar mechanism is limited to only one degree of freedom joints. This can be accomplished through simple mechanisms, such as a notch hinge or composed of a subset of links and joints which only allow one degree of freedom. The mobility equation for this case is referred to as Grubler's equation and is given as Equation (1-12) [46].

$$M = 3(n - 1) - 2j \quad (1-12)$$

An example of the mobility calculation for a planar mechanism can be done for a flexural bearing system, the double compound rectilinear spring. This spring is comprised of notch-type joints which allow only one degree of freedom as a rotation.

The joints are attached to one another through links which have a significantly higher stiffness than the flexural joints. A schematic of this type of flexure system is shown in Figure 1-12. The joints are represented as circles.

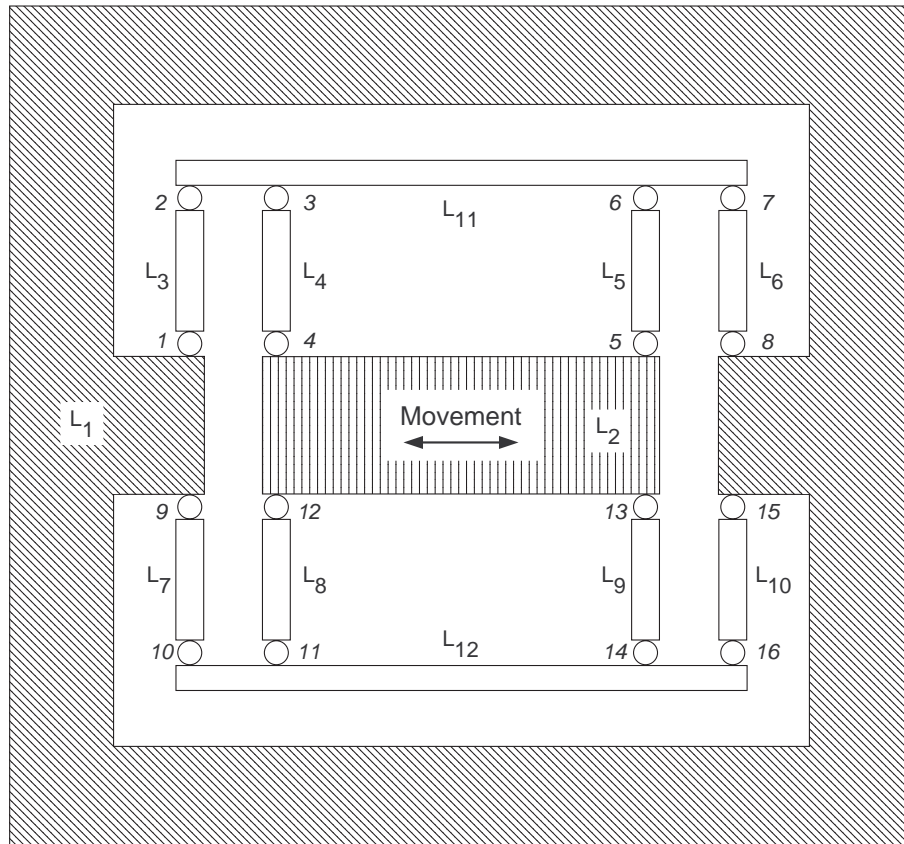


Figure 1-12. Double compound rectilinear planar flexure schematic for mobility analysis

For this analysis, the flexure system is assumed to be planar and the joints have only one degree of freedom. Therefore, Equation (1-12) can be used to determine the mobility. The planar mobility analysis given in Equation (1-13) for 12 links and 16 joints shows that the flexure system is free to move in only one direction.

$$M = 3(12 - 16 - 1) + 16 = 1 \quad (1-13)$$

This means that the movement of the flexure system is constrained to only allow linear motion of L_2 if body L_1 is fixed.

1.6 Thesis Overview

This thesis describes the design and testing of segmented mirror alignment using piezoelectric actuators. From previous alignment work, it has been shown that increased precision and design are necessary to meet the segmented mirror alignment requirements for the Constellation-X mission.

1.6.1 Thesis Hypothesis

Piezoelectric actuators are capable of aligning thin foil segmented mirrors by manipulating the shape of the mirror and correcting for errors introduced during installation. Physical placement, collimated beam testing, Centroid Detector Assembly feedback, and interferometry feedback will be used to test the hypothesis and ensure the correct alignment is achieved. The use of piezoelectric actuators will facilitate the future alignment of many closely nested mirrors and eventually allow for an efficient closed loop alignment technique.

1.6.2 Research Objectives

Over the past few years, several methods have been investigated in the development and design of ways to achieve the Constellation-X mission optical alignment requirements. With each of these methods comes the need for continued demonstration and improvements. The scope and purpose of this research is to:

- Detail the considerations and design of an alignment system for thin foil segmented optics utilizing piezoelectric actuators.

- Analyze the design of the positioning stages and the interface between the actuator and mirror.
- Present the thin foil segmented optic alignment methods utilizing piezoelectric bending actuators
- Test the alignment capability of piezoelectric bending actuators for a thin foil segmented optic

1.6.3 Research Contributions

The research objectives for this thesis are met which contribute to development of the Constellation-X spectroscopy x-ray telescope (SXT). The design considerations and analysis for using piezoelectric actuators for segmented optic alignment are detailed and applied in the design of two alignment assemblies which integrate into existing housings used in the technology development of the SXT. The alignment methods and results for each method are presented for the testing of the first generation alignment assembly.

The contributions of this thesis research to the SXT development include:

- Development of two alignment assemblies using piezoelectric actuators for aligning thin-foil segmented optics
- Analysis of flexure design, contact stresses, piezoelectric performance, and stiffness models relating to the alignment of thin-foil segmented optics
- Experimental demonstration of precise Centroid Detector Assembly alignment using piezoelectric actuators through testing of the first generation alignment assembly
- Demonstration of the capability of piezoelectric actuators for the minimization of installation induced errors in the axial sag of a single mirror segment near the actuation points with the use axial interferometry feedback

1.6.4 Methodology

The first method used to meet the requirements for this research will be the design of an assembly integrated into existing Constellation-X test structures using piezoelectric actuators. The second method used is the analysis of the mechanical design. The third method is the use of optical testing to determine if the mechanical design and use of piezoelectric actuators can manipulate a mirror segment to achieve the correct alignment including the use of optical interferometer to investigate the effects on the axial profile of the mirror using this alignment technique.

1.6.5 Remaining Chapter Summary

Chapter 2 gives overviews of previous alignment work and research done with regards to the Constellation-X program. The chapter also describes the conceptual design and key points of a piezoelectric alignment assembly. Much of the initial alignment work investigating the mirror behavior utilized manual adjustments. An additional method being researched utilizes a number of precision microcombs. The conceptual design includes information on requirements, materials, mirror interfaces and other considerations. Finally, the designs of two generations of piezoelectric alignment assemblies completed for this thesis are included.

Chapter 3 details the analysis of the mechanical design for important design functions. The analysis of contact stresses and tip design is detailed. In addition, the design of a coarse positioning flexure stage for positioning the piezoelectric actuators is discussed. A discussion on the motion of an actuator subject to exterior loads is included. The equivalent stiffness of the positioning system for use in the translation of motion and physical placement is also discussed.

Chapter 4 details the technique and results for testing mirror alignment. The chapter includes important points on the assembly of the structure and initial mirror placement with the use of a coordinate measuring machine (CMM). In addition, the chapter covers the optical testing accomplished using piezoelectric actuators. The first method of optical testing utilizes a collimated white light beam to facilitate a rough visual alignment over the entire mirror segment surface. The next method for optical testing utilizes grazing incidence testing with a Centroid Detector Assembly (CDA). The third method of optical testing uses normal incidence optical interferometry to investigate the effects on the axial figure of the mirror segment after installation and during alignment.

Chapter 5 provides the conclusions reached from the design and testing of the piezoelectric alignment assemblies. A summary of future work is included to assist in the evolution towards the alignment goals for the Constellation-X mission.

CHAPTER 2

ALIGNMENT ASSEMBLY CONCEPTUAL DESIGN

Previous assembly research provided insight into the requirements and methods that may be applied to precisely position and align thin foil x-ray optics. Using piezoelectric actuators is founded on the necessity for aligning closely spaced mirrors to high precision with the intent of using a closed loop alignment scheme in future applications. The current conceptual design should first demonstrate the effectiveness and feasibility of using piezoelectric actuators for this alignment.

2.1 Previous Assembly Research

Assembly research for thin foil x-ray optics and those specifically related to Constellation-X has led the way for improving on alignment methods. The use of radial supports, or struts, along the edges of the mirrors for positioning is a common feature among much of the work that has been done. In the build-up of a thin foil x-ray telescope assembly, the optics are typically aligned and then secured or bonded into place. The location at which the optic is held is known as an attachment point. The requirements for attachment points in a thin foil optic assembly stem from requiring the mirror segments to have fundamental frequencies above 50 Hz for parts of an optical system and have sufficient support and constraint to prevent buckling during launch [18, 19].

The Astro-E2 telescope utilized 13 radial support bars in each quadrant with grooves on the top and bottom of a mirror segment to position and align closely nested aluminum thin foil mirrors with epoxy-replicated gold coatings [20]. Figure 2-1 shows an assembly an Astro-E2 telescope made up of four quadrants of mirrors with each quadrant containing 175 mirrors. The diameter of this telescope is 40 cm.

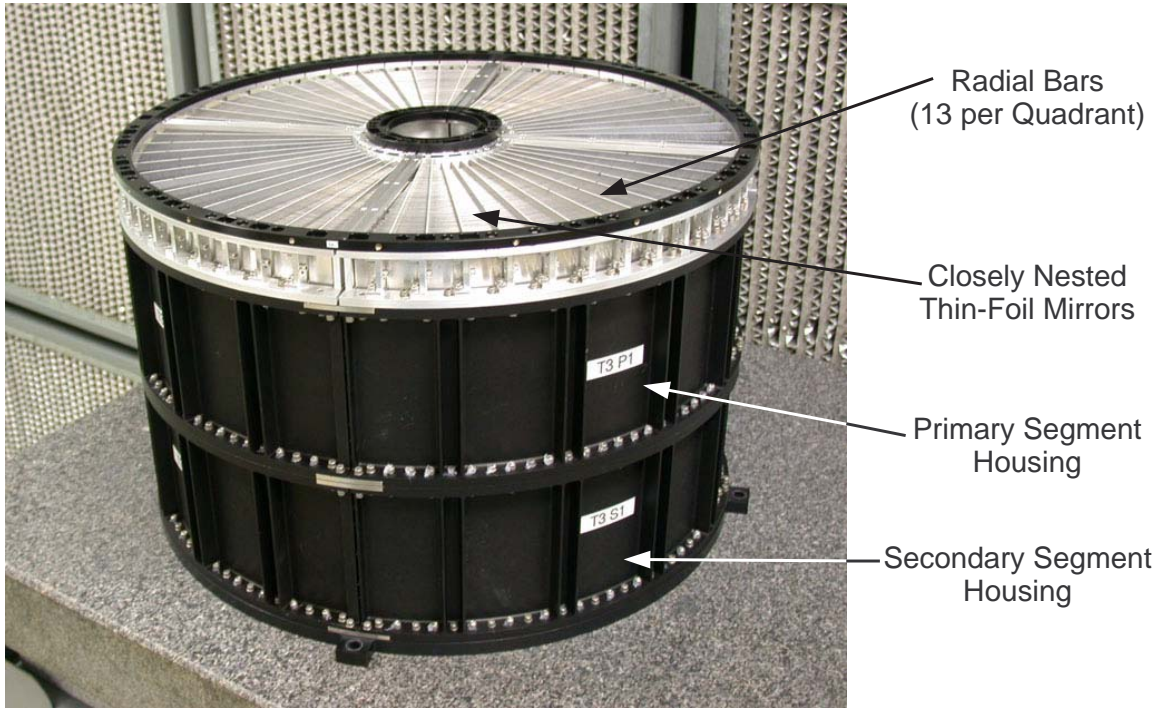


Figure 2-1. Astro-E2 telescope segmented mirror assembly [21]

The use of radial bars allows for a well-supported structure and simplified assembly process. However, the use of radial bars alone in the Astro-E2 is capable of achieving approximately arc minute level resolution and is limited by machining tolerances, which is not sufficient for the Constellation- X mission. In addition, the radial bars align all of the mirror shells in a quadrant at the same time and are not intended to manipulate each mirror segment figure individually. Ideally, the radial bars are used simply as a holding structure for the mirror segments.

A previous method that has researched similar to the use of radial bars involves the use of high-accuracy silicon microcombs to align the mirror using interface points on the top and bottom edges of the mirror [22,23,24]. This method utilizes a precision assembly reference structure to align the flat mirror substrates using a spring and

reference silicon microcomb within a flight module. Figure 2-2 shows the microcombs holding a flat mirror substrate.

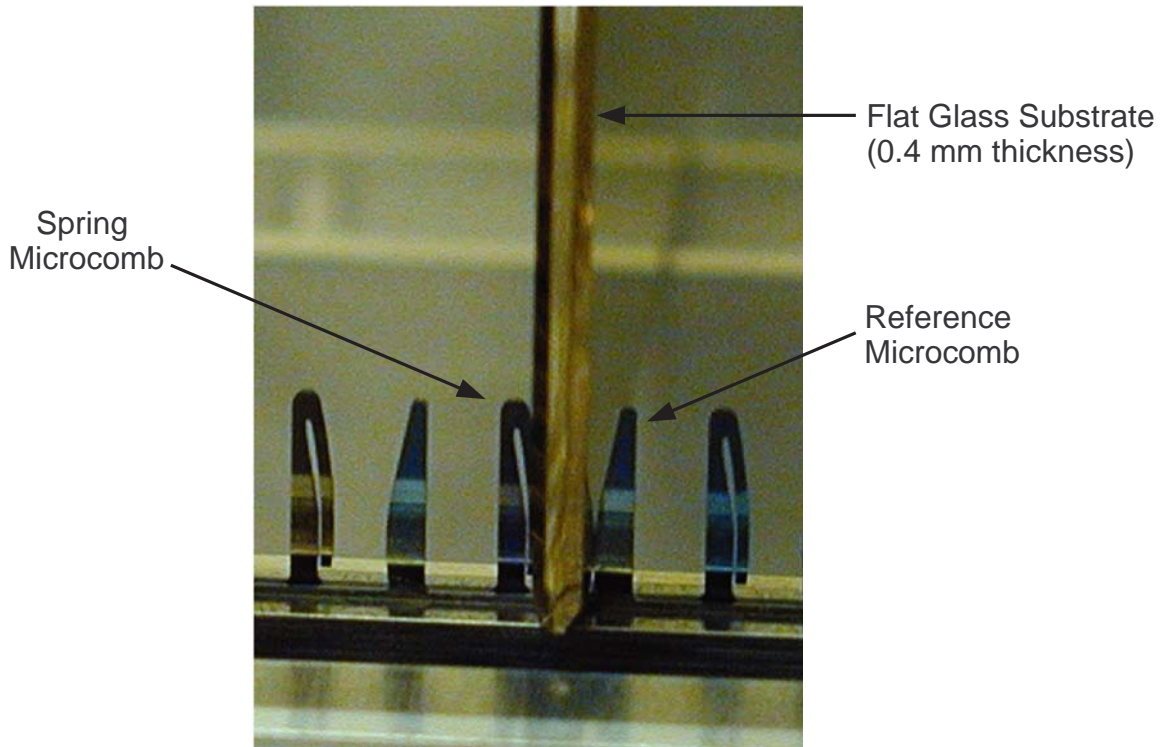


Figure 2-2. Flat glass substrate between microcombs [1]

Microcombs offer significant advantages over traditional radial bars for mirror segment alignment. The etched silicon microcombs may be designed for tight tolerances, allowing for precise positioning of mirror segments. The etched silicon also has an improved surface finish when compared with machined radial bars, which results in a better interface between the alignment mechanism and mirror. The use of silicon microcombs positions all of the mirror segments, and is not used for individual mirror manipulation in the current configuration.

Additional research considered the radial manipulation of individual optics. This work has been part of the phase buildup for the technology demonstration of building the SXT flight modules at the NASA Goddard Space Flight Center (NASA-GSFC). The first

alignment research in this buildup was the Optical Alignment Pathfinder 1 (OAP-1) [25]. This work utilized a mirror actuator interface of ruby balls which were driven by manual micrometers and was used as an initial study on the mirror alignment. As it was an initial study, the unit allowed the manipulation of one optic per housing and was constructed of aluminum, which has a high coefficient of thermal expansion (CTE) compared with the glass samples. The OAP-1 is shown in Figure 2-3.

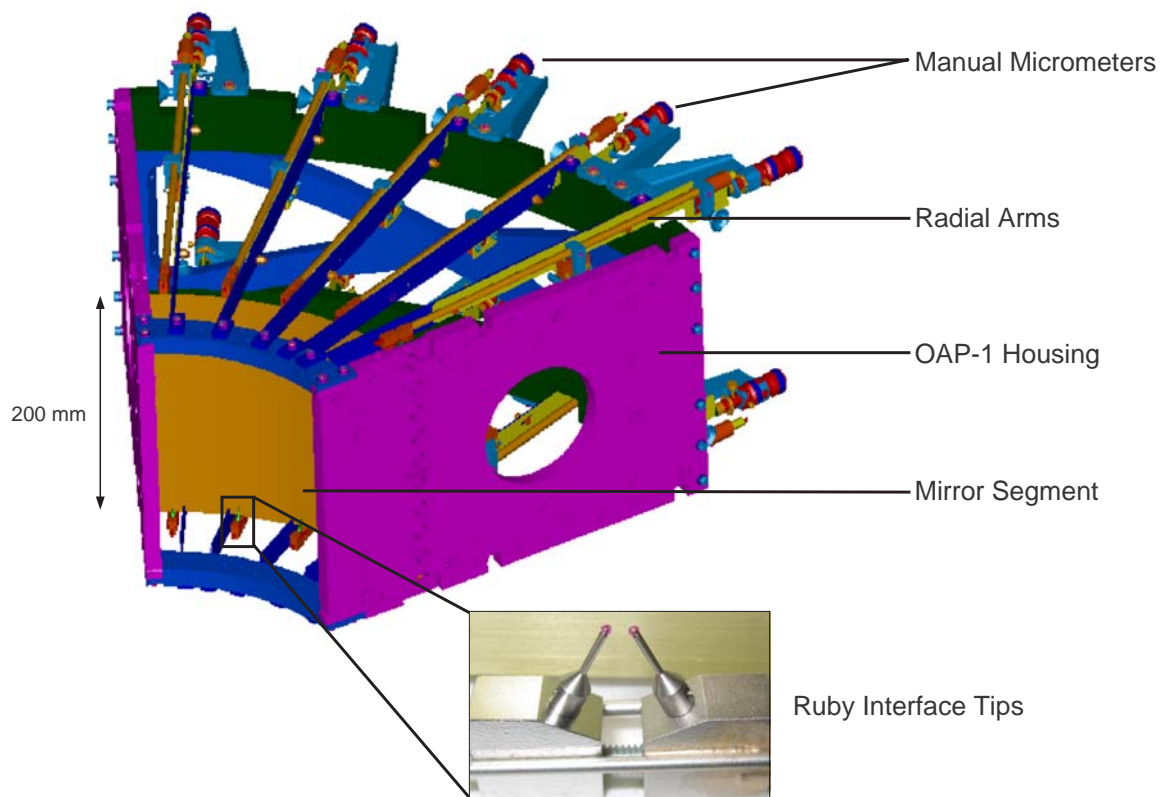


Figure 2-3. OAP-1 alignment assembly

The OAP-1 setup was followed by the Optical Alignment Pathfinder 2 (OAP-2), which was comprised of a smaller titanium structure with radial struts for bonding of the optic. The OAP-2 was capable of fitting within the OAP-1 alignment assembly. The OAP-2 mirror segment was aligned with the OAP-1 manual adjusters and then bonded into the radial struts on the OAP-2 housing. The testing of the OAP-2 structure yielded

additional information on the relation of radial actuator movements in relation to the figure and alignment of the mirror [26]. The OAP-2 housing is shown in Figure 2-4.

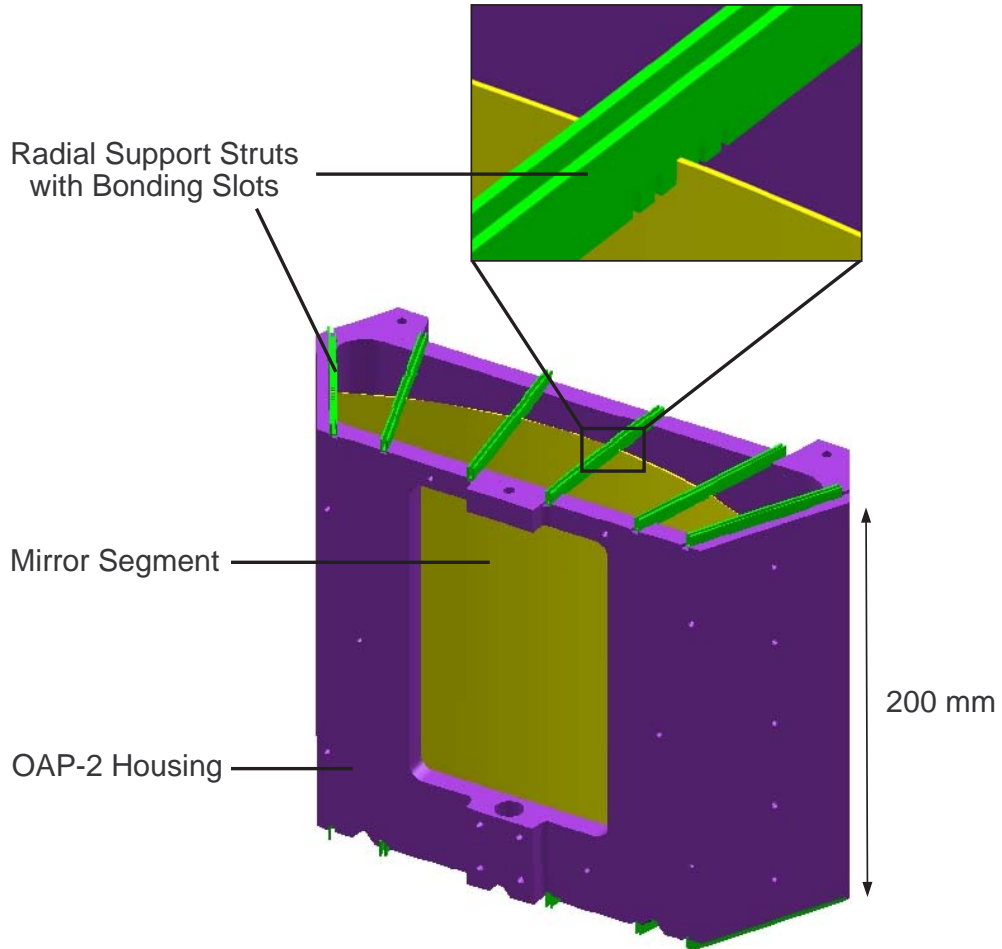


Figure 2-4. OAP-2 housing with radial struts

The development of OAP-1 and OAP-2 led to important information on the mirror response to actuator movements. The large manual micrometers did not allow for placement of multiple mirrors and could not achieve the required alignment precision. A factor which may have prevented the precise alignment necessary is likely the actuator-mirror interface. Small misalignments of the actuation points which grasped the front and rear of the mirror cause a local bending of the mirror.

The development of a piezoelectric actuator assembly, which is an important aspect of this thesis, is important in the demonstration of SXT buildup in that it provides a means to align closely spaced mirrors with increased precision. In addition, the improved design of the actuator-mirror interface is also emphasized, as it has a large impact on the achievable alignment.

2.2 Functional Requirements

There are many considerations which drive the design of a piezoelectric actuator alignment assembly for segmented optics. In general, the alignment assembly must be able to first position the actuators and mirror to approximately the correct position. This coarse positioning stage is utilized during the physical assembly and alignment process and must be capable of positioning the actuators to the prescribed mirror position within the range of the actuators. The fine positioning system, or piezoelectric actuators, must be able to adjust the cone angle and radial position of the mirror to the prescribed value. In addition, the actuator assembly must be able to correct the errors of the axial figure of the optical segments at the actuation points introduced during mirror installation, as this has a large impact on the achievable image quality. For the scope of this research, the following functional requirements were specified for the alignment assembly:

- Mirror segments should be capable of being aligned using the Centroid Detector Assembly to less than 1.25 arcseconds RMS radius.
- Positioning system must be capable of correcting the axial figure errors introduced during installation of the mirror segment at the actuation points.
- Interface points between the actuators and mirror must not overstress the mirror and cause mirror failure. A conservative estimate limits the contact pressure to approximately 160 MPa.

2.3 Actuation Points

The selection of the number of actuation points is based on the necessity to have control over the entire mirror and allow enough points for bonding the mirror to a final support structure after alignment has been achieved. For a mirror segment, it is advantageous to have positioning capability at the center azimuth of the mirror. This can be used initially to make a rigid body adjustment of the tip of the mirror. The placement of the remaining actuation points are set for equal spacing throughout the mirror segment, resulting in an odd number of actuation points for the top and bottom of the mirror segment. Actuation at the corners of the mirror alone may be insufficient in affecting the rest of the mirror segment, as the corners have less rigidity for the approximate conical shape [60]. In some cases, it may even be beneficial to move the end adjustment points away from the corners, as edge effects of the mirror and the lack of rigidity may prevent the desired alignment performance from being achieved [27]. The selection of five actuation points allows for the ends of the mirror to be manipulated as well as intermediate sections along the mirror which would otherwise not be correctable. It is known that the number of actuation points results in an over constraint of the optic which may induce initial deformations, but which also allow for the corrections of these errors. By increasing the number of actuation and subsequent bond points, the effective deformation due to gravity sag for the optical segments, which remain at a slight angle, is reduced [24]. Though the number of bonding points utilized in the design corresponds to the actuation points for the current design utilizing a monolithic structure, analysis has shown that the use of six end supports instead of five for the bonding and support of the mirror reduces the optical performance sensitivity to bulk temperature changes in the assembly structure [28].

The current housing assemblies and modular buildup of the SXT utilizes approximately 50 degree mirror segments, depending on the cutting accuracy in creating the part. By designating the center of the mirror the zero azimuth, Figure 2-5 gives the location of the actuation points. The azimuth location corresponding to actuators B1 and U1 may also be referred to as P1. The designation of points P2, P3, P4, and P5 follows the same format.

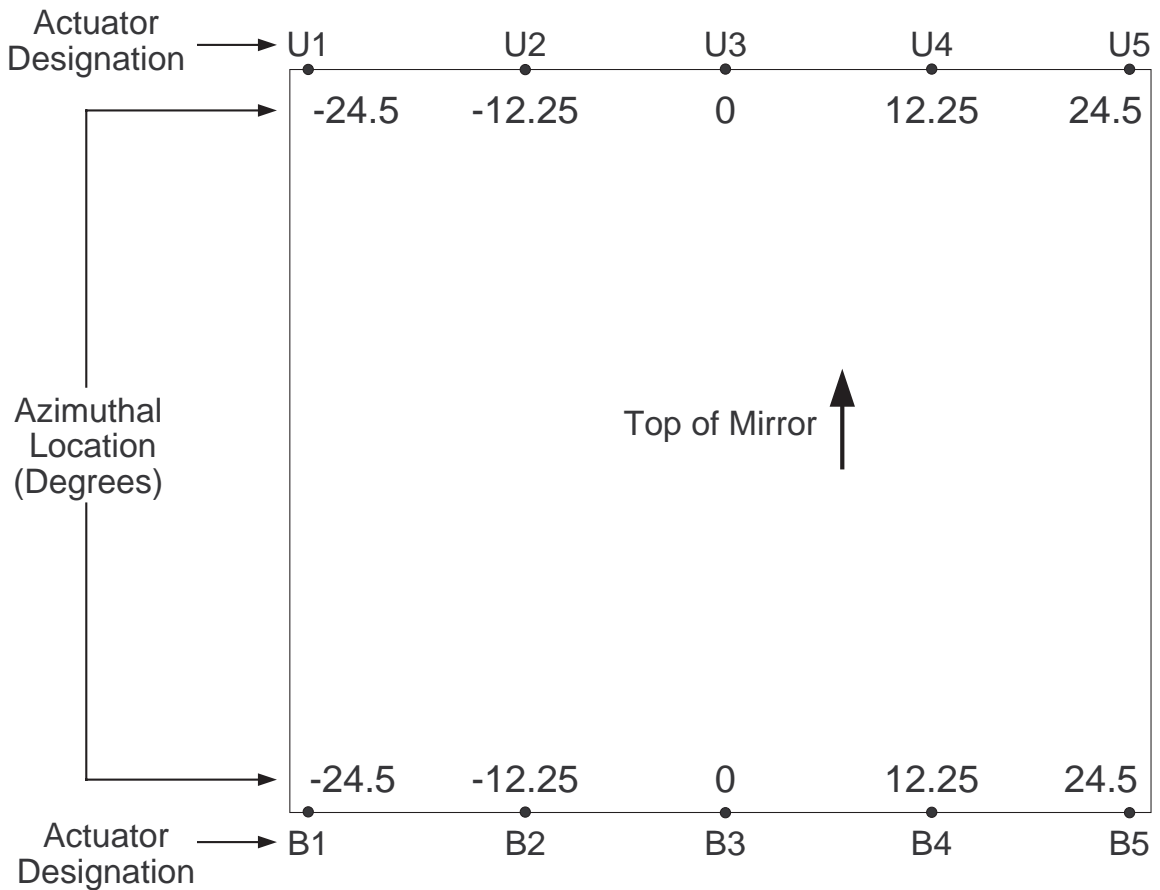


Figure 2-5. Mirror actuation point locations

The end actuation points are placed slightly inboard of the mirror edges to allow spacing for the tip that acts as the mirror-actuator interface and avoid edge effects of the mirror. In addition, this spacing can also be applied for use in bonding the corner of the mirror after alignment. In order to secure the alignment achieved using actuators, the

bonding points may exist near the actuation points. Figure 2-6 shows a slot configuration which allows the mirror to be aligned using piezoelectric actuators and then bonded into place. The clearance of the gap configuration between the front and rear of the mirror should allow for the desired travel of the actuators and still remain within the acceptable bond line range for the adhesive in use. For current design, this clearance distance is 100 μm , which is still fairly large. It would be advantageous to decrease this clearance, as the minimization of bond line thicknesses is desired to minimize thermal effects of the bonding adhesive and minimize shrinkage effects during the bonding process. The determination of appropriate bonding techniques and setups is an important issue that still remains for the assembly of the SXT instrument.

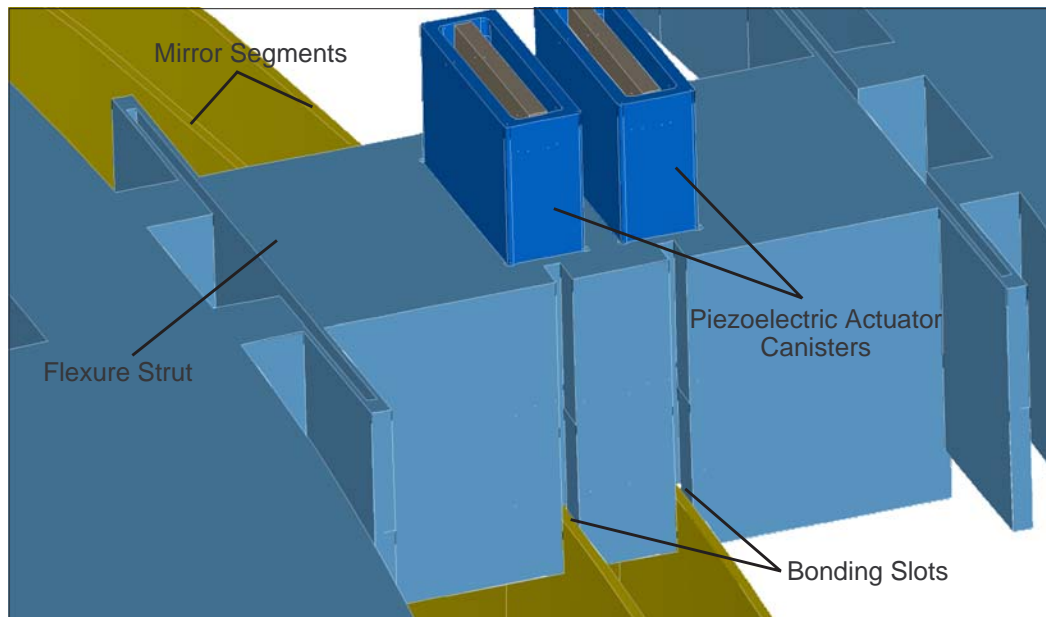


Figure 2-6. Flexure strut with integrated bonding slots

2.4 Actuation Stages

As discussed in section 1.4 and applicable to all of the assembly methods, the placement and alignment of the optics are referenced off of the optical axis. For the application of radial adjustments, the required travel is dependent on the accuracy of the

assembly method. For the build-up of current alignment assemblies, a coarse actuation stage is included at each of the actuation positions along the mirror. This is used as a radial positioning stage and will be referred to as the *strut*. This actuation stage is coupled with a fine positioning stage, which is the piezoelectric actuator. In the development of the piezoelectric actuator assembly, two variants of strut designs have been utilized which will be discussed.

2.4.1 Independent Strut Design

For many applications, the strut may be an independent structure which is positioned and secured in place. This is similar to the methodology used for the Astro-E telescope, as shown in section 2.1. This is a simple approach which allows for the movement of struts along mechanical slots. Figure 2-7 shows a model of an independent strut approach which houses a piezoelectric actuator within a canister.

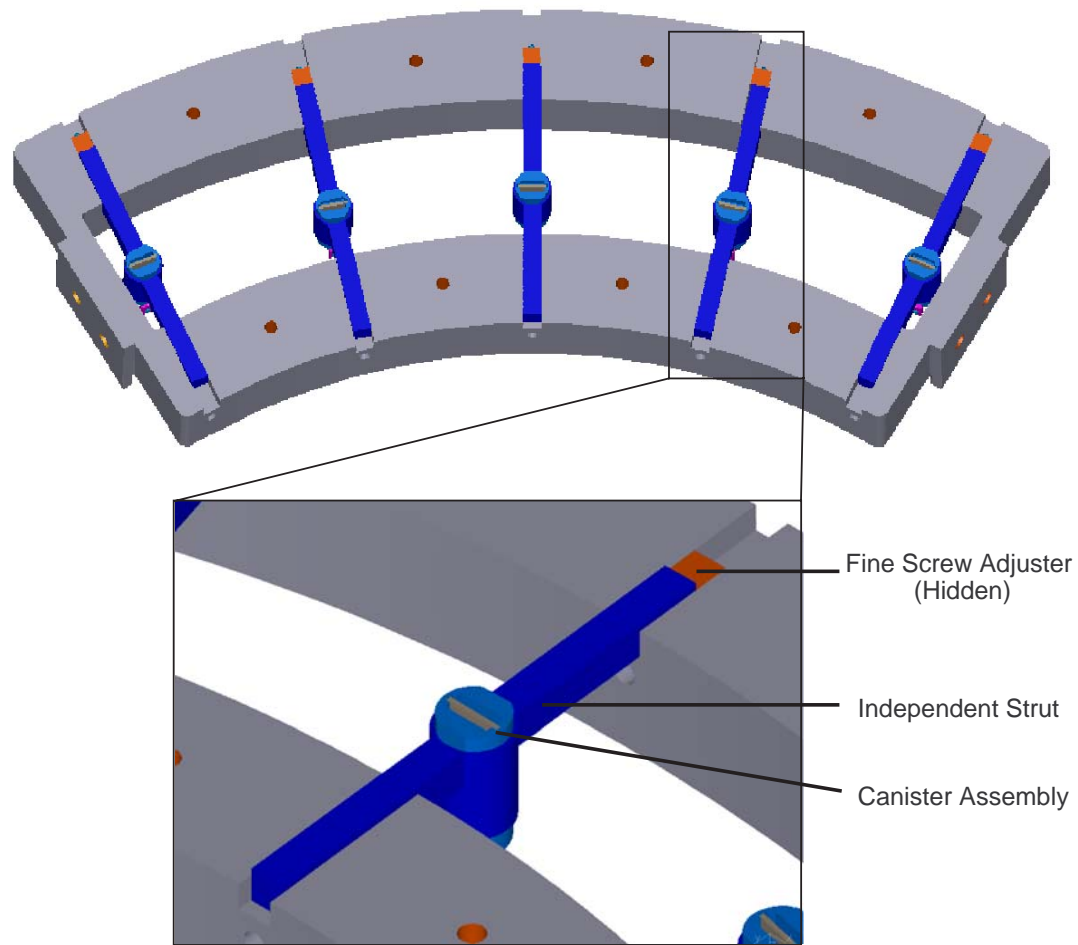


Figure 2-7. Independent strut design within a strut frame

For the movement of the strut, the resolution requirements of the actuation stage will influence the drive mechanism that is needed. However, space requirements become the driving factor in the selection of drive mechanisms which must fit within an assembly if multiple units are required. For simplicity of design and compactness, the use of small extremely fine-pitched adjusters is adequate to place the mirror to the correct position within the range of the fine positioning stage, the piezoelectric actuator.

The advantage of the independent strut frame is that a large travel range may be specified, if needed, and will likely be limited by the drive mechanism. The independent strut may be bonded into place once the desired position has been achieved. As with any

other permanent bonding step, this does effectively limit the coarse actuation stage to a one-time use which may be acceptable as long as subsequent motions may be achieved with the fine actuation. In an independent strut design, the rigidity of the assembly is affected by the stiffness of the bonds. A disadvantage of the independent strut is that the tolerance and fit of the piece parts and additional assembly necessary due to the number of components present increased challenges in meeting the precise alignment requirements.

2.4.2 Monolithic Strut Design

The second variant approach to a coarse alignment stage is the use of a monolithic strut frame. The monolithic strut frame uses flexural bearings to provide motion in the radial direction. Figure 2-8 shows the design of the monolithic strut frame.

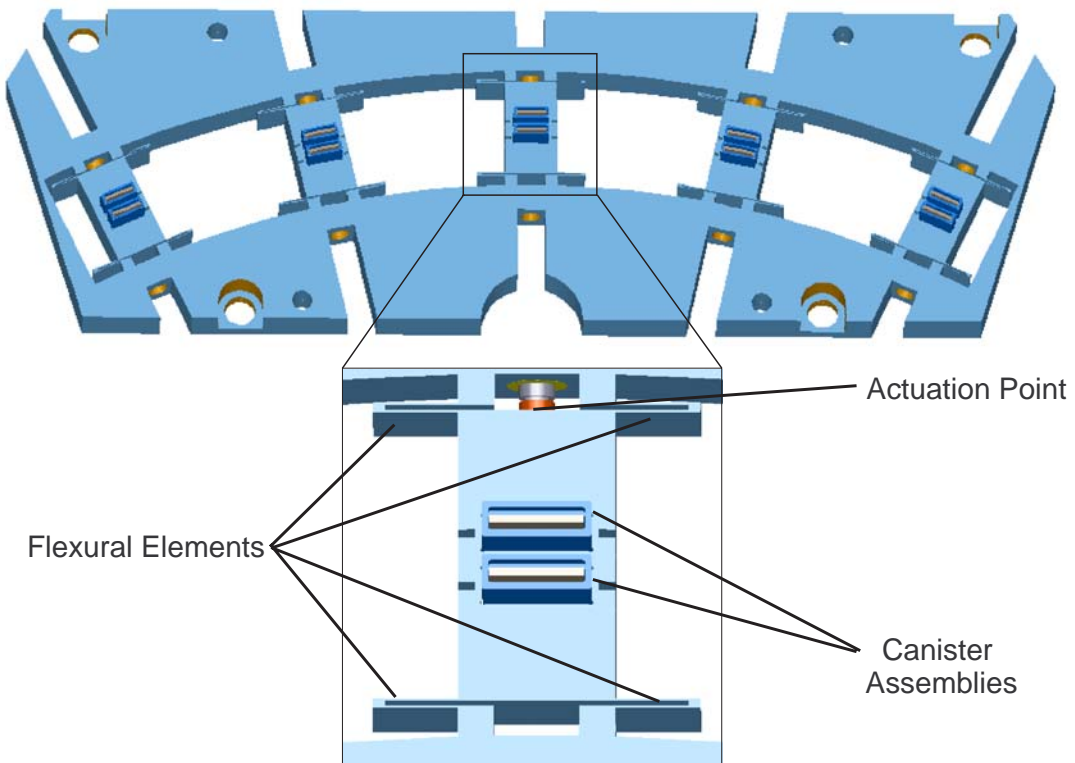


Figure 2-8. Monolithic strut frame utilizing flexural elements

As discussed in section 1.5, flexures offer smooth, repeatable motions and eliminate the need for close fitting parts, which is an issue with the independent strut design. The use of a monolithic structure simplifies the assembly process. The major disadvantage to the use of flexures for strut design is a decreased out-of-plane stiffness. Maximizing the out-of-plane stiffness is an important issue which is included in the flexure design analysis of section 3.3. In comparison with independent struts, the range of travel is also decreased.

As with the independent strut design, the use of an extremely fine-pitched adjuster can be utilized. The importance of the drive coupling design between the translation stage and adjuster is apparent in that the rotation of the adjuster may impart an unwanted torque due to the friction between the two bodies. In addition, the adjuster of a drive coupling may show some variation about the path of motion as well as a misalignment of the axes of the adjuster and stage which will further prevent linear motion of the driven stage [43]. An example of a drive coupling to alleviate these coupling errors is the wobble pin drive. However, there are also other alternatives which may compromise a bit from the ideal coupling but are still effective. The use of a spherical end on the adjuster minimizes the errors seen from axes misalignment by creating a point contact. The use of a synthetic sapphire interface between the translation stage and adjuster minimizes the friction and resulting torque that will cause rotations about the drive direction. The use of a synthetic sapphire also increases the stiffness of the coupling. A cup jewel is utilized to increase the point contact area and minimize the contact stress between the two bodies, which will be discussed in the design analysis. Figure 2-9 shows the interface of a fine pitch adjuster with the flexure translation stage.

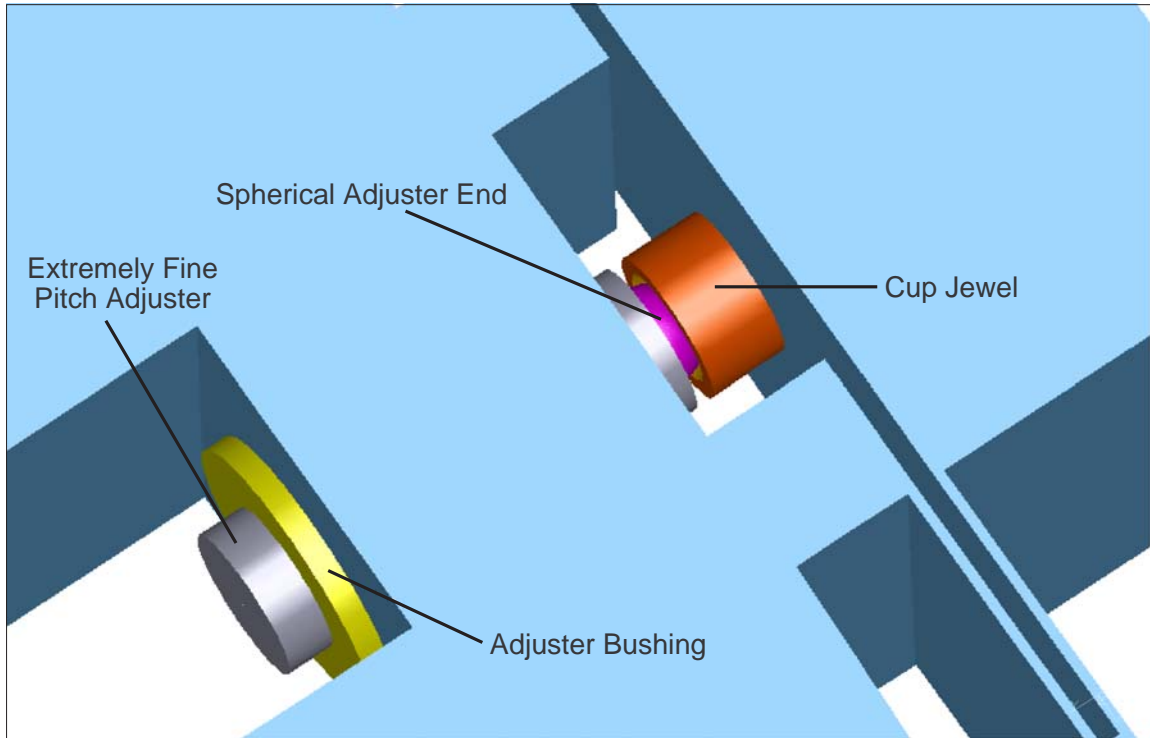


Figure 2-9. Fine-pitch adjuster interface for strut movement

2.4.3 Piezoelectric Actuator Canister Assembly

Piezoelectric actuators act as the fine adjustment mechanism for the alignment of x-ray optics. The intent of housing the actuator within a canister assembly is to allow the actuator to be removed after the optic has been aligned and bonded into the housing structure. An additional advantage that this serves is that it increases the effective collecting area of the mirror segment by allowing the collection of x-rays through the area previously blocked by the piezoelectric actuators. This is an important point for any assembly structure which houses closely nested thin foil optics. An additional benefit that the canister design permits is adjustability of the height of the actuators to accommodate varying sizes in the mirror heights due to manufacturing errors. Figure 2-10 shows two variations of piezoelectric actuator canister assemblies.

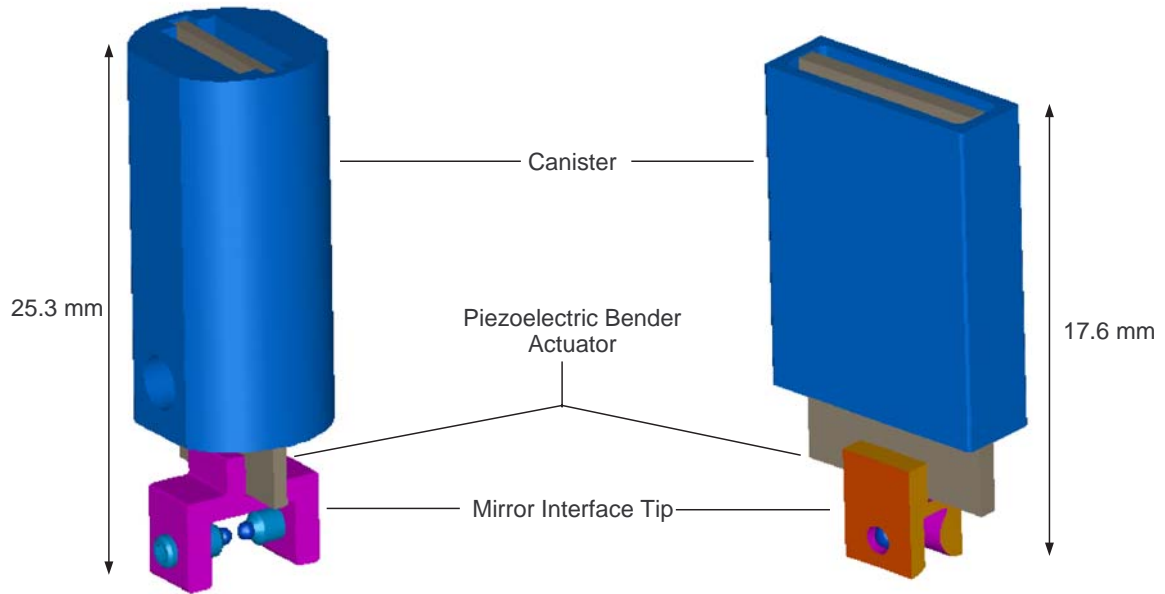


Figure 2-10. Piezoelectric bender actuator canister assemblies

The piezoelectric actuator is integrated into the canister through the use of bonding at the inactive region of the end of the actuator. For current applications the canisters may be held within the strut design with the use of a cyanoacrylate adhesive, which is used primarily because the bonds can be removed with a de-bonding solvent for the removal of the canisters after alignment.

The most important part of the piezoelectric canister assembly is the actuator-mirror interface, which will be referred to as the tip. The purpose of the tip is to impart the motion of the actuator to the mirror segment in only the intended radial direction without imparting unwanted moments on the mirror surface, which will have adverse effects on the mirror alignment. The importance of drive couplings applies to the design of the actuator tips. The condition of point contact is desired to minimize unwanted moments within the mirror.

Since the segmented mirrors for Constellation-X have a concave and convex side, there are several ways which result in point contact. The first way of achieving point contact is through the use of spheres on each side of the mirror. This is shown in Figure 2-11.

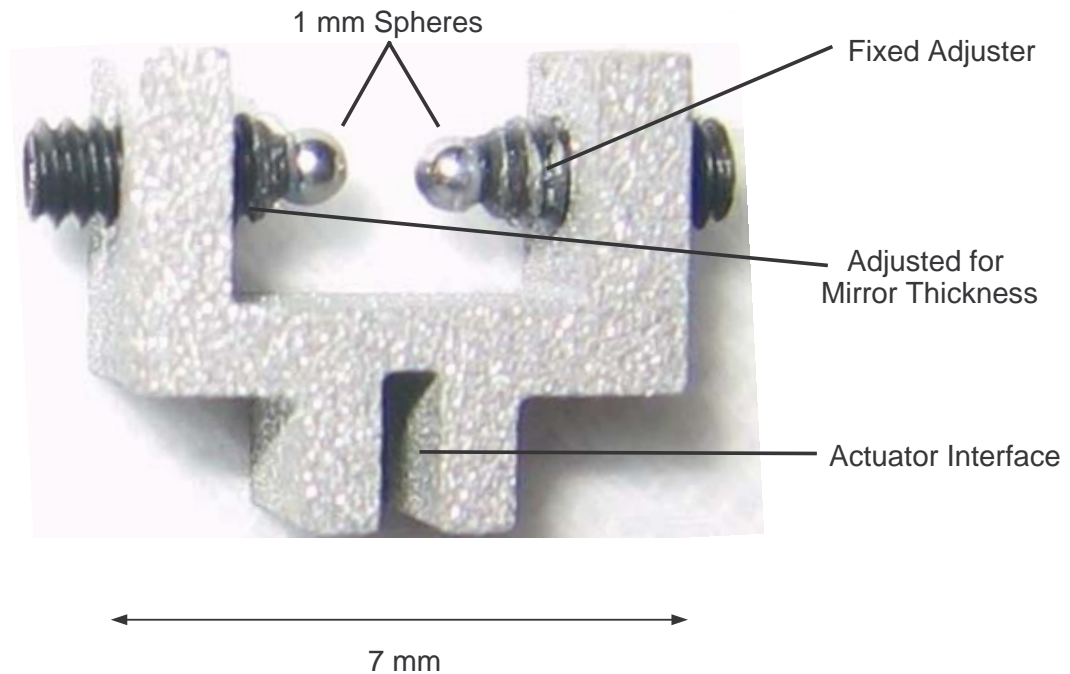


Figure 2-11. Test tips utilizing opposing spheres for mirror manipulation

The use of opposing spheres is excellent for creating point contact. It is also of note that the mirror must not be pinched by the opposing spheres, as manufacturing tolerances will result in the points of contact not being aligned. These off-center contact points create an undesired moment in the mirror. The creation of tips small enough to fit within the mirror segments with two spherical surfaces is increasingly challenging as there may be clearances to less than 1.5 mm between mirrors. In looking at the ability to manufacture and assemble a telescope with many interface points, it is important to remember manufacturability in the design of the actuator tip. One such way to maintain

point contact which is easily adaptable to wire electro-discharge-machining (EDM) techniques is to utilize cylinders at right angle case for the convex side and a sphere for contacting the concave side of the mirror. Figure 2-12 shows this configuration of tip. While this is still a prototype tip, the decreased size is a positive step in achieving the size necessary for the design mirror spacing.

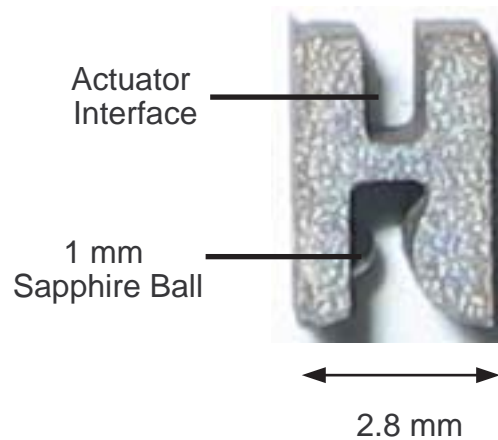


Figure 2-12. Second generation test tips utilizing an opposing sphere and cylinder

In order to have a sphere contacting the concave side of the mirror, the tips must be assembled by inserting a synthetic sapphire ball into a guide hole which is opposite of the cylinder and backfilling with an ultraviolet (UV) cure adhesive. The desired tip spacing can be set by assembling the tip with an appropriate glass sample or precision ground spacer with the necessary thickness. This tip spacing includes a small amount of clearance compared with the mirror thickness to avoid pinching the mirror and allow for removal. There are several other design considerations for the development of actuator tips. The first is that a low coefficient of friction is desired to minimize forces tangential to the actuation. In selecting the dimensions for the curvatures of the tip, the contact stress is an important parameter which is discussed in section 3.2.2.

2.5 Other Design Considerations

There are several other design considerations in the development of a piezoelectric actuator alignment assembly. The first of these considerations has been previously mentioned and emphasizes the importance of minimizing obstructions to the collecting surface of the mirror. This is important in the selection of the strut sizing as well as the type of flexure strut that may be selected. The second consideration is the importance of the interface which the mirror rests on within the housing. Another impact of the mirror supports is that it has been shown that the friction between the surface and the mirror resists the movement of the actuator and creates a bending moment within the mirror [24]. One way to counteract this is to add a low coefficient of friction coating at the mirror support point of the titanium structure, such as Tiolon® [29]. Another option that was utilized in the first assembly design is the use of a Teflon interface for lowered friction. Finally, the mirror may rest on the actuator to avoid additional mirror deformation.

The selection of materials has important implications from several points of view, including thermal, structural, and from a mirror interface standpoint. From a thermal expansion standpoint, the basis for determining requirements is from the glass substrates, as this is the critical component. As mentioned, the glass used for the substrates is Schott D-263 glass. The minimization of CTE mismatches between materials used for any assembly of the mirrors along with the utilization of symmetric design will aid in the thermal stability of the assembly. The design, testing, and operation for both the testing assemblies discussed in this thesis and the SXT telescope assembly will be done near room temperature at approximately 20° Celsius. This is important to keep in mind in

utilizing CTE data for material selection, as CTE values may be averaged over much larger ranges. The comparison of thermal properties of several materials of interest for the design is given in Table 2-1.

Table 2-1. Thermal properties of assembly materials

Material	Notes	CTE ($\mu\text{m}/\text{m}\cdot^\circ\text{C}$)
Aluminum – 6061	Linear, 20-100 °C [30]	23.4
Ti 6-AL-4-V	Linear, 10 °C to 30 °C [31]	7.30
Allvac [®] Ti-15Mo [32]	Linear, 10 °C to 30 °C [31]	6.44
Synthetic Sapphire [33]	Parallel to material c-axis	5.30
Schott D-263 [34]	Linear, 20 °C [35]	6.99

The use of aluminum alloys is useful for initial demonstrations due to its ease of manufacturing. However, the thermal mismatch between aluminum and the glass substrates creates a problem for distortion over a temperature range. The use of titanium offers a relatively lightweight and stiff structure. The Allvac Ti-15Mo is a beta titanium alloy which shows excellent thermal properties in the range of operation for the assemblies and also exhibits a high strength to density ratio, making it attractive from a structural standpoint. From a mirror interface standpoint, the selection of the material should ideally have a high surface finish, high compressive strength, and high modulus of elasticity [42]. As previously mentioned, the existence of a low-coefficient of friction is also important for the tip design.

In the alignment of multiple housings, as in for the primary and secondary mirror elements, the use of a kinematic coupling that utilizes the principle of exact constraint is recommended. Exact constraint refers to the condition when the number of constraints exactly equals the six degrees of freedom [36]. The advantages of exact constraint

include high repeatability, predictable performance, minimal elastic distortions of the bodies from over constraint, and the ability to obtain accuracy by adjusting at the contact points of the kinematic coupling [41]. Exact constraint may be obtained through the use of six contact points between two bodies, which can be achieved through several configurations. An example of this type of coupling can be achieved using three vee grooves which are interfaced with three spheres, as shown in Figure 2-13.

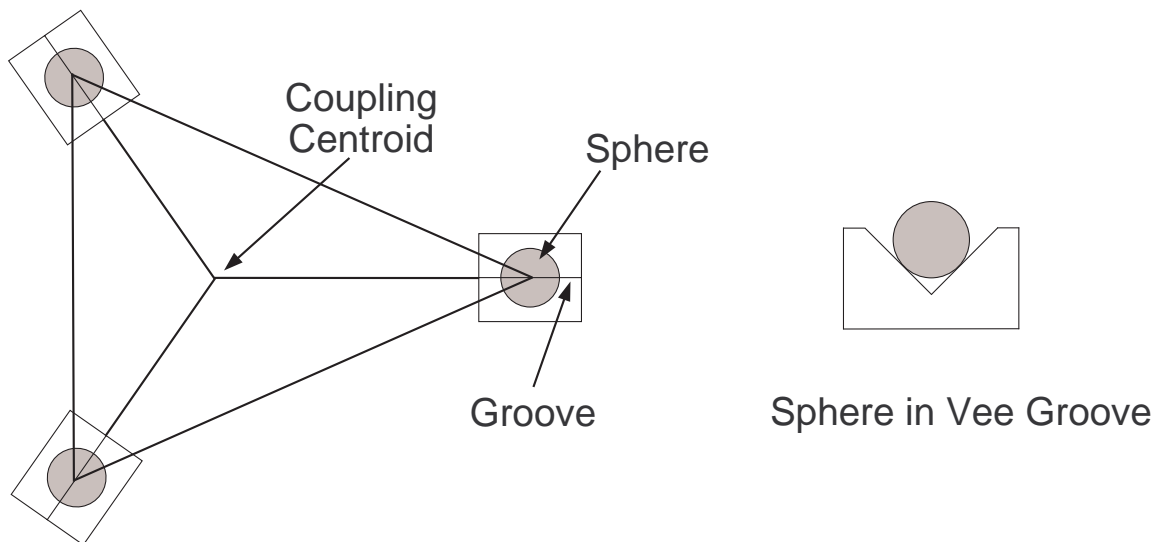


Figure 2-13. Kinematic mount featuring three spheres within vee grooves

In the design of a kinematic mount, the location of the coupling centroid is found at the intersection of the vectors normal to the planes of the contact force vectors. For balanced stiffness in all directions, the normal vectors to the planes containing the vector force pairs should bisect the angles between the spheres [42]. The coupling centroid is also the location of the thermal center for the mount. For the design of the kinematic attachment points on the structures housing mirror segments, the desired thermal center is the optical axis. By placing the coupling centroid at the optical axis, improved thermal stability is achieved by sacrificing part of the kinematic coupling's stiffness. Figure 2-14 shows this vee-groove orientation on the OAP-2 housings.

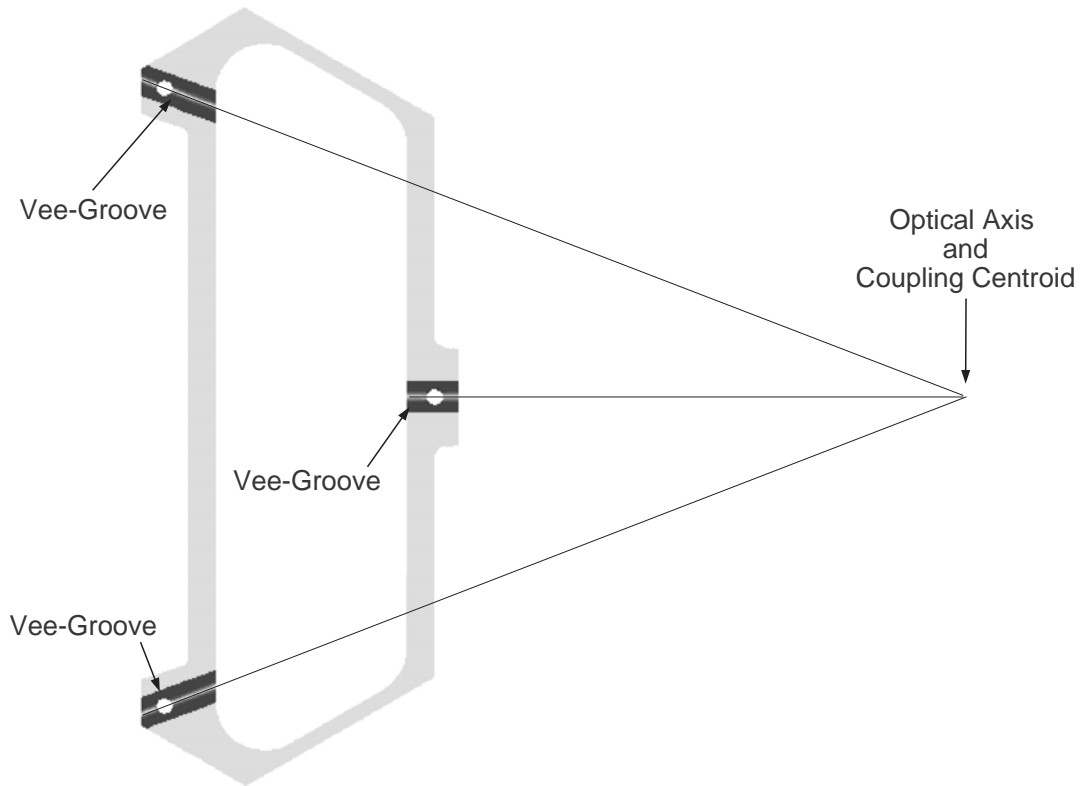


Figure 2-14. Vee-groove orientation with co-located optical axis and coupling centroid

2.6 First Generation Piezoelectric Actuator Assembly Design

The first generation piezoelectric actuator assembly, or Piezo Prototype (PPI), is the initial test setup for the manipulation of a single mirror segment. The design was required to integrate with the existing OAP-1 structures and testing hardware. In addition, aluminum was utilized for manufacturing considerations, as decreased thermal performance was accepted for the initial testing of using piezoelectric actuators. Figure 2-15 shows the PPI assembly. The design incorporates several of the simpler design considerations, such as independent struts and larger tips as previously discussed. The testing results achieved thus far are from the testing of PPI. The kinematic mount interface is shown, which allows for rigid body tip and tilt adjustments of the housing.

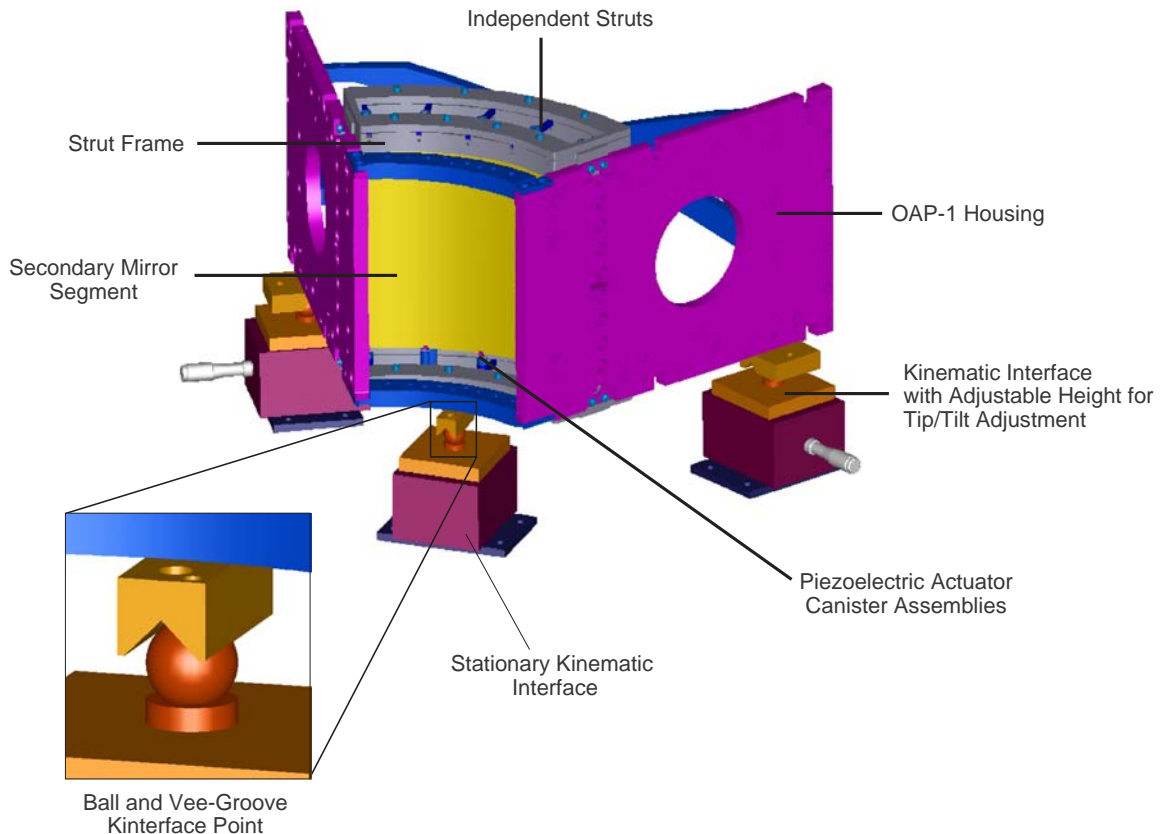


Figure 2-15. First generation piezoelectric actuator alignment assembly

2.7 Second Generation Piezoelectric Actuator Assembly Design

The second generation piezoelectric actuator assembly, or Piezo Prototype II (PPII), is the concept variation which advances the use of piezoelectric actuators utilizing smaller components and the ability to align a primary and secondary mirror segment pair. The use of smaller components, including canisters and tips, allows for two reflector sizes (485 and 494 series) to be nested while held by actuators. The PPII is required to integrate with current OAP-2 housings for the use of current testing hardware. The use of titanium components increases the thermal stability of the system as opposed to PPI. The additional concepts of monolithic flexure strut design and actuator tips with simplified design and decreased size are incorporated. The use of a kinematic interface is utilized in the connection between the two housings. Figure 2-16 shows the PPII.

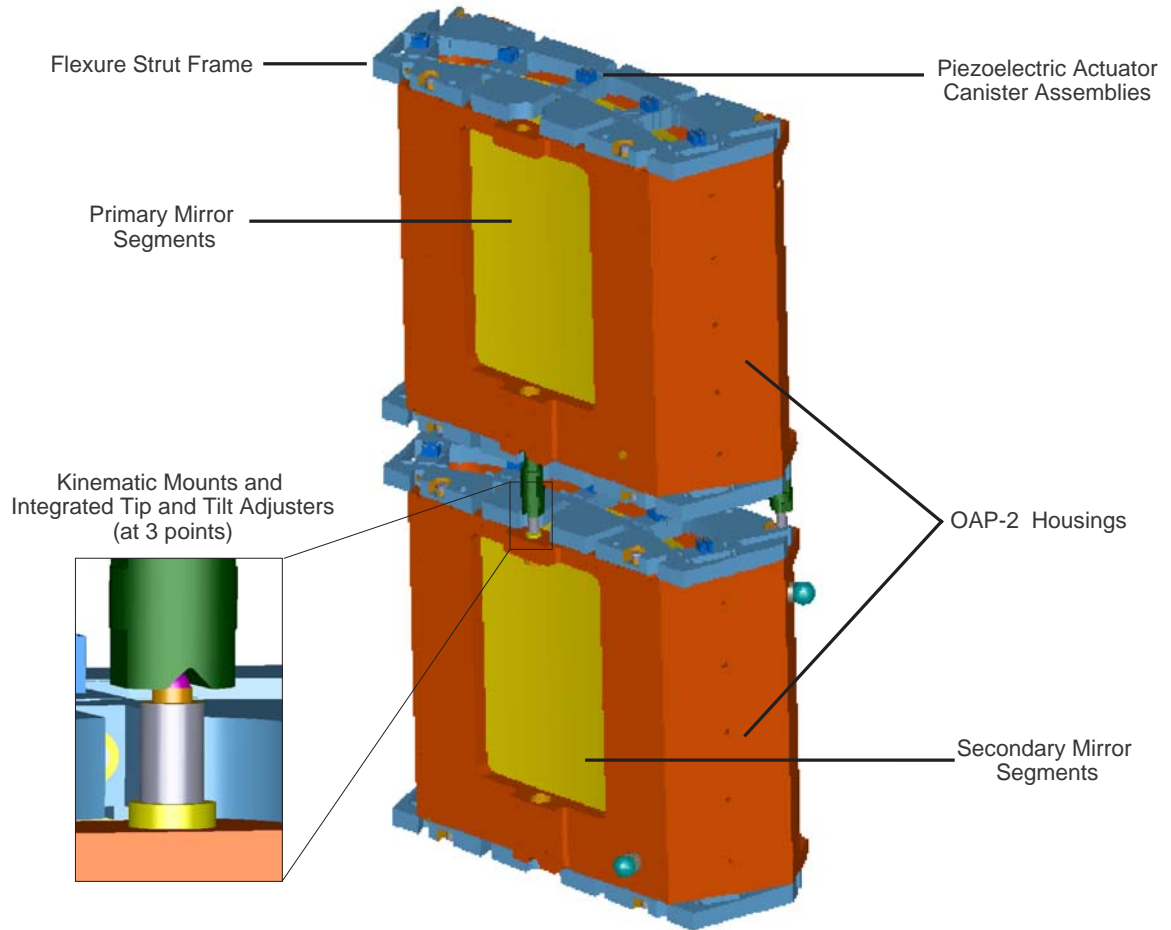


Figure 2-16. Second generation piezoelectric actuator alignment assembly

The kinematic interface incorporates differential screw adjusters to allow for rigid-body adjustments to the primary mirror with respect to the secondary mirror. In terms of the rigid body alignment errors given in section 1.4, the three adjustment points allow for corrections to the axial position error, tangential tilt error, and relative radial tilt error of the primary mirror. The resolution of the axial position adjustment is dependent on the resolution of the actuator. The resolution of the rotation is dependent on the resolution of the actuator and distance from the point of rotation. Equation (2-1) gives the angular resolution for an actuator, x_{step} , moving at a distance of d_r from the center of rotation.

$$\theta_{step} = \tan^{-1} \left(\frac{x_{step}}{d_r} \right) \quad (2-1)$$

The differential screw adjusters used in PPII travel 25 μm for every 360 degree turn. For determination of the angular resolution, it is assumed that a five degree turn is the smallest movement of the screw. Table 2-2 shows the angular and axial positioning resolution for PPII rigid body adjustments using differential screw adjusters.

Table 2-2. Rigid body adjustment resolution for PPII

Parameter	Value
Differential Screw Travel/Turn (μm)	25
Turn Resolution of Screw (degrees)	5
Differential Screw Resolution, x_{step} (μm)	0.347
Radial tilt adjustment arm, $d_{r(t)}$ (mm)	103.427
Radial tilt angular resolution, $\theta_{step(r)}$ (arcsec)	0.692
Tangential tilt adjustment arm, $d_{r(t)}$ (mm)	90.488
Tangential tilt angular resolution, $\theta_{step(t)}$ (arcsec)	0.791
Axial Position Resolution (μm)	0.347

CHAPTER 3

MECHANICAL DESIGN ANALYSIS

The purpose of mechanical design analysis is to understand and develop a system to ensure acceptable performance. In the design of the alignment assembly, the initial analysis areas include the design of the mirror and actuator interface, coarse positioning system, and fine positioning system. The design of the system components leads to the secondary analysis of determining the stiffness parameters which are applicable to the positioning of the mirror segment throughout the alignment process. Figure 3-1 gives a representation of the analysis process for an alignment assembly design.

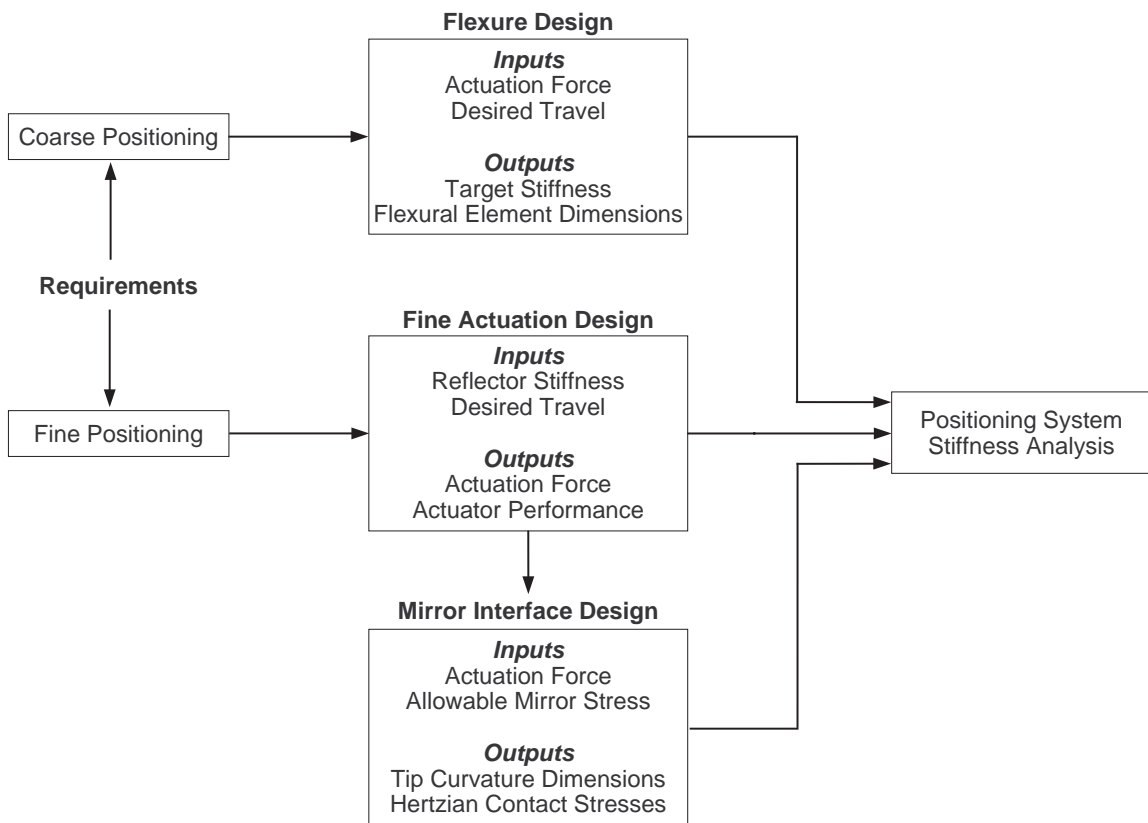


Figure 3-1. Alignment assembly design analysis representation

3.1 Glass Failure Overview

In analyzing the stress for the contact interface between an actuator and glass, it is important to mention the basics of how the glass will likely fail. Glass does not show any plastic deformation prior to failure, which is considered brittle failure. Similar glass samples may display large variations in strength because they fail due to flaws within the glass which are initially dependent on the glass manufacturing or forming process. As opposed to metals, the flaws, or small cracks, in glass grow each time a stress is applied to the glass until a critical crack length is achieved. This continuous damage of the glass results in failure of the glass.

In a flawless brittle solid, a certain amount of work is required to pull apart the atomic forces which are holding the solid together. The stress within the solid will reach a maximum, at which point the bonds between the atoms will break. When the atomic bonds are broken, two new surfaces will be formed which have a fracture surface energy, γ_f [37]. In reality, a brittle solid will contain flaws. When a stress is applied to the solid, stress concentrations form at the tip of the flaws. The stress concentrations cause the stress near to flaw to be high, resulting in the breaking of atomic bonds and the formation of a crack in the solid. With the continued application of stress, the cracks will propagate into a fracture and eventually brittle failure. For plane strain, the failure stress is given by Equation (3-1), where γ_f is the fracture surface energy and c^* is the critical crack length. For plane stress, the $(1-\nu^2)$ term is omitted. This equation is known as Griffith's theory [37].

$$\sigma_f = [\sigma_a]_{failure} = \left[\frac{2\gamma_f E}{(1-\nu^2)\pi c^*} \right]^{1/2} \quad (3-1)$$

In failure analysis of glass, the glass behavior is also influenced by the loading rate, environment, static fatigue, and dynamic fatigue. In terms of static fatigue, the crack growth in a glass will be slower at a lower applied stress. In terms of loading rates and dynamic fatigue, a high stressing rate will result in higher strength results for a specimen, as there is less time for a crack to prorogate. An increasing temperature and humidity level in the ambient environment will cause an increase in the crack propagation velocity and time to failure for a glass substrate under loading [37].

Since the failure of glass primarily occurs by the separation of atomic bonds which results in crack formation, the primary term of interest is the tensile stress that results. In the study of Hertzian contact, the pressing of two bodies together creates a contact pressure. For a circular contact region between two bodies, the maximum tensile stress for failure of brittle materials in general is given as Equation (3-2) [40]. In the design of an interface creating pressure against general brittle materials, Equation (3-3) includes a factor of safety of 1.5 for limiting the maximum allowable Hertzian contact pressure [42].

$$\sigma_{t_{max}} = \frac{(1-2\nu)p_0}{3} \quad (3-2)$$

$$p_{0_{allowable}} = \frac{2\sigma_{allowable}}{1-2\nu} \quad (3-3)$$

Due to the dependence on the defects within the glass from the manufacturing process, a conservative estimate for the strength of glass based on a range of strength

values corresponding to the actual glass manufacturing process is necessary for a determination of the allowable stress. This is particularly important in the use of glass segments slumped to the curved segments for Constellation-X, as the glass strength properties decrease due to the forming process. In initial strength testing of slumped mirror segments for Constellation-X, the resulting strength was found to be 61 +/- 13.9 MPa [38]. Substituting the modulus of elasticity of 0.208 for D263 glass and the range of strength values into Equation (3-3) results in an allowable Hertzian contact pressure range of 161.3-256.5 MPa for a circular contact area. The most conservative contact pressure is therefore 161.3 MPa.

3.2 Hertzian Contact Mechanics

For the application of manipulating the mirror, it is important to maintain point contact for the translation of motion in the radial direction and minimize unwanted distortions in the mirror. By utilizing contact between curved surfaces a point contact is established, which is known as Hertzian contact. The point contact is characterized by a small contact area with highly concentrated stresses between the elastic bodies which is analyzed. The stiffness of the contact between the curved surfaces is used in the analysis of the assembly stiffness.

3.2.1 Hertzian Contact between Curved Surfaces of General Profiles

For the general case of contact between curved surfaces, it is assumed that the bodies are elastic and the surfaces are nonconforming and smooth. The surfaces of the bodies are defined by their principle radii of curvature. R_i' and R_i are the maximum and minimum principle radii of curvature, respectively, and $i=1$ or 2 for the body designation. Figure 3-2 shows the radii of curvature between two curved surfaces in contact.

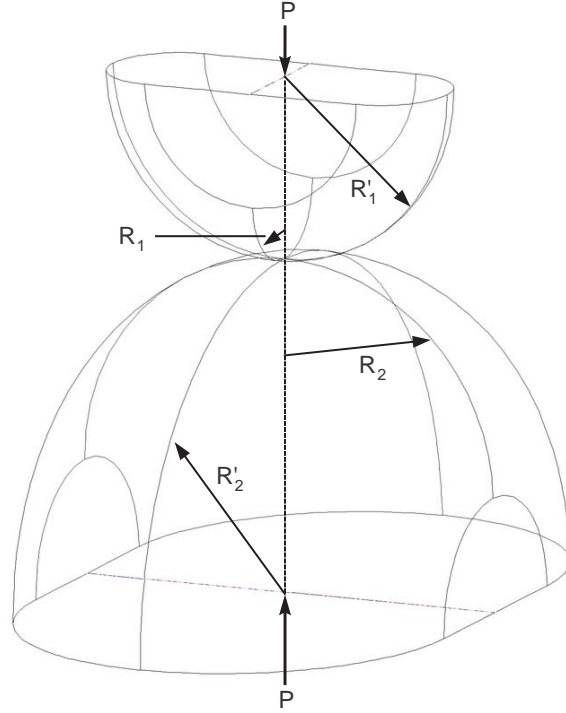


Figure 3-2. Curvatures of two bodies in contact

When the two bodies come into contact, the two bodies deform elastically. The sum of the deformations of each body in the vertical direction, u_{z1} and u_{z2} can be related to the total deformation of the bodies and position from the center of contact by Equation (3-4) .

$$u_{z1} + u_{z2} = \delta + Ax^2 + By^2 \quad (3-4)$$

The constants, A and B, are functions of the radii of curvature of the two bodies and can be determined using Equations (3-5) and (3-6), where θ is the angle between the planes of maximum (or minimum) curvature of the two bodies [44].

$$A = \frac{1}{4} \left(\frac{1}{R_1} + \frac{1}{R_2} + \frac{1}{R_1'} + \frac{1}{R_2'} \right) - \frac{1}{4} \left\{ \left[\left(\frac{1}{R_1} - \frac{1}{R_1'} \right) + \left(\frac{1}{R_2} - \frac{1}{R_2'} \right) \right]^2 - \left[4 \left(\frac{1}{R_1} - \frac{1}{R_1'} \right) \left(\frac{1}{R_2} - \frac{1}{R_2'} \right) \sin^2 \theta \right] \right\}^{1/2} \quad (3-5)$$

$$B = \frac{1}{4} \left(\frac{1}{R_1} + \frac{1}{R_2} + \frac{1}{R_1'} + \frac{1}{R_2'} \right) + \frac{1}{4} \left\{ \left[\left(\frac{1}{R_1} - \frac{1}{R_1'} \right) + \left(\frac{1}{R_2} - \frac{1}{R_2'} \right) \right]^2 - \left[4 \left(\frac{1}{R_1} - \frac{1}{R_1'} \right) \left(\frac{1}{R_2} - \frac{1}{R_2'} \right) \sin^2 \theta \right] \right\}^{1/2} \quad (3-6)$$

The equivalent radius of curvature, R_e , can be determined using Equation (3-7) [40]. For the convention shown, it is assumed that a convex surface has a positive radius, whereas a concave surface would be denoted by a negative radius.

$$R_e = \frac{1}{2} (AB)^{-1/2} \quad (3-7)$$

According to Hertzian contact theory, the contact area is an ellipse defined by a and b , the major and minor radii, respectively. For a complete solution, the use of elliptic integral functions is necessary. Equations (3-8) and (3-9) define the complete elliptical integrals of the first and second kind, $K(e)$ and $E(e)$, where the eccentricity, e , is considered the elliptic modulus [39].

$$K(e) = \int_0^{\pi/2} \frac{d\phi}{\sqrt{1 - e^2 \sin^2 \phi}} \quad (3-8)$$

$$E(e) = \int_0^{\pi/2} \sqrt{1 - e^2 \sin^2 \phi} d\phi \quad (3-9)$$

Equation (3-10) defines the eccentricity of the ellipse as a function of the semimajor and semiminor axes [40].

$$e = \sqrt{1 - (b/a)^2} \quad (3-10)$$

The constants A and B can be used to determine the dimensions of the ellipse of contact by solving Equation (3-11).

$$\frac{B}{A} = \frac{(a/b)^2 E(e) - K(e)}{K(e) - E(e)} \quad (3-11)$$

For close approximations, it has been shown by Johnson that the ratio of elliptical axes is approximately related to the constants A and B by Equation (3-12) [40]. It should be noted that the approximate relationship given in Equation (3-12) becomes less accurate as the value of (B/A) increases.

$$\frac{b}{a} \approx \left(\frac{B}{A}\right)^{-2/3} \quad (3-12)$$

The determination of several correction factors is useful in characterizing the compression and maximum pressure for the two bodies in contact. The correction factors, $F_1(e)$, $F_2(e)$, and $F_3(e)$ can be calculated using elliptical integrals and the ratio of the axes of the contact ellipse using Equations (3-13)-(3-15) [40,41].

$$F_1(e) = \left[\frac{16}{\pi^2 e^4} \left(\frac{b}{a}\right)^3 \left\{ \left(\frac{a}{b}\right)^2 E(e) - K(e) \right\} \{K(e) - E(e)\} \right]^{1/6} \quad (3-13)$$

$$F_2(e) = \frac{2}{\pi} \left(\frac{b}{a}\right)^{1/2} \frac{K(e)}{F_1(e)} \quad (3-14)$$

$$F_3(e) = F_1(e)^{-2} \quad (3-15)$$

Assuming the two bodies in contact are elastic, the equivalent modulus of elasticity, E_e , can be determined using Equation (3-16) [42].

$$E_e = \frac{1}{\frac{1-\nu_1^2}{E_1} + \frac{1-\nu_2^2}{E_2}} \quad (3-16)$$

The total compression of the two bodies can be calculated using Equation (3-17), where P is the applied load.

$$\delta = \left(\frac{9P^2}{16E_e^2 R_e} \right)^{1/3} F_2(e) \quad (3-17)$$

The stiffness in the direction of the applied load is defined as the derivative of the load with respect to the deflection and is shown as Equation (3-18), and is also the inverse of the compliance [43].

$$k = \frac{dP}{d\delta} = \frac{2E_e(\delta \cdot R_e)^{1/2}}{F_2(e)^{3/2}} \quad (3-18)$$

The distribution of pressure over the contact area is semi-ellipsoidal. The maximum contact pressure between the two bodies is found at the center of the contact area and is given in Equation (3-19).

$$p_0 = \frac{3P}{2\pi ab} = \left(\frac{6PE_e^2}{\pi^3 R_e^2} \right)^{1/3} F_3(e) \quad (3-19)$$

Within the area of contact, the resultant stresses are compressive. Equations (3-20) and (3-21) define the stress components at the center of contact.

$$\sigma_x = -p_0 \{2\nu + (1 - 2\nu)b/(a + b)\} \quad (3-20)$$

$$\sigma_y = -p_0 \{2\nu + (1 - 2\nu)a/(a + b)\} \quad (3-21)$$

For the case of brittle materials, such as the glass used for mirror segments, the most important area of stress is found at the edge of contact. The radial and circumferential directions exhibit equal tension and compression, respectively. The

resulting stress at the ends of the semimajor axis ($x = \pm a, y = 0$) is given in Equation (3-22) [40].

$$\sigma_x = -\sigma_y = p_0(1 - 2\nu) \frac{b}{ae^2} \left(\frac{1}{e} \tanh^{-1} e - 1 \right) \quad (3-22)$$

The resulting stress at the ends of the semiminor axis ($x = 0, y = \pm b$) is given in Equation (3-23) [40].

$$\sigma_x = -\sigma_y = p_0(1 - 2\nu) \frac{b}{ae^2} \left(1 - \frac{b}{ae} \tan^{-1} \left(\frac{ea}{b} \right) \right) \quad (3-23)$$

The shear stress occurs along the axis of contact between the two bodies beneath the surface. The use of shear stress in failure analysis is primarily important for the failure of ductile materials. The depth at which the maximum shear stress occurs is a function of the radii of the contact ellipse [40]. For the general case of a circular contact area with radius a , the maximum shear stress and location beneath the surface may be found using Equation (3-24).

$$\tau_{\max} = 0.31p_0 = \frac{0.47P}{\pi a^2} \quad (3-24)$$

$$z = 0.48a \quad (\text{for } \nu = 0.3)$$

The use of Hertzian contact analysis has assumed that the topography of the surfaces in contact is smooth. In application, the surface roughness of the interfacing bodies plays a role in affecting the actual pressure distribution. If a surface contains discontinuities, the discontinuities will have peaks and valleys. The initial contact between the bodies with discontinuities will occur initially only at the tips of the discontinuities, which will then be compressed due to the pressure. The bodies with

discontinuities will have a larger contact area than the contact of nominally smooth bodies due to the contact of the discontinuity peaks outside of the nominal contact area assumed by Hertzian contact theory. As a result, the effect of surface discontinuities is that the maximum contact pressure is decreased by spreading the applied load over a larger contact area. The implication of this decreased contact pressure is that the maximum contact pressure predicted by Hertzian contact for smooth surfaces may be used with only a few percent error if the combined roughness of the bodies in contact is less than approximately five percent of the compression of the bodies [40]. In the case of parts machined using electro discharge machining (EDM) techniques, the surface finishes may vary from 1 to 10 μm for the centerline average, R_a . This value is significantly higher than the worst case compression of bodies, which is approximately 30 nm. For a grade 25 spherical ball, the surface finish is approximately 50 nm R_a . The surface roughness of the mirror surface is on the order of 0.3-0.6 nm [10]. Due to the surface roughness of primarily the ball and wire-edm surfaces, the actual contact pressure will be less than the maximum Hertzian contact pressure. For the given values of roughness and compression of bodies, the actual contact pressure should be at least 50% less than the given Hertzian contact pressure [40].

While the effect of surface discontinuities may have benefits in reducing the effective contact pressure and stress, the surface discontinuities create additional problems in the actuation of mirror segments. Surface discontinuities between actuation surfaces may cause an increase in the friction acting against the motion, which may impart unwanted constraint and limit the ability to move the mirror in only the desired

radial direction. If the surface roughness becomes increasingly large, local moments may be created between the peaks and valleys of the actuation surface.

3.2.2 Force Determination for Contact Analysis

Prior to performing contact analysis, the appropriate forces must be determined. Due to the geometry of the reflectors, the stiffness opposing the actuator varies for different actuation points. Finite element analysis is used to determine the stiffness by determining the amount of force necessary to move an actuation point a certain radial distance while imposing appropriate constraints on the remaining actuation points. For modeling, it is assumed that the maximum distance is 63.5 μm and that the mirror stiffness is linear over this distance. Table 3-1 gives the results for the finite element analysis for the mirror segment size used for the piezoelectric actuator alignment assemblies. Additional finite element analysis parameters for these results are given in Appendix D.

Table 3-1. Mirror segment stiffness results from finite element analysis (494 series secondary mirror) [60]

Location	θ ($^\circ$)	Force (N)	$k_{g\theta}$ (N/m)
B1	-24.50	0.00019	2.93
B2	-12.25	0.00641	100.94
B3	0	0.00699	110.05
B4	12.25	0.00641	100.94
B5	24.50	0.00019	2.93
U1	-24.50	0.00018	2.84
U2	-12.25	0.00621	97.72
U3	0	0.00676	106.48
U4	12.25	0.00621	97.72
U5	24.50	0.00018	2.84

3.2.3 Glass Interface Hertzian Contact

The curvature of the mirror segments used in the Constellation-X features a convex and concave side. It is important to achieve a point contact interface to avoid adding unwanted moments. The point contact achieved using the design shown in Figure 3-3 can be modeled as cylinders at right angles for the convex side and a sphere within a cylindrical race case for the concave side of the mirror.

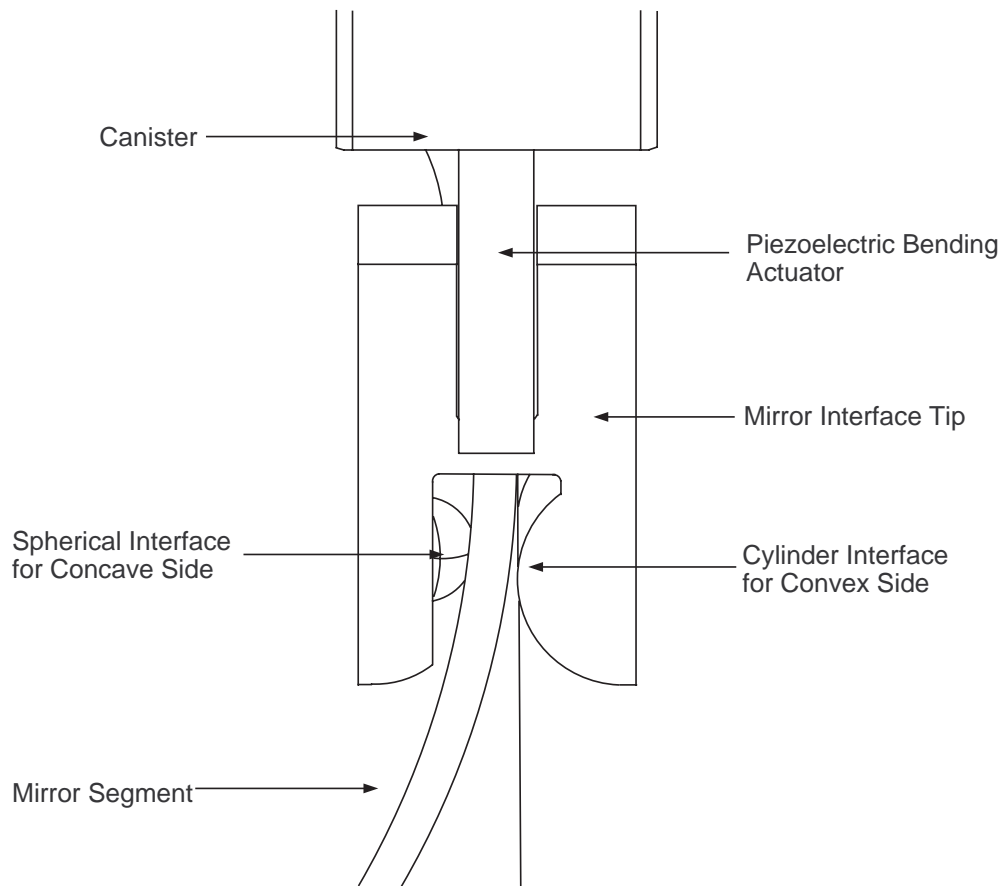


Figure 3-3. Actuator to mirror interface tip with point contact

For the two interface cases, simplified formulas are available for analyzing the Hertzian contact and resulting compressive stress from Pilkey [44]. For the simplified formulas, the inverse of the equivalent stiffness, E_e , given in Equation (3-16), is denoted by γ , and is given in Equation (3-25).

$$\gamma = \frac{1-\nu_1^2}{E_1} + \frac{1-\nu_2^2}{E_2} \quad (3-25)$$

For the case of the cylinders crossed at right angles, Figure 3-4 shows the applicable dimensions [44]. For the case of the mirror and tip interface, D_1 is the diameter of the actuator tip while D_2 is diameter of the mirror segment at the given axial distance of actuation.

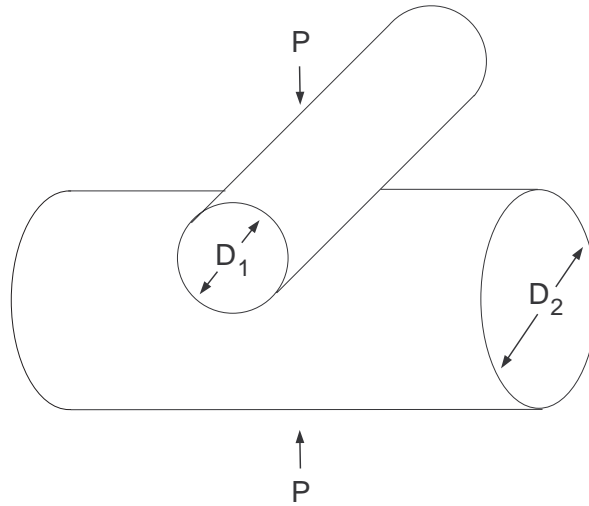


Figure 3-4. Hertzian contact of cylinders crossed at right angles

For characterizing the case of cylinders crossed at right angles, several coefficients are required. The coefficients n_a , n_b , n_c , and n_d are available in tabular form in [44]. The equations for calculating the coefficients involving elliptic integrals are also available. Using the definition of the elliptical integrals given in Equation (3-8), the coefficients can then be calculated using Equations (3-26) through (3-30) [44].

$$k = \frac{b}{a} \quad (3-26)$$

$$n_a = \frac{1}{k} \left(\frac{2kE(e)}{\pi} \right)^{1/3} \quad (3-27)$$

$$n_b = \left(\frac{2kE(e)}{\pi} \right)^{1/3} \quad (3-28)$$

$$n_c = \frac{1}{E(e)} \left(\frac{\pi^2 k E(e)}{4} \right)^{1/3} \quad (3-29)$$

$$n_d = \frac{K(e)}{[E(e)]^{1/3}} \left(\frac{2k}{\pi} \right)^{2/3} \quad (3-30)$$

As can be seen by the associated equations, the elliptical equations and calculations involved in the exact solution can become very involved. For initial analysis, it may be beneficial to use available tabulated values available from Pilkey, from which several rows of data are shown in Table 3-2 for several values of A/B typical of the tip interface design for the cylindrical race (large A/B) and crossed cylinders (small A/B) [44].

Table 3-2. Constants for use in contact equations [44]

A/B	n_a	n_b	n_c	n_d
1.000000	1.000000	1.000000	1.000000	1.000000
0.965467	1.013103	0.987137	0.999929	0.999952
0.928475	1.025571	0.975376	0.999684	0.999714
0.006266	7.142177	0.299092	0.468127	0.406537
0.005391	7.567233	0.290498	0.454903	0.391004
0.004570	8.062065	0.281372	0.440832	0.374507
0.003805	8.647017	0.271621	0.425766	0.356910

For the case of cylinders crossed at right angles, the ratio A/B for using Table 3-2 can be determined using Equation (3-31).

$$A = \frac{1}{D_2} \quad B = \frac{1}{D_1} \quad (3-31)$$

$$\frac{A}{B} = \frac{D_1}{D_2}$$

Due to the small size of the tips with respect of the radius of curvature of the mirror segments, the tabulated values available may not offer sufficient entries for the small changes in possible tip diameters used. For this reason, all tabulated data available from Pilkey for various ratios of A/B is curve-fitted for calculation and comparison of tip diameters. The tabulated data for n_a closely follows a power function for all values of A/B ($R^2=0.9998$). For the coefficients n_b , n_c , and n_d , the tabulated data closely follows a power function for values of $A/B < 0.05$ and a fourth-order polynomial for the remaining values of A/B between 0.05 and 1 ($R^2 \geq 0.9994$). The form of the equations for the coefficients is given in Equations (3-32)-(3-34). The associated parameters are given in Table 3-3.

$$n_a, n_b, n_c, n_d = 1 \quad \frac{A}{B} = 1 \quad (3-32)$$

$$n_i = x_1 \left(\frac{A}{B} \right)^{x_2}, \quad \frac{A}{B} < 1 \text{ for } i = a, \frac{A}{B} < 0.05 \text{ for } i = b, c, d \quad (3-33)$$

$$n_i = x_3 \left(\frac{A}{B} \right)^5 + x_4 \left(\frac{A}{B} \right)^4 + x_5 \left(\frac{A}{B} \right)^3 + x_6 \left(\frac{A}{B} \right)^2 + x_7 \left(\frac{A}{B} \right) + x_8 \quad (3-34)$$

$$0.05 < \frac{A}{B} < 1 \text{ for } i = b, c, d$$

Table 3-3. Parameters for coefficient curve-fit equations

Term	n_a	n_b	n_c	n_d
x_1	0.9727	0.8266	1.2329	1.4192
x_2	-0.3927	0.2006	0.1909	0.2462
x_3	N/A	2.2461	3.9737	4.7254
x_4	N/A	-6.7483	-11.856	-14.043
x_5	N/A	7.8948	13.797	16.227
x_6	N/A	-4.6986	-8.081	-9.3705
x_7	N/A	1.9333	2.5799	2.9111
x_8	N/A	0.3761	0.595	0.5607

After determining the necessary coefficients, the semimajor and semiminor axes of the contact ellipse and the rigid distance of approach of the two bodies can be found using Equation (3-35) [44].

$$\begin{aligned}
 a &= 0.909 n_a (PK \gamma)^{1/3} \\
 b &= 0.909 n_b (PK \gamma)^{1/3} \\
 \delta &= 0.825 n_d \left(\frac{P^2 \gamma^2}{K} \right)^{1/3} \\
 K &= \frac{D_1 D_2}{D_2 + D_1}
 \end{aligned} \tag{3-35}$$

If the term n_d has been determined, the stiffness of the contact interface is the inverse of the compliance and given as Equation (3-36).

$$k = \frac{dP}{d\delta} = \frac{3}{2\gamma} \left(\frac{K\delta}{(0.825)^3 n_d^3} \right)^{1/2} \tag{3-36}$$

The maximum compressive stress is given by Equation (3-37).

$$\sigma_c = 0.579 n_c \left(\frac{P}{K^2 \gamma^2} \right)^{1/3} \tag{3-37}$$

The values of the semimajor and semiminor axes, along with the load, can be entered into Equation (3-19) to determine the maximum contact pressure. This value can be compared to the allowable contact pressure given in Equation (3-3).

Due to the large difference between the radius of the mirror and the radius of the contact cylinder used for the contact stress approximation, the actual dimensions of the contact area are elliptical, which results in different tensile stresses at the ends of the semimajor and semiminor axes. Given the contact pressure and dimensions of the elliptical contact area, Equations (3-22) and (3-23) can be used to determine the tensile stress. The maximum tensile stress occurs at the end of the semimajor axis for the dimensions given. Figure 3-5 shows the maximum contact pressure for several loads when using a titanium cylindrical tip on the convex side of the mirror. The loads used correspond to the approximate loads from the finite element analysis given in Table 3-1. The resulting stress in the glass at the semimajor and semiminor axes is shown in Figure 3-6 and Figure 3-7, respectively. Of note is the significantly decreased tensile stress for the right cylinders as opposed to the sphere contacting the concave side of the mirror due to the increased contact area. For the selection of tip dimensions, the use of crossed cylinders allows selection of dimensions at least as low as 0.1 mm in diameter for the conservative Hertzian contact analysis. For the PPII tips, a diameter of 2 mm was used for the cylindrical portion of the tip.

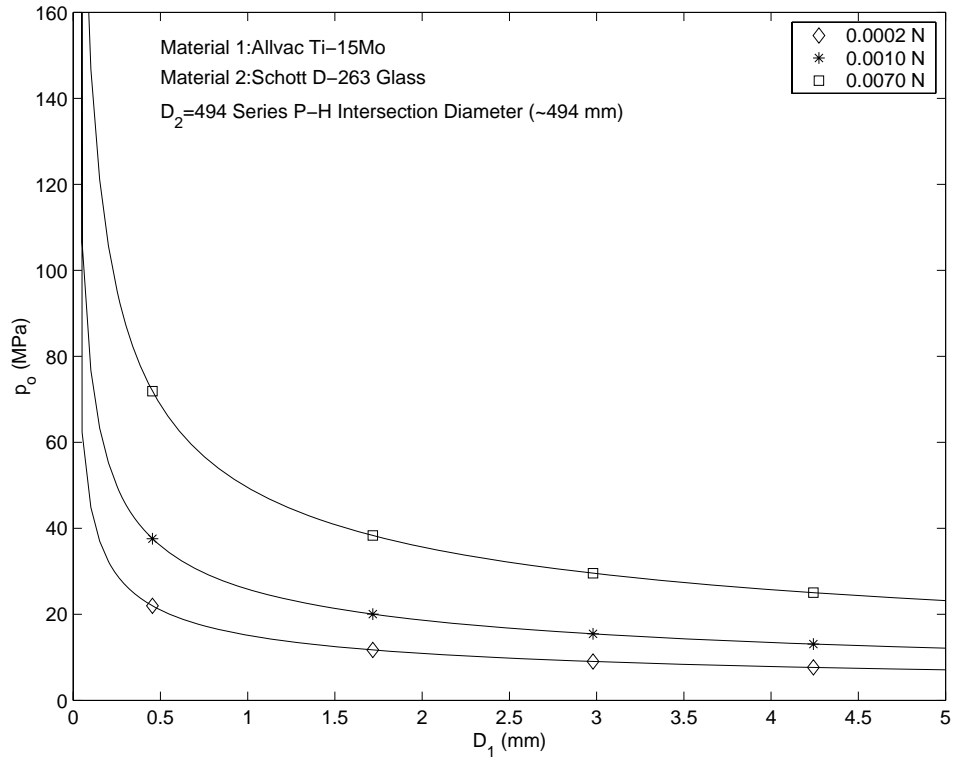


Figure 3-5. Maximum contact pressure for Hertzian contact of crossed cylinders

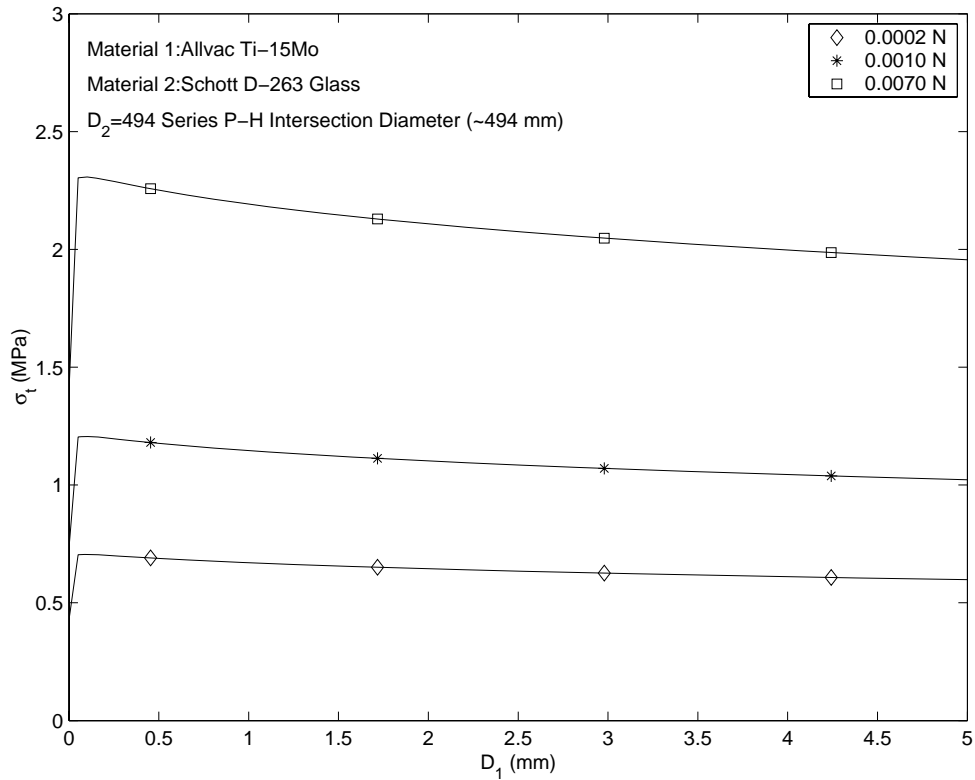


Figure 3-6. Glass tensile stress at the semimajor axis end for crossed cylinder Hertzian contact

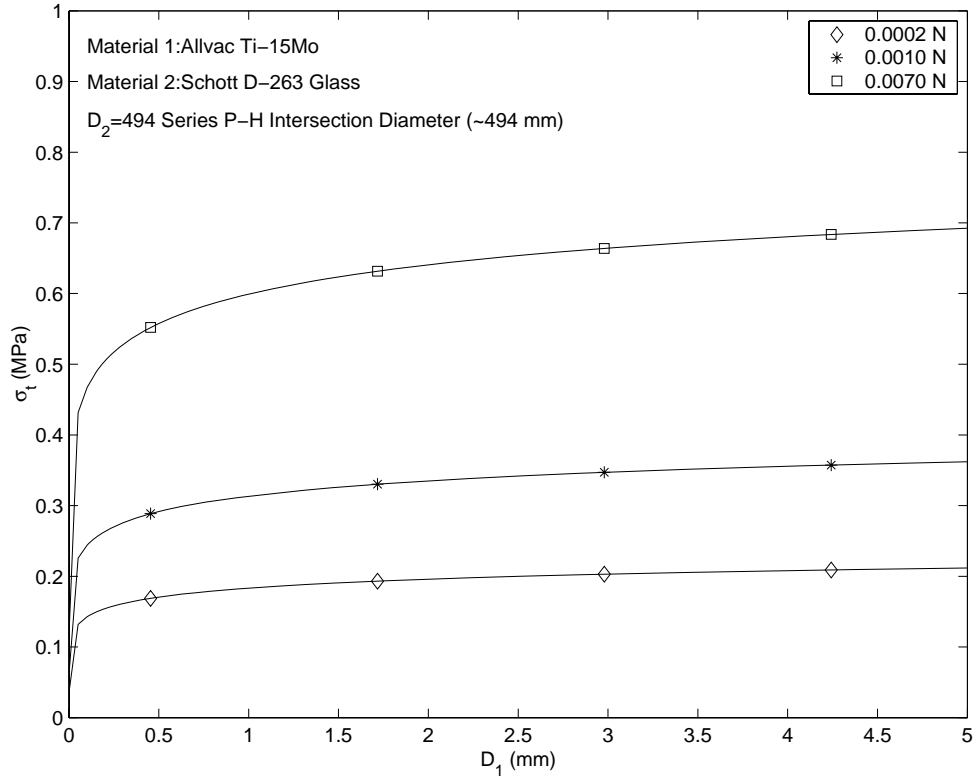


Figure 3-7. Glass tensile stress at the semiminor axis end for crossed cylinder Hertzian contact

For the case of a sphere within a cylindrical race, the process is very similar to the crossed cylinders case. Figure 3-8 shows the parameters for this case.

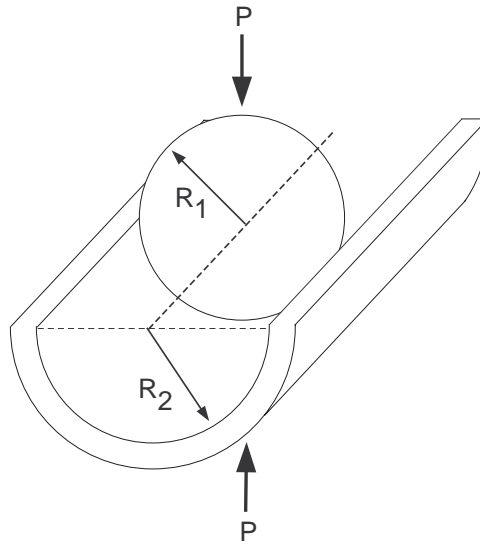


Figure 3-8. Hertzian contact of a sphere in a cylindrical race

The values of A and B to be used with Table 3-2 and the Equations (3-32)-(3-34) are given in Equation (3-31).

$$A = \frac{1}{2} \left(\frac{1}{R_1} - \frac{1}{R_2} \right), \quad B = \frac{1}{2R_1} \quad (3-38)$$

After determining the necessary coefficients, the semimajor and semiminor axes of the contact ellipse and the rigid distance of approach of the two bodies can be found using Equation (3-39) [44].

$$\begin{aligned} a &= 1.145 n_a (PK \gamma)^{1/3} \\ b &= 1.145 n_b (PK \gamma)^{1/3} \\ \delta &= 0.655 n_d \left(\frac{P^2 \gamma^2}{K} \right)^{1/3} \\ K &= \frac{R_1 R_2}{2R_2 + R_1} \end{aligned} \quad (3-39)$$

The stiffness of the contact interface is given as Equation (3-40).

$$k = \frac{dP}{d\delta} = \frac{3}{2\gamma} \left(\frac{K\delta}{(0.655)^3 n_d^3} \right)^{1/2} \quad (3-40)$$

The maximum compressive stress is given by Equation (3-41).

$$\sigma_c = 0.579 n_c \left(\frac{P}{K^2 \gamma^2} \right)^{1/3} \quad (3-41)$$

The dimensions of the contact area are elliptical, though they are very near circular due to the likely dimensions of the tip and glass. The values of the semimajor and semiminor axes, along with the load, can be entered into Equation (3-19) to determine the maximum contact pressure. This value can be compared to the allowable

contact pressure given in Equation (3-3). . Given the contact pressure and dimensions of the elliptical contact area, Equations (3-22) and (3-23) can be used to determine the tensile stress. Figure 3-9 shows the maximum contact pressure for several loads when using a synthetic sapphire sphere on the concave side of the mirror. Based on the estimated allowable circular contact pressure of 161.3 MPa, the corresponding selection of sphere diameters is limited to greater three millimeters. It is important to keep in mind that this is for ideal Hertzian contact and the worst case strength value of the glass samples tested. For the tips used in PPI and PPII, spheres of 1 mm diameter were used to accommodate size limitation, assuming that the significant surface discontinuities as compared with the compression of the bodies will decrease the actual contact pressure.

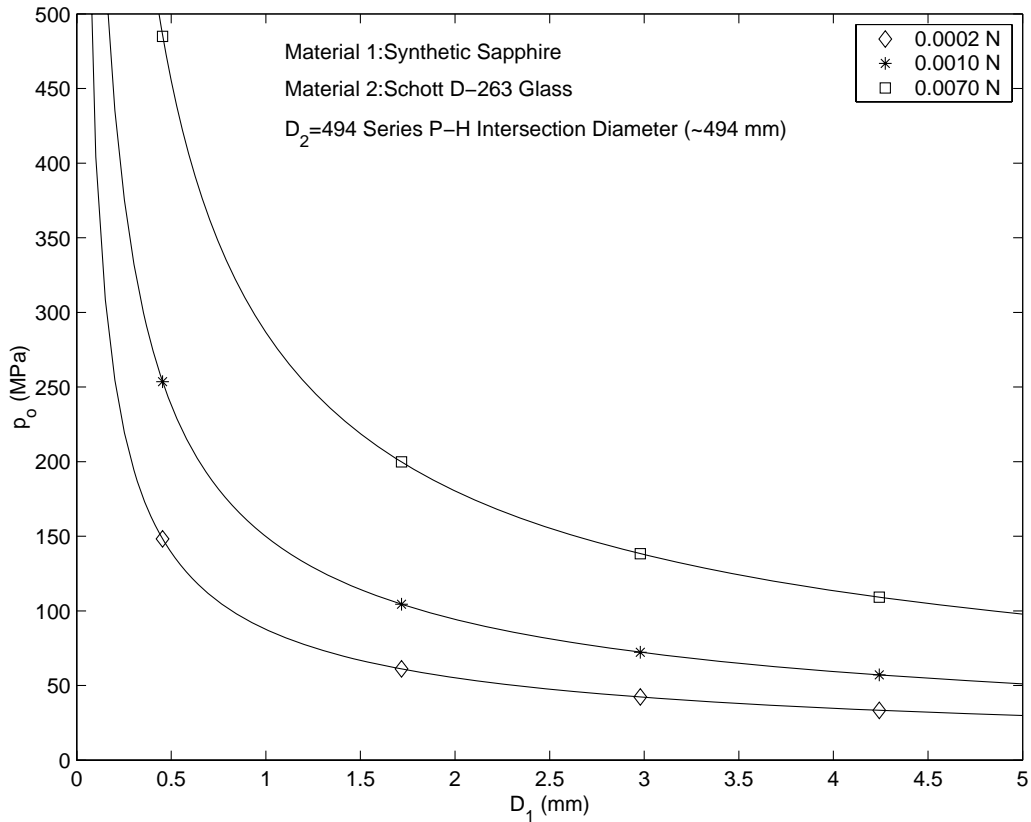


Figure 3-9. Maximum contact pressure for Hertzian contact of a sphere within a cylindrical race

Equations (3-22) and (3-23) can be used to determine the tensile stress in the glass. The stresses at the semiminor axes are slightly higher for this case and given dimensions. Figure 3-10 shows the maximum tensile stress in the glass at the end of the semiminor axis which can be used for the appropriate sphere diameter. It should be of note that the stresses created from this configuration are significantly higher than the convex side since the contact area of the sphere within the cylindrical race is less than the two crossed cylinders configuration.

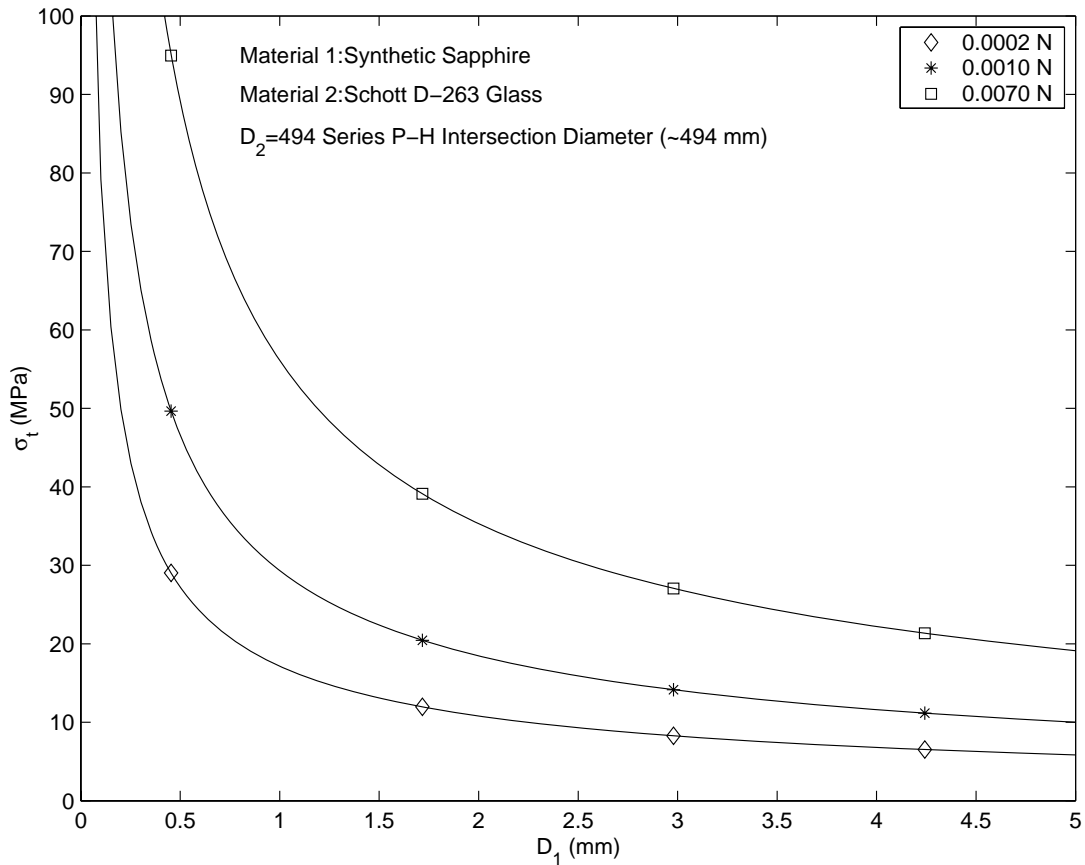


Figure 3-10. Tensile stress at the semiminor axis for Hertzian contact of a sphere within a cylindrical race

Hertzian contact analysis assumes semi-infinite bodies. However, the mirror has a limited thickness (0.4 mm). Although the mirror is only loaded from one side of a tip at a time, the depth of the stress distribution should be considered. This consideration is to

ensure that the actual stresses are not significantly higher due to the semi-infinite body assumption. For a circular contact area, the stress in the radial and circumferential direction extends down to approximately 1.5 times the contact radius, with the compressive stress region extending further and decreasing in magnitude [40]. For the case of a 1 mm ball in contact with 0.007 N of force on the concave side of the mirror, the contact radius is $\sim 3.3 \mu\text{m}$, resulting in depth of stress in the radial and circumferential direction which extends down to approximately $5 \mu\text{m}$.

3.2.4 Coarse Flexure Drive Coupling Hertzian Contact

The coarse flexure drive coupling utilizes a sphere within a spherical socket. For the case of a sphere within a spherical socket, Figure 3-11 shows the applicable dimensions [44]

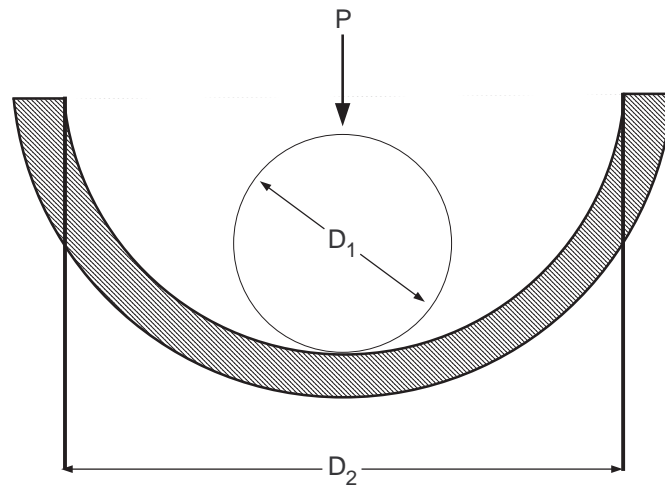


Figure 3-11. Sphere in spherical socket

For this case, the semimajor and semiminor axis of the contact ellipse, a and b are equal to each other and defined by Equation (3-42) [44].

$$a = b = 0.721(P K \gamma)^{1/3}$$

$$K = \frac{D_1 D_2}{D_2 - D_1} \quad (3-42)$$

The rigid distance of approach between the contacting bodies is given by Equation (3-43).

$$\delta = 1.040 \left(\frac{P^2 \gamma^2}{K} \right)^{1/3} \quad (3-43)$$

The stiffness of the contact interface is given as Equation (3-44).

$$k = \frac{dP}{d\delta} = \frac{3}{2\gamma} \left(\frac{K\delta}{(1.04)^3} \right)^{1/2} \quad (3-44)$$

The maximum compressive stress is given by Equation (3-45) for analysis of the ductile solid.

$$\sigma_c = 0.918 \left(\frac{P}{K^2 \gamma^2} \right)^{1/3} \quad (3-45)$$

For analysis of a brittle solid, the tensile stress values for may be determined using the same process as done for the mirror interface calculations. The values of the semimajor and semiminor axes, along with the load, can be entered into Equation (3-19) to determine the maximum contact pressure. Given the contact pressure and dimensions of the elliptical contact area, Equations (3-22) and (3-23) can be used to determine the tensile stress.

In the positioning of the radial struts, the struts feature opposing fine pitch adjusters. The opposite fine pitch adjuster may be used as a constraint for the strut

position. In the constraint of the radial position of the strut, the opposing forces will cause a deformation in the interface between the jewel bearing and adjuster which is of importance. Figure 3-12 shows the deformations for varying opposing loads at the contact point for varying interface ball diameters made of 18-8 stainless steel.

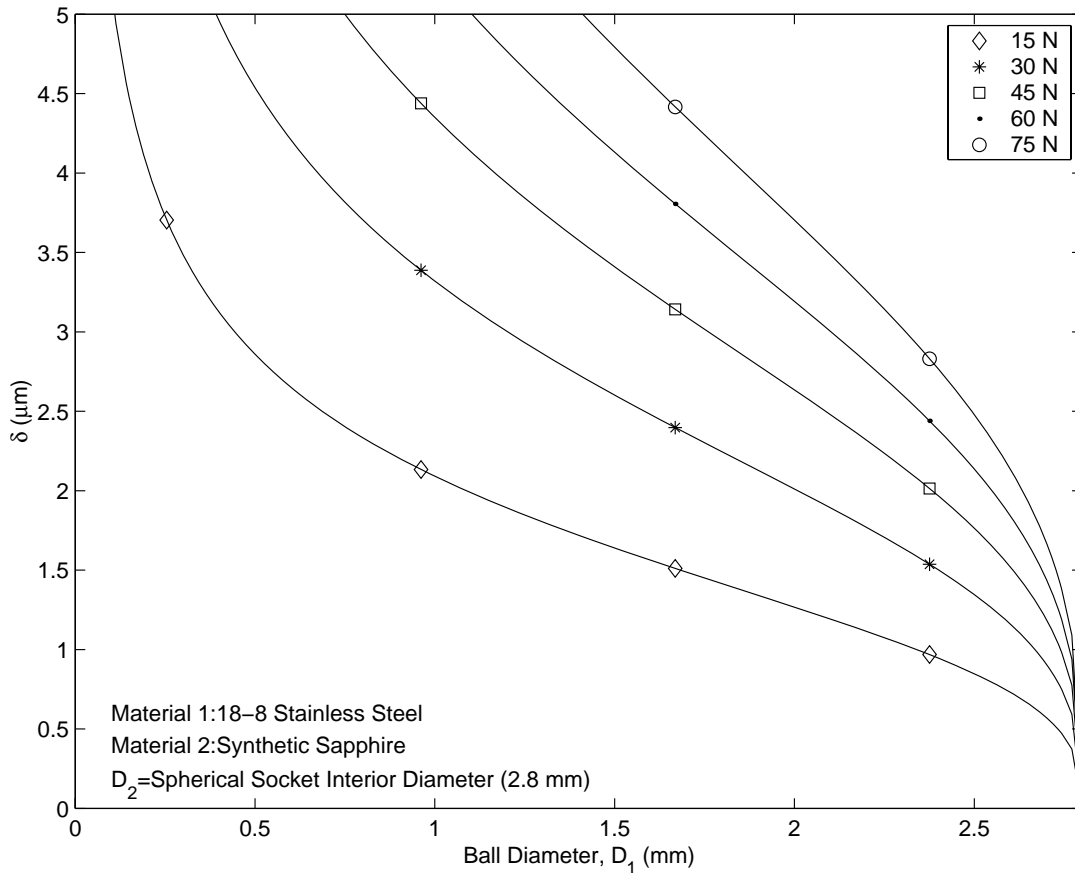


Figure 3-12. Deformation due to an applied load for Hertzian contact of a sphere within a spherical socket

For the application of a rotating fine pitch adjuster, torsion results from the friction between the bodies at the contact area. For the case of a sphere within a spherical socket, the contact area is circular with radius a . Assuming that one body is constrained to prevent rotation, the moment created by the applied load, P , with a coefficient of friction μ is given in Equation (3-46) [40].

$$M = \frac{3\pi\mu Pa}{16} \quad (3-46)$$

This moment attempts to twist the flexure strut about the radial direction of motion. For application, a low coefficient of friction interface between the adjuster and positioning strut is desired. The coefficient of friction between the 18-8 stainless steel tip of the adjuster and synthetic sapphire of the spherical socket is 0.15 [33]. Given a load, P , of 10 N, the contact area radius, a , is 57.9 μm . This results in a moment of 5.113×10^{-5} N-m. If a lower coefficient of friction is necessary, the lubrication of this interface may be feasible provided the lubricant is certified for use in a vacuum environment.

3.3 Flexural Bearing Strut Design

The use of flexural elements which are capable of providing linear motion is an approach to the positioning of actuators which is intended to simplify the initial alignment process and allow for predictable performance. In determining the type of flexure design to use for the coarse actuation of struts for mirror segments, several desired features were considered:

- Monolithic titanium structure manufactured using wire-EDM techniques
- Limited blockage of the reflected beam from the mirror surface
- Simplicity of features
- Travel range of 0.4 mm
- High out-of-plane stiffness

In addition, for the design of the PPII, the flexure design needed to fit compactly onto existing OAP-2 housings. A common flexural setup which has been widely used in achieving single degree of freedom linear motion is the double compound, notch type rectilinear spring [45]. This type of flexure assembly was discussed in section 1.5 and

may also be achieved using beam elements. The one drawback to implementing this type of design in an integrated structure with the actuators is that the coupled flexural hinges on each side add additional material and creates additional blockage of the mirror collecting surface. This extra blockage is undesirable for x-ray collection capabilities as well as limiting the area that can be used for alignment of the mirror segment. For this reason, a similar design which does not couple the flexural bearings was demonstrated using notch type flexures by Becker [46]. By not coupling the flexural elements, the flexure assembly is not ideally constrained to only one degree of freedom. However, by utilizing a symmetric design, precise manufacturing, and actuating through the center of stiffness, the flexure assembly can produce near single degree of freedom translation. A design using beam elements was suggested by Smith [47]. This type of flexure translation stage utilizes four separate two-beam, two-axis hinges.

Since the flexure system is used as a coarse positioning system for the actuators, the pseudo single degree of freedom design is an acceptable tradeoff which allows for increased collecting and alignment area while still improving over the independent strut design. Figure 3-13 shows a two dimensional schematic of this type of translation stage. Due to the limited travel, two actuations points are used to allow for full travel of the flexure in both directions by using only one at a time. If less travel is required, an intentional offset in the designed placement of the actuators allows for the use of actuation in only one direction.

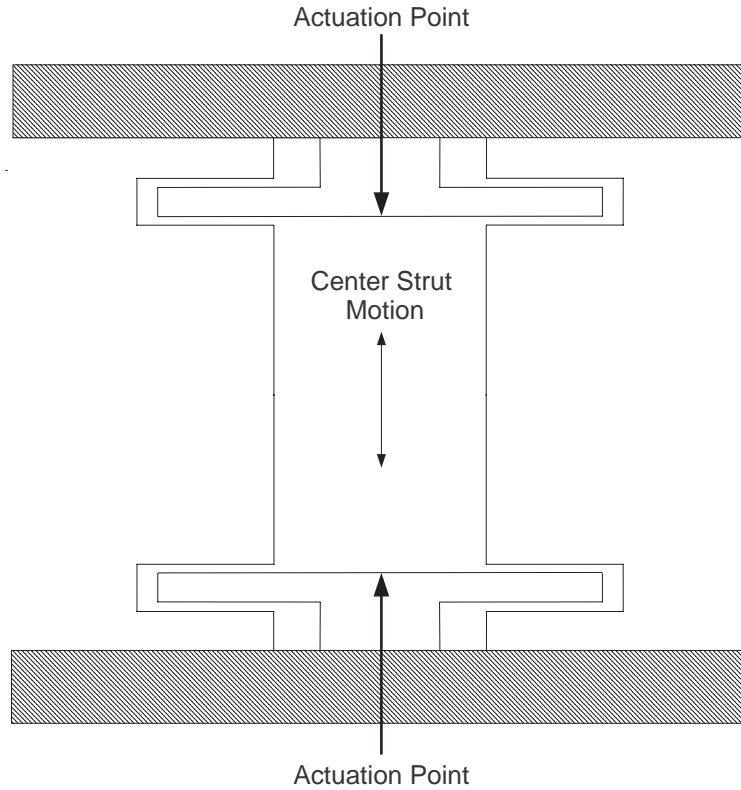


Figure 3-13. Flexural translation stage schematic utilizing two-beam, two-axis hinges

The parameters involved in the design of the two-beam, two-axis hinges are shown in Figure 3-14.

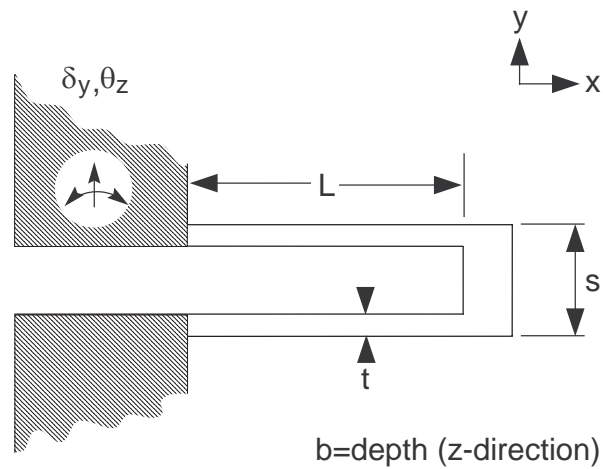


Figure 3-14. Design parameters for a two-beam, two-axis flexure

In the design of the flexure translation stage, the two main factors that will influence the dimensions are the amount of force that is available to drive the stage which limits the actuation direction stiffness and the magnitude of stress that is allowable for the members. The first step in the design of the flexure system is recognizing that the links of the system that will be deformed in the elastic range are the two cantilever beams which are subject to a transverse force plus a bending moment at the free end. There is a bending moment at the free end because the two cantilever beams are connected by a rigid beam which imposes a zero slope condition at the free end. For these boundary conditions, the stiffness of an individual beam is given in Equation (3-47).

$$k_{\delta_y, F_y, (beam)} = \frac{12EI_z}{L^3} \quad (3-47)$$

Since there are two cantilevers with these boundary conditions connected in series, the stiffness of a flexure element as seen in Figure 3-14 is equal to half of the stiffness of each cantilever. The stiffness of the flexure element is given in Equation (3-48) [46].

$$k_{\delta_y, F_y, (element)} = \frac{6EI_z}{L^3} \quad (3-48)$$

In order to determine the equivalent stiffness in the y-direction of the entire translation device shown in Figure 3-13, the stiffness of the individual flexure elements are summed together, as all four are acting in parallel against a force applied at one of the actuation points. The resulting stiffness, including the expansion of the area moment of inertia term is given in Equation (3-49).

$$k_{\delta_y F_y} = \frac{24EI_z}{L^3} = \frac{2Ebt^3}{L^3} \quad (3-49)$$

The out-of-plane stiffness for a force in the z-direction for the flexure assembly can be modeled in a similar manner as the directional stiffness, in that the two individual beams act in series under the boundary condition of zero slope on the ends and the four elements act in parallel. This is assuming the stiffness of the connecting members is much greater than the flexural elements, and therefore may be considered rigid bodies. The resulting out-of-plane stiffness for the entire translation stage is given in Equation (3-50). As would be expected, a high out-of-plane stiffness is most readily achievable by minimizing the length and increasing the depth.

$$k_{\delta_z F_z} = \frac{24EI_y}{L^3} = \frac{2Et b^3}{L^3} \quad (3-50)$$

The maximum deflections of a single flexure as seen in Figure 3-14 can be written in terms of a specified design stress, σ_d . The design stress limited maximum deflection is given in Equation (3-51) [46].

$$\delta_{y_{\max}} = \frac{2\sigma_d L^2}{3Et} \quad (3-51)$$

The target stiffness of the flexure can be defined by the actuation force available and the desired displacement, as shown in Equation (3-52).

$$k_{\delta_y F_y (design)} \leq \frac{F_y}{\delta_{y design}} \quad (3-52)$$

By specifying the desired depth of the flexure, the flexure dimensions can be selected to meet both the stress and stiffness requirements. For the stiffness requirements, combining Equations (3-49) and (3-52) and rearranging terms results in the flexure length written as a function of the thickness, as shown in Equation (3-53).

$$L > \left(\frac{2Ebt^3 \delta_{y_{design}}}{F_y} \right)^{1/3} \quad (3-53)$$

In order to meet the design stress requirement, assuming the deflection is less than the maximum deflection, rearranging Equation (3-51) in terms of the length as a function of the thickness results in Equation (3-54).

$$L > \left(\frac{3Et\delta_{y_{design}}}{2\sigma_d} \right)^{1/2} \quad (3-54)$$

It is also advisable to avoid making the flexure thickness too small. If the thickness is specified very low, the machining tolerances may be of concern as the variance in the manufactured thicknesses may cause large differences in stiffness between flexure elements. The design space of the flexure parameters can then be plotted against the contour lines of out-of-plane stiffness values as given in Equation (3-50). The dimensions may be selected by maximizing the out-of-plane stiffness, while still meeting stress, stiffness, and any associated manufacturing requirements necessary. Figure 3-15 shows the design space used in the selection of the flexure parameters for the PPII. The allowable dimensions lie in the section between the constraints lines, as shown in the area designated with vertical lines. Although the dimension may be selected from anywhere

in this area, it is preferable to select dimensions in the lower parts of this area, which corresponds to a larger out-of-plane stiffness for the flexure system.

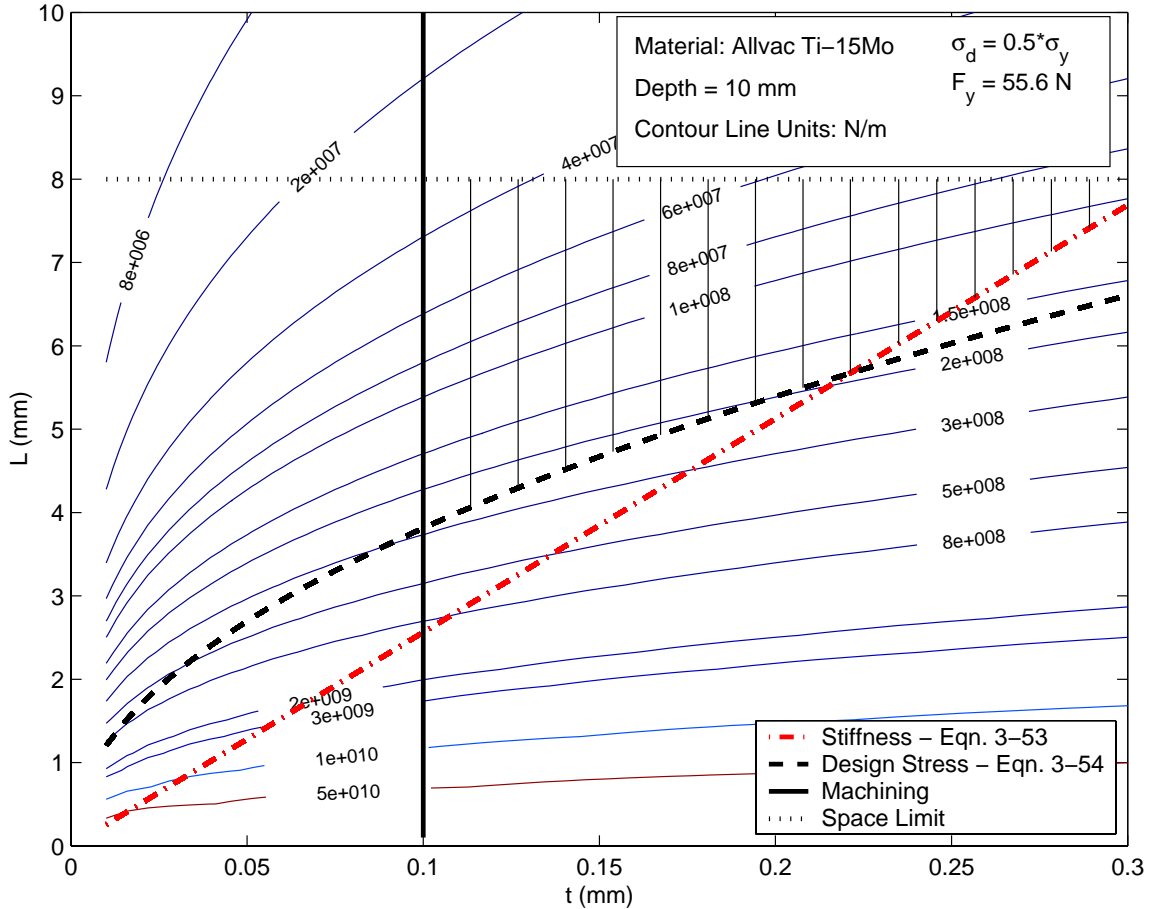


Figure 3-15. Design space for the selection of the beam dimensions used in the parallel axis flexure struts for PPII

In order to prevent the yielding of flexure elements from exceeding the travel limitations, it is good practice to include a mechanical stop in the design. In the case of the translation stage shown in Figure 3-13 and Figure 3-14, this can be accomplished by setting the gap distance between the two flexural elements to the desired travel range, as shown in Equation (3-55).

$$\delta_{y\ design} = s - 2t \tag{3-55}$$

Table 3-4 shows the selected dimensions and calculated parameters for the flexure elements of the PPII.

Table 3-4. Selected flexural element parameters for PPII flexure struts

Parameter	Value
Depth, b (mm)	10
Thickness, t (mm)	0.2
Length, L (mm)	6
Stiffness, $k_{\delta_y F_y}$ (N/m)	57,778
Design travel, $\delta_{y \text{ design}}$ (mm)	0.4
Design stress, $\sigma_{y \text{ design}}$ (MPa)	260

3.4 Multilayer Piezoelectric Bender Actuators

The performance of piezoelectric actuators depends upon the stiffness of their mounting structures and boundary conditions imposed upon the moving end. For the selection of commercially available piezoelectric actuators, the equations presented in section 1.3 provide a simple way to ensure that a piezoelectric actuator is capable of achieving the desired displacement range or force for a given displacement. For the selection of commercial piezoelectric actuators for the first and second generation alignment assemblies, this method was used.

In section 1.3, the equation for quick estimation of the constrained displacement was given in Equation (1-6). A simple estimation for the piezoelectric displacement may be obtained by substituting in the glass stiffness, $k_{g\theta}$, for the spring stiffness opposing actuator motion, k_s . Equation (3-56) shows the maximum effective displacement, ΔL , for this simplification, where ΔL_o is the unconstrained displacement and k_{piezo} is the stiffness of the piezoelectric actuator.

$$\Delta L = \Delta L_o \left(\frac{k_{piezo}}{k_{piezo} + k_{g\theta}} \right) \quad (3-56)$$

The term k_{piezo} may be determined from the actuator specifications by Equation (3-57), where F_{max} is the maximum blocking force of the actuator when constrained to zero displacement with maximum voltage and ΔL_o is the unconstrained displacement for maximum voltage.

$$k_{piezo} = \frac{F_{max}}{\Delta L_o} \quad (3-57)$$

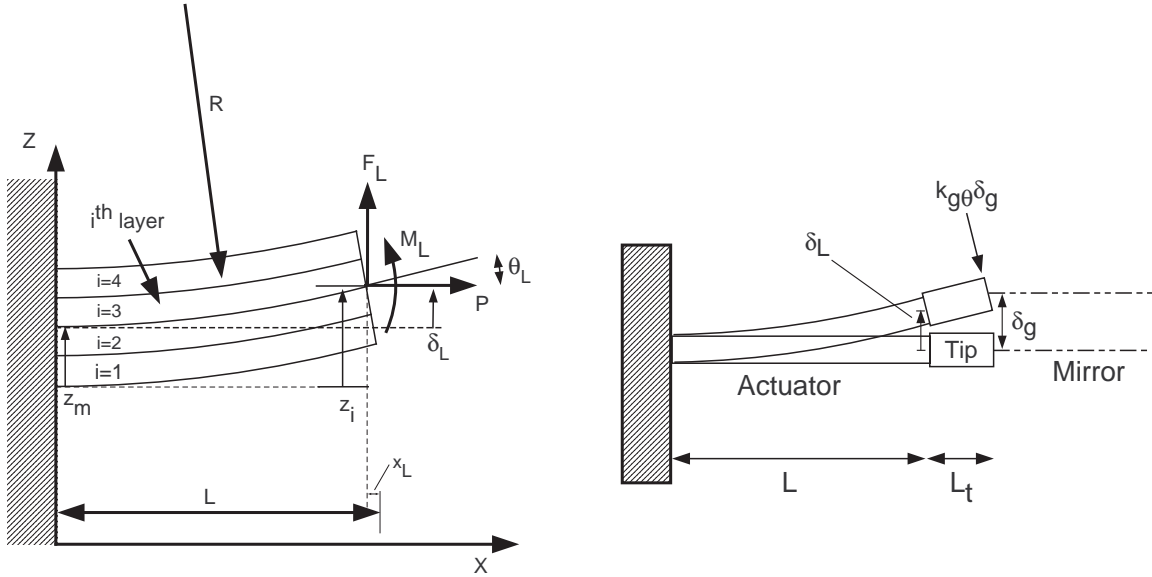
A further constraint on the piezoelectric actuators used in PPI and PPII is the available supply voltage. Although the actuator specifications are for +/- 100 V for a bipolar voltage system or 0-200 V when using differential voltage control, the supply voltage available is 150 V. This limitation results in a decrease of the achievable travel and force produced. As an initial estimate for the displacement for a given change in voltage, it was assumed that the relationship between voltage and displacement is linear. Table 3-5 shows the estimates for the displacement range of the actuators used in PPI and PPII. The actuator for PPII is listed as diced because the length of the stock actuator was modified by Noliac from 21 mm to 15 mm, which results in a decreased maximum displacement. This modification was necessary to meet the size requirements based on the available space between the primary and secondary housing assemblies. The estimates given for the actual actuator movement have not been tested.

Table 3-5. Piezoelectric actuator initial performance estimates

Parameter	PPI Values	PPII Values
Piezoelectric Actuator	Noliac CMB-P1	Noliac CMB-P1 (Diced)
Displacement Range, ΔL (μm), +/-	185	80
Voltage Range (Volts), +/-	100	100
Max Blocking Force (N)	1.2	1.8
k_{piezo} (N/m)	6,486.5	22,500
$k_{g\theta}$ for B3 Location (N/m)	110.05	110.05
Constrained Displacement Range, ΔL_o (μm), +/-	181.91	79.61
Constrained Displacement/Volt ($\mu\text{m}/\text{V}$)	1.8191	0.7961
Supply Voltage (Volts), +/-	75	75
Constrained and Voltage Limited Max Displacement (μm), +/-	136.44	59.71

For closed loop alignment schemes, it may be desirable to closely predict the actuator performance for quicker alignment algorithms in order to achieve the desired actuation point displacements. While the equations were not used for the scope of this research, they are presented for possible future use.

This section relates to the equations for multilayer piezoelectric bending actuators as presented by Weinberg [48] with the boundary conditions imposed by a reflector. The state of the piezoelectric actuator is described by the perpendicular movement (δ_L), angle (θ_L), and axial movement at the end (x_L) along with the charge on the actuator's electrodes (Q). The actuator is subject to an external force (F_L), moment (M_L), and axial load (P) applied at the end of the actuator along with the voltage (V) applied across the electrodes. Figure 3-16 shows the parameters associated with this analysis as well as the resistance to actuator movement from the glass stiffness.



(a) Multilayer Piezoelectric Bender Actuator Variables

(b) Bender Actuator with mirror and tip for a displacement of d_L

Figure 3-16. Parameters for multilayer piezoelectric actuators and the stiffness opposing actuator movement

The profile of an actuated piezoelectric bender may be described by a radius of curvature, R , as seen in Figure 3-16. The term C_M is the curvature of the bender actuator per unit moment and is the superposition of moment, force, and electric field effects. C_M is given by Equation (3-58), where E_i is the modulus of elasticity, I_i is the area moment of inertia, A_i is the cross-sectional area, and Z_i is the vertical position measured from a reference axis at the center of the beam before deflection to the neutral axis of the i^{th} layer after deflection [48].

$$C_M = \frac{1}{\sum_i E_i (I_i + A_i Z_i^2)} \quad (3-58)$$

The application of a voltage across the electrodes of the actuator creates a moment with the actuator. M_v is the moment per unit voltage across the electrodes, given by Equation (3-59) [48]. The term d_{31j} is the piezoelectric coupling coefficient and ε is

the permittivity, which are properties of the material. The neutral axis of the piezoelectric actuator is z_m . The subscript j refers to the layers in between the electrodes if there is more than one layer in between electrodes and the term t_j is the individual layer thickness.

$$M_v = \frac{\sum_j \frac{d_{31j} E_j A_j (z_m - z_j)}{\epsilon_j}}{\sum_j \frac{t_j}{\epsilon_j}} \quad (3-59)$$

The applied voltage across the electrodes creates an axial force within the actuator. F_v is the axial force per unit voltage, given by Equation (3-60) [48].

$$F_v = \frac{\sum_j \frac{d_{31j} E_j A_j}{\epsilon_j}}{\sum_j \frac{t_j}{\epsilon_j}} \quad (3-60)$$

The axial stiffness opposing an axial load may be determined using Equation (3-60), where L is the actuator length [48].

$$k_x = \frac{\sum_i E_i A_i}{L} \quad (3-61)$$

The state of the end of piezoelectric actuator can be determined using Equation (3-62) for the case where there is no axial tension in the actuator [48]. C is the capacitance of a single piezoelectric layer between electrodes.

$$\begin{bmatrix} \delta_L \\ \theta_L \\ x_L \\ Q \end{bmatrix} = \begin{bmatrix} \frac{C_M L^3}{3} & \frac{C_M L^2}{2} & 0 & \frac{C_M L M_v}{2} \\ \frac{C_M L^2}{2} & C_M L & 0 & C_M L M_v \\ 0 & 0 & \frac{1}{k_x} & \frac{F_v}{k_x} \\ \frac{C_M L M_v}{2} & C_M L M_v & \frac{F_v}{k_x} & C \end{bmatrix} \begin{bmatrix} F_L \\ M_L \\ P \\ V \end{bmatrix} \quad (3-62)$$

The motion of the glass using a piezoelectric actuator creates an end moment (M_L) due to the stiffness of the glass opposing motion and distance between the actuator end and point of actuation (L_t). The displacement of the glass at the point of actuation is given as δ_g and the stiffness of the glass opposing motion at an azimuth angle is given as $k_{g\theta}$

$$M_L = -k_{g\theta} \delta_g(L_t) \quad (3-63)$$

Given the geometry of Figure 3-16, substituting the applied moment M_L into the displacement portion of Equation (3-62), the end displacement of the actuator is given as Equation (3-64).

$$\delta_L = \left[\frac{2}{2 + k_{g\theta} C_M (L \cdot L_t^2 + L^2 \cdot L_t)} \right] \left[\frac{C_M L^3}{3} F_L + \frac{C_M L M_v}{2} V \right] \quad (3-64)$$

For small displacements with respect to the actuator length and the assumption that the stiffness of the tip is significantly greater than that of the glass, the displacement on the glass at the point of actuation may be estimated as a linear extension at the end of the actuator using Equation (3-65).

$$\delta_g \cong \delta_L + L_t \cos(\theta_L) \quad (3-65)$$

3.5 Actuation Stage Stiffness Modeling

In the design and use of a coarse positioning stage to move the actuators and mirror into alignment, it is important to understand the stiffness of the positioning system. The positioning system's stiffness will have an effect on the transmission of motion between the adjuster and the mirror during coarse alignment. In addition, the stiffness acting against a touch probe tip is important for understanding the movement of the mirror during placement using a coordinate measuring machine. For the movement of the mirror using the coarse adjustment of the screw adjuster, the stiffness of the flexure positioning system at a single strut location is shown by Figure 3-17.

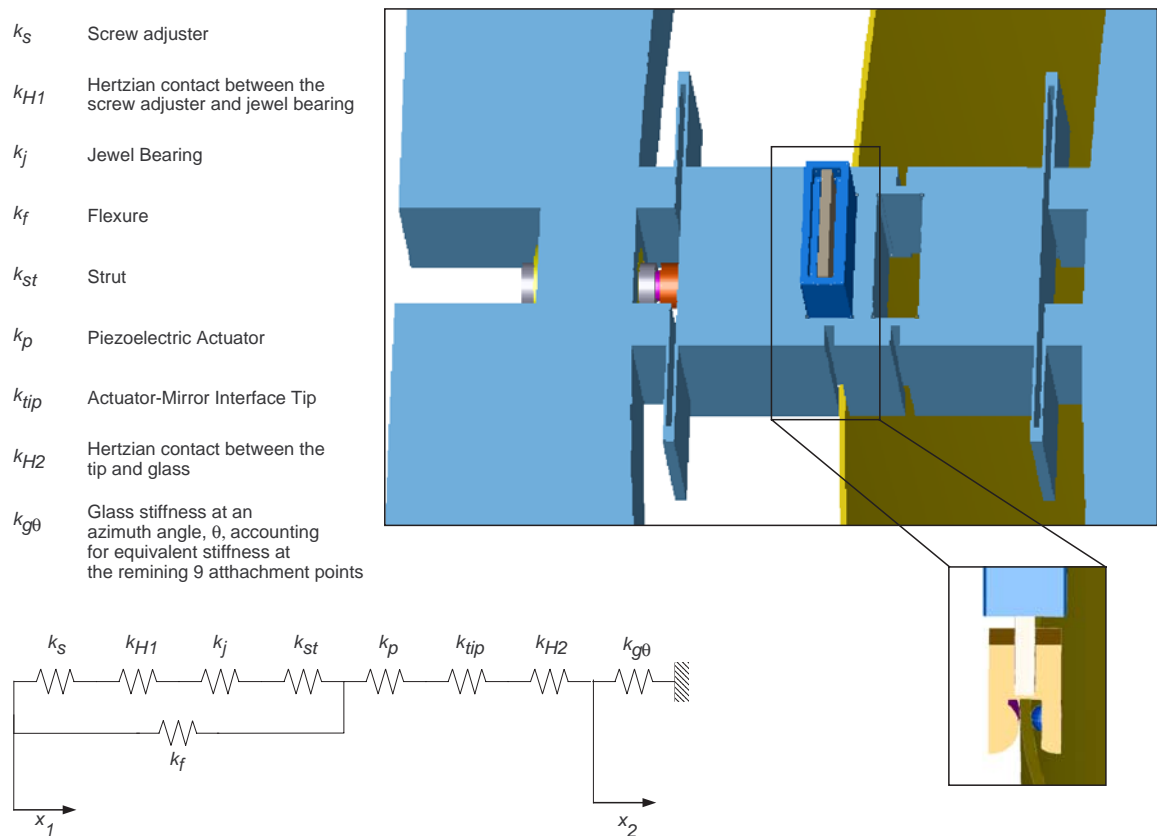


Figure 3-17. Equivalent stiffness model for screw adjuster movement of the mirror at a single strut location

The equivalent stiffness of a single strut location in the positioning system which does not include the glass stiffness is given by Equation (3-66).

$$\frac{1}{k_{eq1}} = \frac{1}{\frac{1}{k_s} + \frac{1}{k_{H1}} + \frac{1}{k_j} + \frac{1}{k_{st}} + k_f} + \frac{1}{k_p} + \frac{1}{k_{tip}} + \frac{1}{k_{H2}} \quad (3-66)$$

The transmission ratio between the adjuster screw translation and the mirror translation provides a model for how far the mirror will move for an adjuster movement. For a given force, F , the relation between the equivalent stiffness and displacement for the first actuation segment may be given by Equation (3-67).

$$F = k_{eq1}(x_1 - x_2) \quad (3-67)$$

The movement of the second actuation segment may be given by Equation (3-68).

$$F = k_{g\theta}(x_2) \quad (3-68)$$

The transmission ratio of x_2/x_1 may be determined by combining Equations (3-67) and (3-68), and is given as Equation (3-69).

$$\frac{x_2}{x_1} = \frac{k_{eq1}}{k_{eq1} + k_{g\theta}} \quad (3-69)$$

The second part of stiffness analysis involves the case when a touch probe is used to position the mirror during coordinate measuring machine (CMM) placement by touching the concave side of the mirror. Figure 3-18 shows the equivalent stiffness model for CMM placement.

- k_{eq1} Equivalent stiffness of a single strut location
- $k_{g\theta}$ Glass stiffness at an azimuth angle, θ , accounting for equivalent stiffness at the remaining 9 attachment points
- k_{H3} Hertzian contact between the CMM probe tip and glass

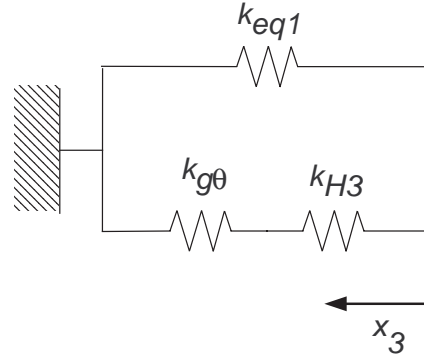


Figure 3-18. Equivalent stiffness model for CMM placement of the mirror

The equivalent stiffness, k_{eq} , acting against the probe tip placement, including the glass stiffness, is given by Equation (3-70).

$$k_{eq} = k_{eq1} + \frac{k_{g\theta} k_{H3}}{k_{g\theta} + k_{H3}} \quad (3-70)$$

Equation (3-71) gives the predicted distance, δ_{CMM} , that the mirror will move for a given probe tip force, F_{probe} .

$$\delta_{CMM} = \frac{F_{probe}}{k_{eq}} \quad (3-71)$$

In order to calculate the equivalent stiffness and model the system, the individual stiffness components must be determined. The equivalent stiffness of the screw adjuster, k_s , is comprised of three stiffness components acting in series and is given in Equation (3-72). The stiffness components are the threaded shaft (k_{sh}), engaged threads (k_{th}), and bushing threads (k_{bt}).

$$\frac{1}{k_s} = \frac{1}{k_{sh}} + \frac{1}{k_{th}} + \frac{1}{k_{bt}} \quad (3-72)$$

The equivalent stiffness of the threaded shaft, k_{sh} is given by Equation (3-73), where A_{sh} is the shaft effective area, which is defined by the minor diameter of the screw, d_m . The modulus of elasticity is given as E , and L_{sh} is the shaft length from the first engaged thread to the end of the screw in contact with the jewel bearing [49]. Given the modulus of elasticity of 18-8 stainless steel as 193 GPa, d_m of 2.7 mm, and L_{sh} of 3 mm, k_{sh} is $3.683 \cdot 10^8$ N/m.

$$k_{sh} = \frac{A_{sh}E}{L_{sh}} = \frac{\pi d_m^2 E}{4L_{sh}} \quad (3-73)$$

The stiffness of the engaged internal threads, k_{th} , is estimated by Equation (3-74), where d_n is the nominal screw diameter. The stiffness of the engaged bushing threads, k_{bt} , is estimated by Equation (3-75), where d_m is the minor diameter and d_n is the nominal diameter. The factors of 0.4 and 0.5 in the Equations (3-74) and (3-75), respectively, are based on empirical values for socket and hexagonal head bolts in steel joints [49]. Given the modulus of elasticity of 18-8 stainless steel as 193 GPa, d_m of 2.7 mm, and d_n of 3 mm, k_{th} is $1.137 \cdot 10^9$ N/m. Given the modulus of elasticity of brass as 105 GPa, k_{bt} is $4.008 \cdot 10^8$ N/m. The resulting stiffness of the screw adjuster is $1.6422 \cdot 10^8$ N/m.

$$k_{th} \cong \frac{0.25\pi d_n^2 E}{0.4d_n} \quad (3-74)$$

$$k_{bt} \cong \frac{0.25\pi d_m^2 E}{0.5d_n} \quad (3-75)$$

The stiffness of the jewel bearing, k_j , is given as Equation (3-76), where A_j is the effective area of the jewel, which is similar to the effective area of a bolted joint. The

region of material for a bolted joint which acts as a resistance to compression is equal to that of a 45 degree cone and is known as the cone of influence [42]. The effective area is defined by the radius of the Hertzian contact area between the screw adjuster and cup jewel, r_j . L_j is the length of the cup jewel from the screw adjuster interface to the strut interface. Since the Hertzian contact area will vary with the load, the stiffness of the jewel bearing will not remain constant. For a force of 0.1 N, the radius of the contact area is 12.467 μm . Given the modulus of elasticity of synthetic sapphire as 360 GPa, and L_j of 1 mm, k_j is $4.664 \cdot 10^6$ N/m.

$$k_j = \frac{A_j E}{L_j} = \frac{(\pi r_j^2 + r_j L_j) E}{L_j} \quad (3-76)$$

The stiffness of the strut is given as Equation (3-77), where w_{st} is the width, b_{st} is the depth, and L_{st} is the length of the strut. Given the modulus of elasticity of Ti-15Mo as 78 GPa, w_{st} of 13 mm, b_{st} of 10 mm, and L_{st} of 24.44 mm, k_{st} is $4.149 \cdot 10^8$ N/m.

$$k_{st} = \frac{A_{st} E}{L_{st}} = \frac{w_{st} b_{st} E}{L_{st}} \quad (3-77)$$

Assuming the piezoelectric actuator is not deflected or actuated initially, the stiffness of the actuator, k_p , can be estimated as a cantilevered beam, as given in Equation (3-78). The area moment of inertia is given as I_p , and L_p is the cantilevered length. The width of the actuator is w_p and the thickness is given as t_p . The modulus of elasticity of the soft-doped piezoelectric material, Pz21, from Noliac is 61 GPa [50]. Given w_p of 7.8 mm, t_p of 0.7 mm, and L_p of 15 mm, k_p is $1.2089 \cdot 10^4$ N/m.

$$k_p = \frac{3EI_p}{L_p} = \frac{E w_p t_p^3}{4L_p} \quad (3-78)$$

The stiffness of the tip, k_{tip} , can also be estimated as a cantilevered beam for the portion that is pushing against the glass, as given in Equation (3-79). The area moment of inertia is given as I_{tip} , and L_{tip} is the cantilevered length as measured from the end of the actuator to the point of contact with the mirror. The width of the tip is given as w_{tip} . The thickness of interest is for the half of the tip in contact, and is given as t_{tip} . Given the modulus of elasticity of Ti-15Mo as 78 GPa, w_{tip} of 3 mm, t_{tip} of 1 mm, and L_{tip} of 2 mm, k_{tip} is $7.3125 \cdot 10^6$ N/m.

$$k_{tip} = \frac{3EI_{tip}}{L_{tip}} = \frac{E w_{tip} t_{tip}^3}{4L_{tip}} \quad (3-79)$$

The stiffness of the flexure, k_f , was given in Equation (3-49), and was shown to be 57,778 N/m in Table 3-4. The values of $k_{g\theta}$ were given in Table 3-1. The Hertzian contact stiffness between the adjuster and jewel bearing, k_{H1} , may be calculated using Equation (3-44). As can be seen from the equations, the stiffness of the Hertzian contact varies with the deformation of the two bodies. As a result, stiffness will vary with the applied load. For the approximation of k_{H1} , a force of 0.1 N was used. The properties of the 18-8 stainless steel ($E=193$ GPa, $\nu=0.25$) and synthetic sapphire ($E=390$ GPa, $\nu=0.3$) are used. The diameter of the screw adjuster tip is 2 mm, while the interior diameter of the cup jewel is 2.8 mm. The resulting k_{H1} is $3.377 \cdot 10^6$ N/m.

The Hertzian contact stiffness between the tip and mirror, k_{H2} , may be calculated using Equation (3-36). For the approximation of k_{H2} , a force of 0.1 N was used. The

properties of the Ti-15Mo ($E=78$ GPa, $\nu=0.33$) and D-263 glass ($E=72.9$ GPa, $\nu=0.208$) are used. The diameter of the actuator tip is 2 mm, while the mirror diameter is approximately 494.3 mm. The resulting k_{H2} is 3.439×10^6 N/m.

The Hertzian contact stiffness of the probe tip contacting the mirror, k_{H3} , may be calculated using Equation (3-40) for a sphere within a cylindrical race. For the approximation of k_{H3} , a force of 0.078 N was used, which is the approximate CMM probe tip force. The properties of synthetic sapphire ($E=390$ GPa, $\nu=0.3$) and D-263 glass ($E=72.9$ GPa, $\nu=0.208$) are used. The diameter of the probe tip is 2 mm, while the mirror diameter is approximately 494.3 mm. The resulting k_{H3} is 4.9165×10^6 N/m.

Given the stiffness values of the components, the equivalent stiffness of an individual strut location positioning system, k_{eq} , may be calculated using Equation (3-66), and is 9,954.6 N/m. The predicted transmission ratio, x_2/x_1 , equivalent stiffness opposing CMM placement, k_{eq} , and the predicted deflection due to the probe tip contact force of 8 grams (0.078 N) may also be calculated using Equations (3-69) through (3-71). The stiffness modeling predictions for each of the actuation points is shown in Table 3-6.

Table 3-6. Stiffness modeling summary for PPII actuation points

Actuator Location	Screw Adjustment Transmission Ratio, x_2/x_1	Equivalent Stiffness Opposing CMM Placement, k_{eq} (N/m)	Deflection due to 8 gram Probe Tip Contact, δ_{CMM} (μm)
B1	0.9997	9958.0	7.8788
B2	0.9900	1005.6	7.8020
B3	0.9891	1006.5	7.7949
B4	0.9900	1005.6	7.8020
B5	0.9997	9958.0	7.8788
U1	0.9997	9957.0	7.8789
U2	0.9903	1005.2	7.8045
U3	0.9894	1006.1	7.7977
U4	0.9903	1005.2	7.8045
U5	0.9997	9957.0	7.8789

The stiffness modeling results show that the translation of the screw adjuster is transferred to movement in the glass very well due to the low glass stiffness in comparison to the positioning system stiffness. The other significance of the stiffness modeling results is that they show a significant mirror deflection due to the CMM probe tip force. The mirror deflection is primarily due to the compliance of the positioning system, which is largely affected by the component with the least stiffness, the piezoelectric actuators. The other implication of the dominating low stiffness of the piezoelectric actuators is that although the stiffness of the Hertzian contact and cup jewel varies with the load, this will have minimal impact on the equivalent stiffness of the system. The possibility of mirror deflection during CMM placement means that the CMM placement will have additional error on top of the machine error. For this reason, the use of collimated beam alignment is used to minimize the errors introduced during the CMM placement process. Both of these alignment methods will be explained in Chapter 4.

It should be noted that the stiffness models have not been experimentally validated for the as-built assemblies. Additional experimentation and testing of the assembled components for use in designing future assemblies will be beneficial. For the current research scope, the emphasis was placed on the achievable alignment performance. This chapter has discussed the important aspects in the assembly design analysis. The design of the mirror interface and positioning system will lead to the testing of alignment capability of the assembly.

CHAPTER 4

OPTICAL ALIGNMENT AND TESTING

Several alignment procedures and optical testing methods are utilized in order to align and analyze the segmented optics. Before optical testing methods can be used, mechanical assembly provides the alignment starting point, including the physical positioning of the mirror using a coordinate measuring machine. The physical positioning provides the starting point for optical alignment where precise positioning and alignment of the optic can be achieved. Optical testing methods are used to align the optics for the preparation of x-ray testing of the optics [51]. This chapter details the alignment methods and testing results for the use of piezoelectric actuators using physical and optical alignment.

4.1 Coordinate Measuring Machine (CMM) Alignment

The first step in the alignment of the mirror segment is the appropriate radial placement of the mirror using a coordinate measuring machine (CMM). The placement of the mirrors is based off of the optical axis. The location of the optical axis with respect to the as-built housings has previously been established, and is referenced by the location of tooling balls on the housing. Figure 4-1 shows the PPI assembly during CMM alignment.

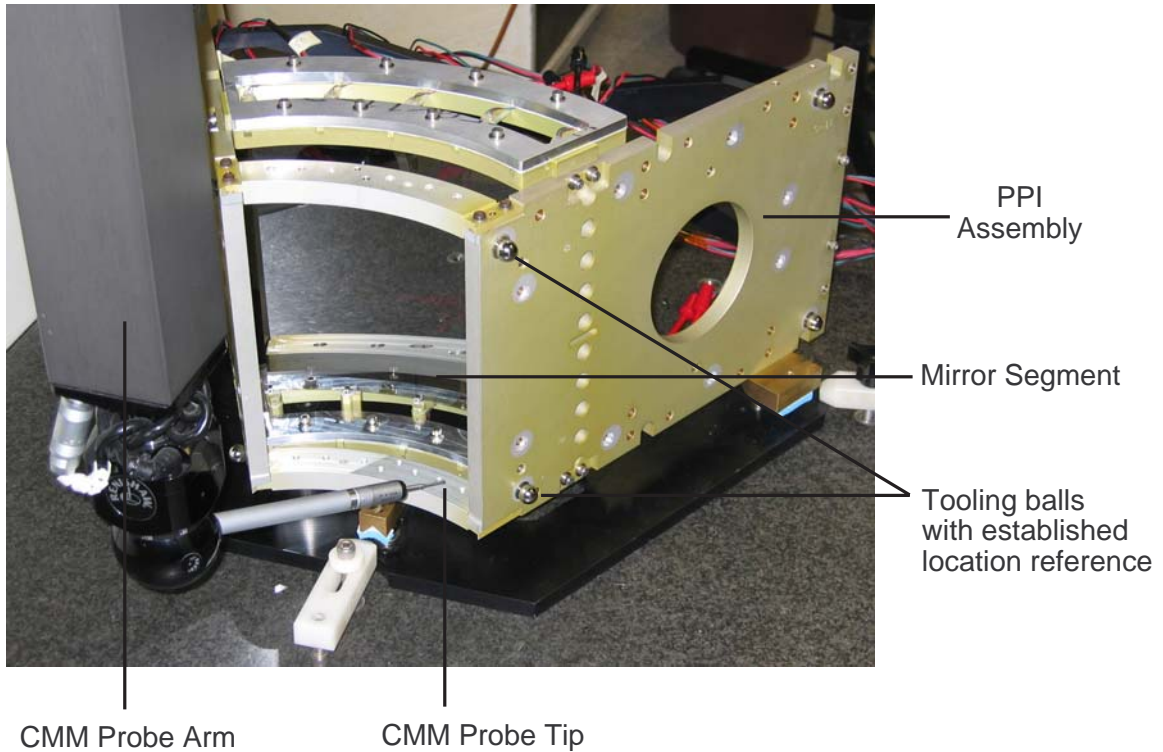


Figure 4-1. PPI assembly during CMM placement

The CMM is used to radially position the mirror at each of the actuation points. It is assumed that the axial distance for the bottom edge of the secondary mirror corresponds with the designed axial distance to the bottom of the secondary mirror. This assumption introduces a possible average radius error that is traced back to when the substrate is taken off of the forming mandrel and cut to size. Currently, there is no way of verifying exactly where the mirror segment was cut in relation to the mandrel. Since a CMM contact probe is not capable of sensing at exactly the top and bottom of a reflector, the axial distance at which the probe touches the mirror is entered into Equation (1-2) to determine the correct radial distance placement. Table 4-1 gives the axial distance entered into Equation (1-2) and the resulting nominal radial distance used to position the 494 series secondary mirror for PPI.

Table 4-1. Radial and axial distance values for CMM placement of the PPI 494 secondary mirror segment

Location	Axial distance from Primary-Secondary Intersection, z_2 , (mm)	Radial distance, h_2 , (mm)
Bottom Actuators (B1-B5)	221.5	242.258
Top Actuators (U1-U5)	26.5	246.565

The resolution of the CMM used is +/- 2.5 μm . However, as discussed in section 3.5, the probe tip force required to register a reading introduces additional significant error into the actual placement of the mirror of nearly 8 μm for the given assembly. In addition, the speed at which the probe tip comes into contact with the mirror may cause errors in the actual accuracy of the CMM placement. The use of CMM alignment which requires less force to obtain a reading or non-contact CMM alignment would significantly improve the initial placement. Due to the significant range of errors during CMM placement, it is beneficial to use collimated beam testing to minimize the errors introduced during CMM alignment.

4.2 Collimated Beam Testing

The purpose of collimated beam testing for the Constellation-X segmented mirrors is to allow visualization of the entire mirror surface curvature and begin initial positioning using the piezoelectric actuators. Collimated beam testing is an intermediate step between the coarse positioning in CMM alignment and precise alignment using the Centroid Detector Assembly (CDA) as described in section 4.3 and axial interferometry as described in section 4.4. The precise alignment methods using the CDA and axial interferometry look only at small apertures at several azimuth locations on the mirror. The collimated beam testing floods the entire surface of the mirror with a white light

source. The light is collected and focused, giving a visual representation of the approximate curvature of the mirror.

The collimated beam testing is advantageous in that it allows for the correction of any inadvertent misalignment during the CMM process or movement of the entire housing between metrology for CMM alignment and optical testing. In addition, the white light testing decreased the setup time for CDA alignment by improving the initial focus.

4.2.1 Collimated Beam Test Setup

The testing setup was previously used in the development of the Astro-E2 x-ray observatory. The setup includes a Xenon white light source pointed onto an off-axis parabolic mirror which collimates the light source in the vertical direction. The optical segment is placed below the vertical collimated beam, allowing light to be reflected off of the surface. The reflected light is directed horizontally off of a forty-five degree fold flat. The focused light can be observed by placing an opaque backdrop or CCD camera at the focal length of the mirror segment. In order to distinguish the movements at different points on the mirror, an opaque backdrop was also placed one meter in front of the focal point. At a distance in front of the focal point, the reflected light has not converged. As a result, the reflected light which is not blocked by the five actuation points is distinguishable as four separate sections. A schematic of the testing setup is shown in Figure 4-2. Figure 4-3 shows the piezo prototype during collimated beam testing.

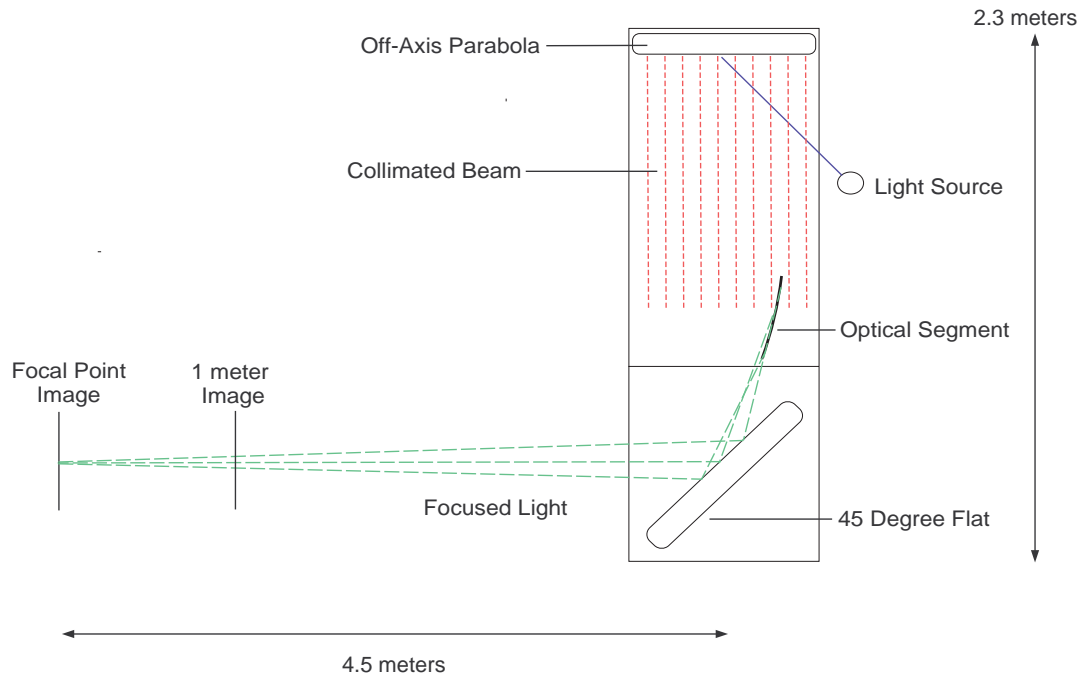


Figure 4-2. Collimated beam test setup

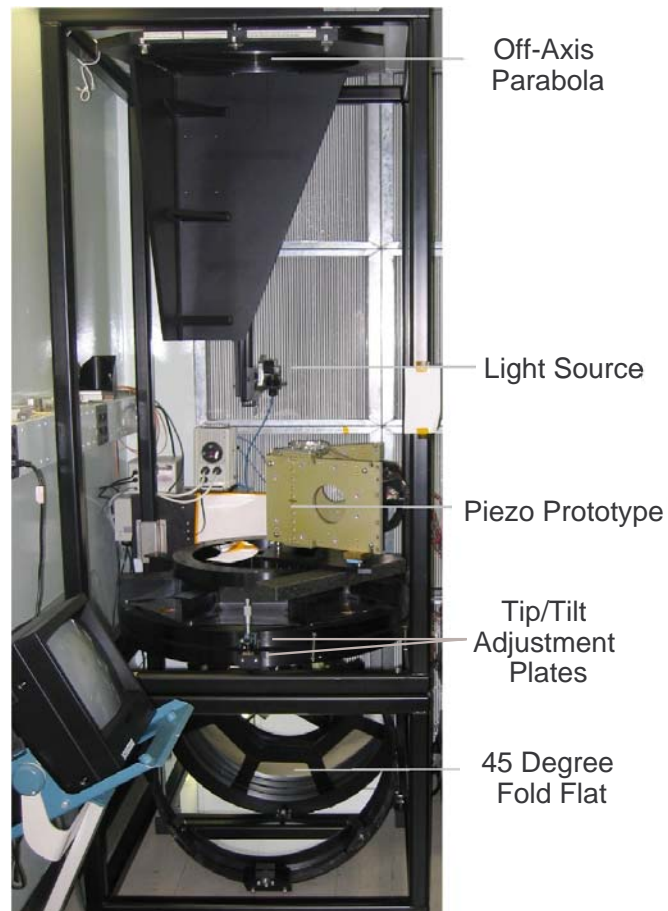


Figure 4-3. PPI in collimated beam testing

The entire OAP housing rests on a three point kinematic mounting plate with three vee grooves. This plate rests on two adjustable plates which rotate about the center of the optical beam. These two adjustable plates allow for the adjustment of the tangential tilt and radial tilt of the optic as discussed in section 1.4. Though the focal length of the telescope with both a primary and secondary mirror is 8400 mm as listed in Table 1-1, the focal length of an individual mirror differs and is necessary for the initial alignment and correction of one secondary mirror before adding the primary segment. The approximation for the focal length of a single mirror segment was presented in section 1.2.

In order to compare the cone angle approximation to the actual design focal length, ray-trace analysis is used. Due to the curvature and geometry of a secondary mirror, ray-trace analysis is capable of determining the accurate focal length [52]. A comparison of the calculated focal length of the secondary optic using the cone angle approximation and using ray-trace analysis for the mirror prescription is shown in Table 4-2. The reason for the difference between the cone angle approximation and the ray-trace analysis is due to the second-order axial figure. In addition, the difference between the cone angle approximation and ray-trace analysis increases as the series designation (and mirror radius) increases because the second order axial figure curvature peak-to-valley (P-V) value increases as the mirror segment series increases.

Table 4-2. Focal length comparison for cone angle approximation and ray-trace analysis

Series Designation	485	489	494
Cone angle approximation, mm	5529.23	5529.20	5529.16
Ray-trace analysis, mm [52]	5529.57	5529.96	5530.35

4.2.2 Collimated Beam Test Results

The collimated beam testing is primarily a rough visual alignment at this stage in its development. However, the curvature of the projected light can be predicted and used as a guide for the alignment. The projected light at a position in front of the focal length is a part of a circular section. Using parameters of the optic found in Equation (1-3), the radius of a circle that the reflected light should follow at a point in front of the focal length is found using Equation (4-1), where r is the radius in meters and d is the distance in front of the focal point in meters, and ϕ is the cone angle of the optic. [53].

$$r = d \tan(2\phi) \quad (4-1)$$

The initial focus of the piezo prototype in the collimated beam setup showed that the initial profile of the mirror exhibited several irregularities from a circular section. This occurrence was expected and was the reasoning for the collimated beam testing. Each of the piezoelectric actuators is turned on to their center positions in the sequence shown in Figure 4-4. The reasoning for this sequence is that the middle portion of the mirror is the stiffest region [60]. In addition, the actuators at the center azimuth of the mirror primarily affect the cone angle of the entire mirror segment. During the adjustments of the mirror, it is beneficial to manipulate and set the center actuators of the

mirror initially and then move to the other actuators, as the mirror edges are the most compliant.

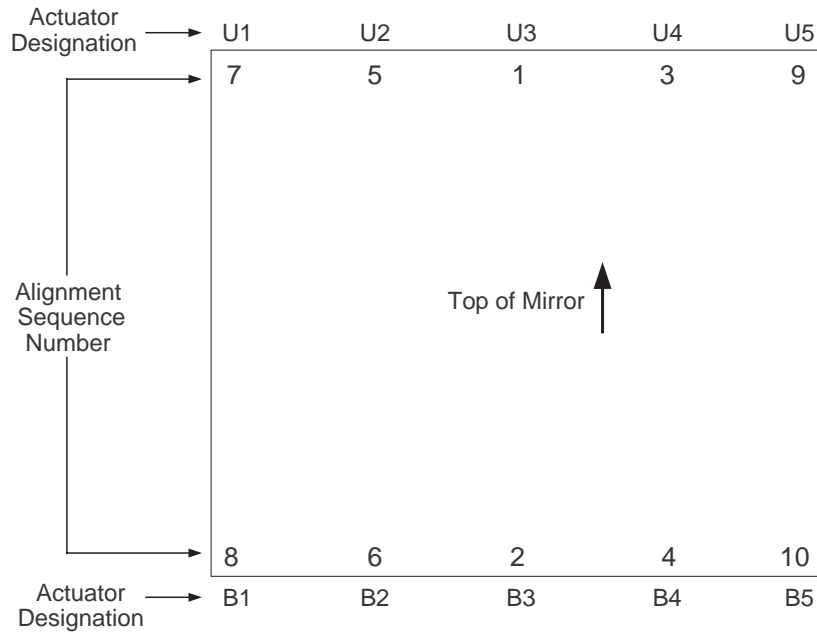


Figure 4-4. Mirror initialization and alignment sequence

After observation of the initial mirror profile, it is important to start with the center actuators and match the center profile of the mirror with the projected curvature line. After this has been accomplished, the other radial positions can be manipulated with the piezoelectric actuators to match the projected curvature. Figure 4-5 shows the profile projections at one meter in front of the focal point of the collimated beam testing at several stages during the alignment. A digital camera is used to capture the projections shown on the opaque backdrop. There appears to be two separate sections of light, which is due to the diffraction pattern of the light reflected off of the mirror segment for the given focal length and mirror orientation [54].

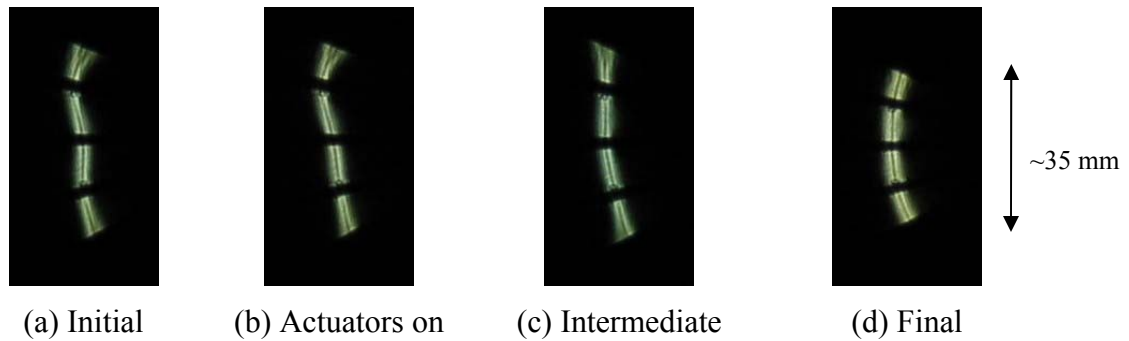


Figure 4-5. Collimated beam projections during alignment at one meter in front of the focal point

Figure 4-5 (a) shows the initial profile of the mirror segment, which shows a deviation from the expected profile of a circular section. Figure 4-5 (b) shows the profile after the piezoelectric actuators have been initialized. Figure 4-5 (c) shows an intermediate step in the alignment as the shape is beginning to resemble a curve. Figure 4-5 (d) shows the final alignment during the collimated beam testing. In order to verify that the image shown in Figure 4-5 (d) is the correct alignment, a circle of the correct radius given in Equation (4-1) is placed on backdrop used to capture the images. This backdrop reference is also used to determine the appropriate radial adjustments to correct the curvature. Using the current setup of visual alignment, there is no ability for quantification of the alignment until the next step of Centroid Detector Assembly (CDA) alignment, which will be discussed in section 4.3. The further development of the collimated beam alignment for Constellation-X mirrors may incorporate the use of CCD cameras, which could be used in conjunction with real-time image analysis for improved feedback and quantification of the results during this alignment step.

The collimated beam alignment is also recorded throughout the alignment stages at the focal point. In order to see the points converge, the cone angle of the optic can be

controlled through rigid body adjustment of the mirror housing, which effectively adjusts the focal length of the optic in accordance with the derivation of Equation (1-5). By adjusting the cone angle to a shallow orientation, the focal length is increased. The resulting image at the nominal focal length of the mirror shows a defocused image of the reflected light from the mirror converging. This defocused image, captured with a CCD camera, can be observed in Figure 4-6 (a) and (b). These images which correspond to the pictures taken at one meter in front of the focal point as shown in Figure 4-5 (a) and (d), respectively. The focused images are shown in Figure 4-6 (c) and (d). These images which correspond to the pictures taken at one meter in front of the focal point as shown in Figure 4-5 (a) and (d), respectively. As mentioned previously, the development of collimated light testing could utilize CCD camera analysis for the further refinement of this alignment step.

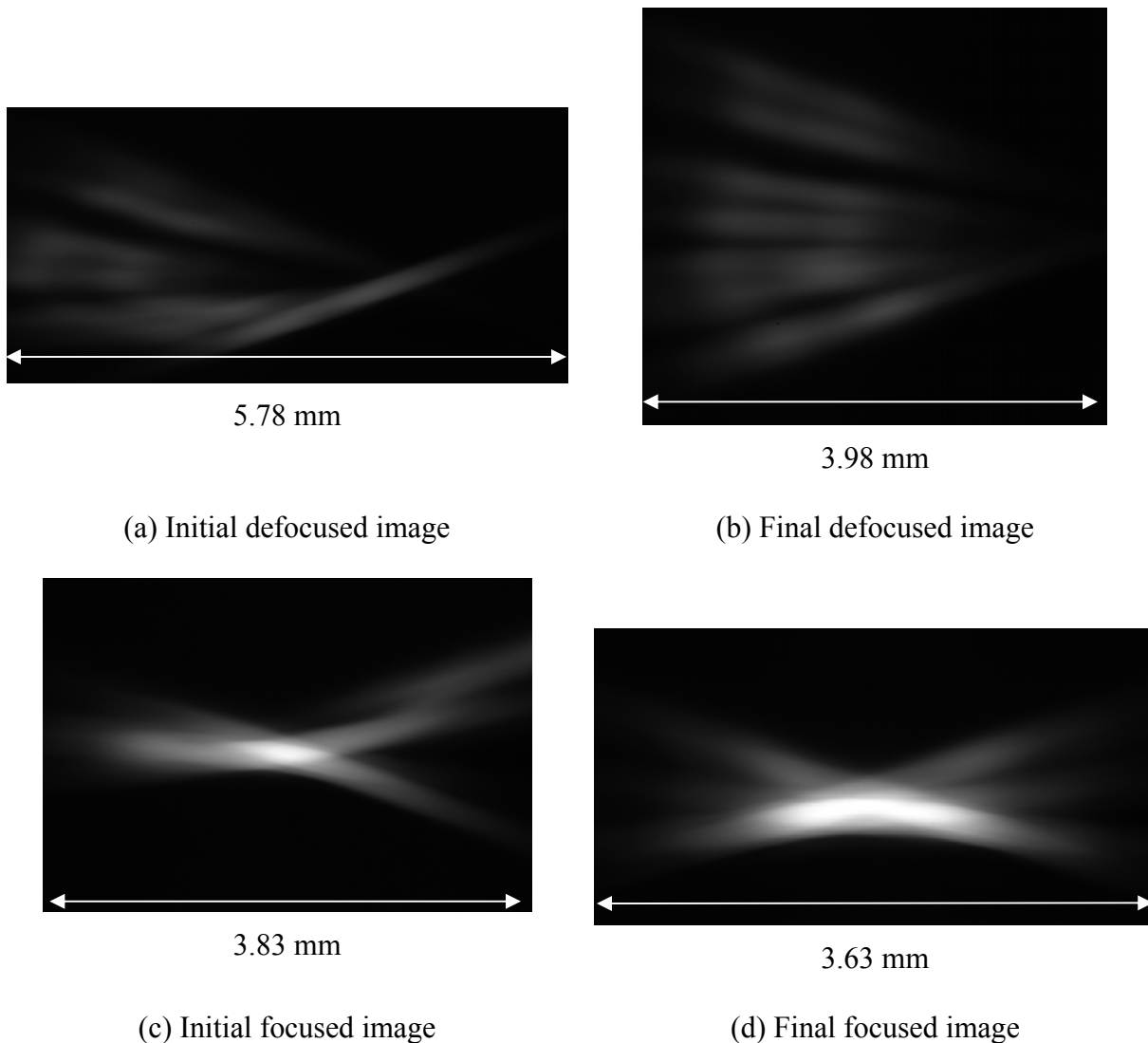


Figure 4-6. Focused and unfocused collimated beam projections at the focal point

4.3 Centroid Detector Assembly (CDA) Alignment

The next step in the optical alignment of the mirror segment is through the use of the Centroid Detector Assembly (CDA), which was initially used for the alignment of the Chandra X-Ray observatory [55]. The CDA is based off of a modified Hartmann approach, which tests small subsections of the mirror aperture, and then integrates over the entire surface of the mirror. In general, the CDA sends a beam externally that is reflected off of the mirror surface, off of a return optical flat, and then returned to the

CDA photodiode detector. The CDA can then determine the wave front error of the mirror alignment by comparing the lateral position error from the return beam. Since the CDA laser beam covers nearly the entire axial length of the mirror, the CDA effectively returns information on how to align the first order axial figure, or cone angle, of the mirror by adjusting the actuators on the top and bottom of the mirror. Additional information on the design, configuration, and specifications of the CDA can be found in [55].

4.3.1 Mirror Segment Actuation

The rigid body manipulation of the optic during CDA alignment is accomplished through adjustment of the tip and tilt of the mirror housing at the kinematic mount interface points. The non-rigid body manipulation of the mirror segment is accomplished using the piezoelectric actuators. The first step will be to define the coordinate system for the mirror segments for actuator motions. The z-axis follows the direction of the optical axis. The x-axis points from the optical axis to the mirror surface. The y-direction is therefore pointing to the left when looking at the front surface of the mirror. The radial direction is positive as the location moves away from the optical axis. The azimuth locations of the actuators correspond to the values shown in Figure 2-5. Figure 4-7 shows this coordinate system.

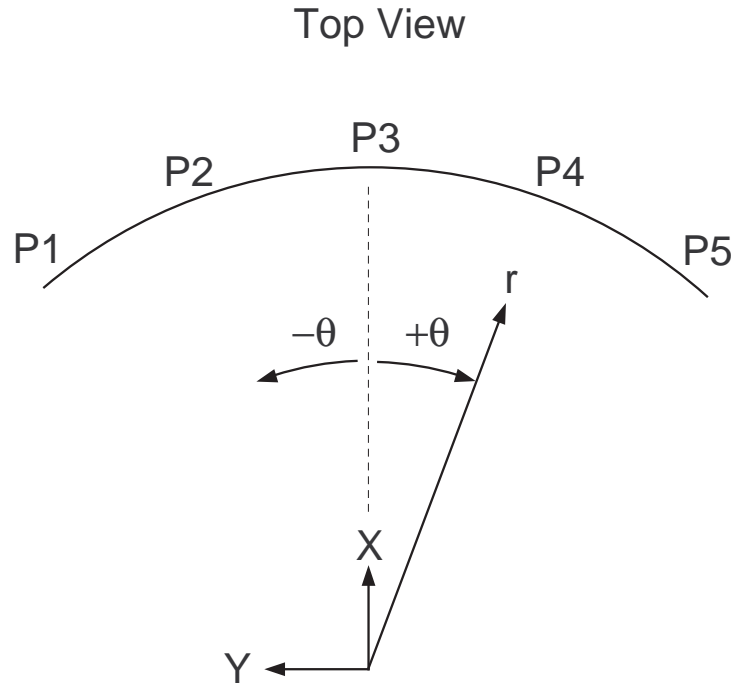


Figure 4-7. Mirror segment coordinate system for actuator movements

It is assumed that the actuator movements are made in the radial direction. For a linear movement by a single actuator, the movement of the mirror at the point of actuation is given by Equations (4-2)-(4-4), where c is the actuator movement in the radial direction, L is the axial length of the mirror, and θ is the azimuth location of the actuator.

$$x = c \cdot \cos(\theta) \quad (4-2)$$

$$y = -c \cdot \sin(\theta) \quad (4-3)$$

$$z = -\sqrt{L^2 - x^2 - y^2} \quad (4-4)$$

The change in the z direction of a point on the mirror is very small in comparison to the actuator movement. For a $25 \mu\text{m}$ actuator motion, the change in the z -direction for a point on a mirror initially vertical would only be approximately 1.5 nanometers (nm). Due to the initial cone angle of the mirrors, a positive (outward) radial movement results

in a negative change in the z location of the point of actuation, while a negative (inward) radial movement results in a positive change.

The purpose of the actuators during CDA alignment is to change the cone angle of the optic at the azimuth location of the actuator. The cone angle at a given azimuth is referred to as the local cone angle. The local cone angle can be changed by moving one actuator to rotate about the top or bottom edge of the mirror or can be changed by moving a pair of actuators at an azimuth location in opposite directions to rotate about the center of the mirror. The movement of actuators in opposite radial directions is referred to as differential-mode adjustment, which is shown in Figure 4-8.

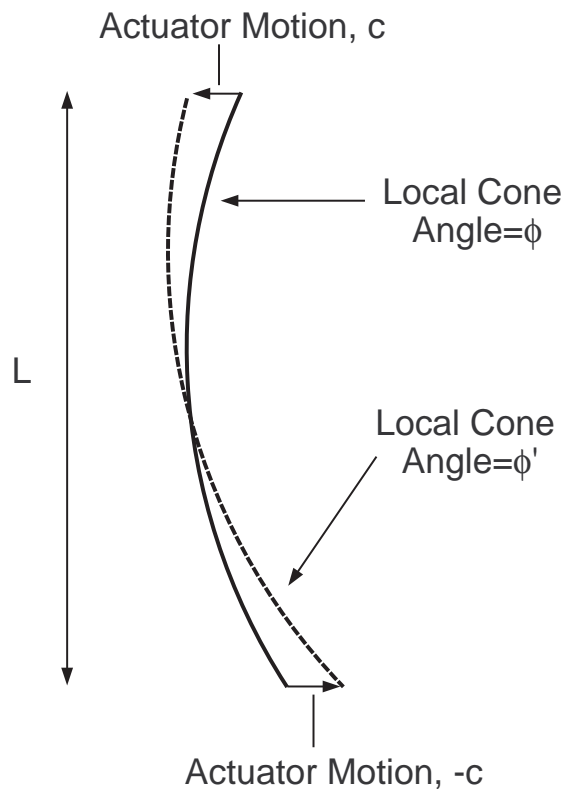


Figure 4-8. Differential mode actuator movement for local cone angle change

The change in the local cone angle, $\gamma = \phi' - \phi$, for a differential mode adjustment may be determined using Equation (4-5). This local cone angle change assumes that the

mirror rotates about a point midway between the actuators and that the small change in the z-direction is small in comparison to the movement. For the movement of only one actuator, the $2c$ term may be replaced by c assuming that the mirror segment rotates about the opposite actuator.

$$\gamma = \phi' - \phi = \tan^{-1}\left(\tan \phi + \frac{2c}{L}\right) - \phi \quad (4-5)$$

$$\gamma \approx \frac{2c}{L} - \phi$$

Although the z direction effects in determining the cone angle were neglected due to their magnitude, it is important to keep in mind that the tip interface should not constrain the mirror in the z direction. This is to prevent the actuator from imparting undesired axial stresses or third order deformations along the axial profile of the mirror, which will be relevant for the axial interferometry testing discussed.

4.3.2 CDA Test Setup

The main components utilized for CDA testing include the CDA, metrology tower, mirror segments, and fold flats. The fold flats are used to maintain all components on the available space on an optical vibration isolation table and direct the CDA beam from a horizontal orientation to the vertical orientation needed for grazing incidence off of the mirror segment surface. The metrology tower is used to mount the mirror assembly. Integrated into the metrology tower are three spheres for the three-point kinematic mount interface with the mirror housings. The two rear kinematic mounts are adjustable with the use of a micrometer and are used for tip and tilt adjustments of the mirror housing as previously mentioned.

The metrology tower includes an aperture mask, which reduces the divergence of the CDA beam by masking off azimuth areas along the mirror segment which are not utilized. In order to return the beam to the CDA detector assembly, a fold flat is used to return the CDA beam back off of the mirror surface. This denotes that the alignment system is a double-pass configuration. Figure 4-9 shows a schematic of the beam path layout with an inset of the schematic of beam path within the metrology tower. The schematic gives a representation of different azimuths along the mirror segment that the CDA may direct a beam at. Figure 4-10 shows the PPI within the metrology tower.

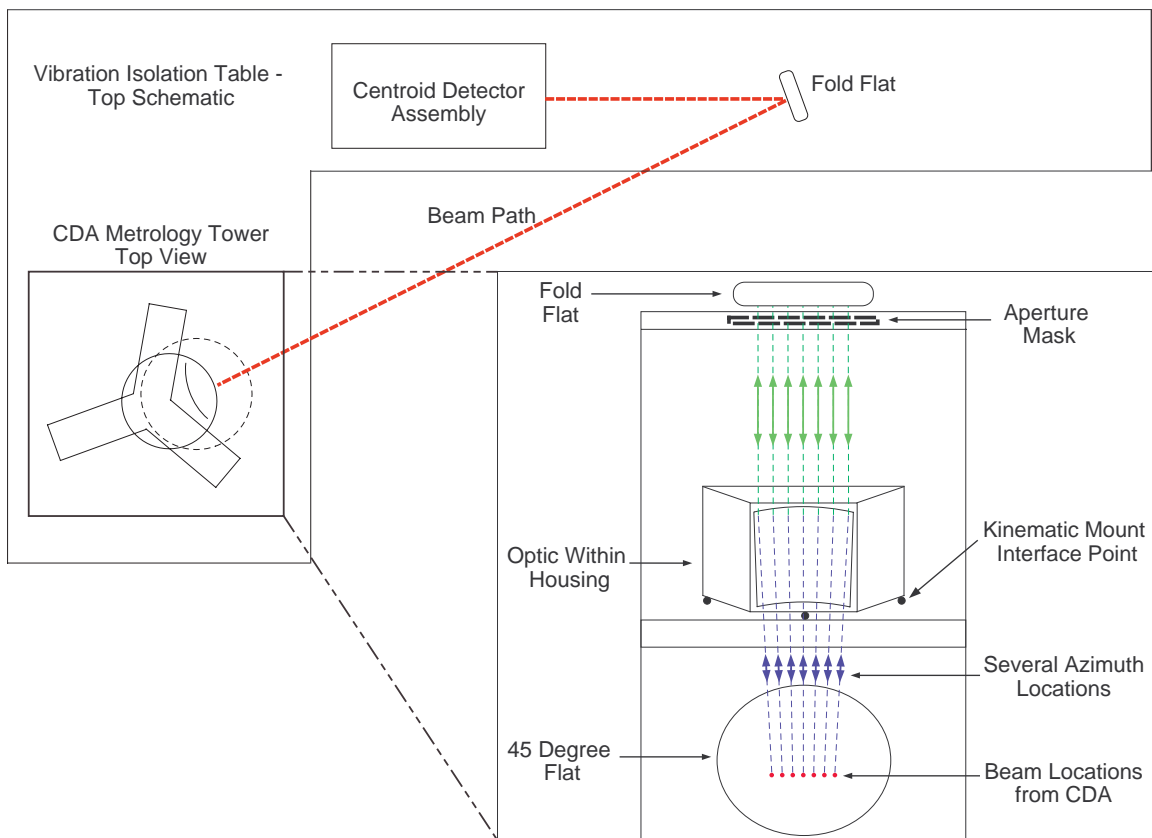


Figure 4-9. Schematic of bench layout for CDA testing with inset of the metrology tower layout demonstrating various azimuth beam locations across an optic surface

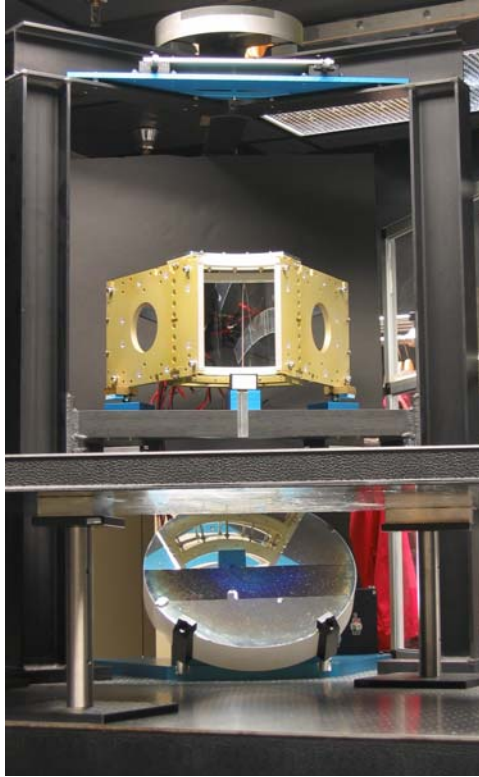


Figure 4-10. PPI in the CDA metrology tower

4.3.3 CDA Alignment Test Results

The CDA detector assembly is capable of returning alignment information for rigid body motions. For comparisons of the alignment done with the CDA using non-rigid-body actuations after the rigid body motions have been set, the alignment parameter that will be used is the root-mean-square (RMS) image radius. After the centroid of all of the return spots is determined, the radial locations, r , of each of the n return beams are determined. Equation (4-6) is used to determine the RMS image radius.

$$r_{RMS} = \sqrt{\frac{\sum_{i=1}^n r_i^2}{n}} \quad (4-6)$$

The comparison of CDA alignment results shows the location of the return beams for a given step in alignment. The numbers correspond to the aperture mask location.

The aperture mask used covers fourteen locations along the azimuth of the mirror segment. The aperture mask locations not shown in comparisons are locations at which struts blocked the passing of the CDA beam. It should be noted that the coordinate system of the CDA software differs from the coordinate system used to define the mirror segments and actuator movements. The y and z axes on the CDA correspond with the negative x and negative y mirror axes, respectively. Local cone angle changes from differential actuators movements are used to converge the spots during each step. A single step focuses on one azimuth location and uses actuators near that azimuth to make adjustments.

The CDA alignment builds off of the intermediate step of collimated beam testing. Figure 4-11 shows several steps in the CDA alignment sequence of a 494 secondary mirror.

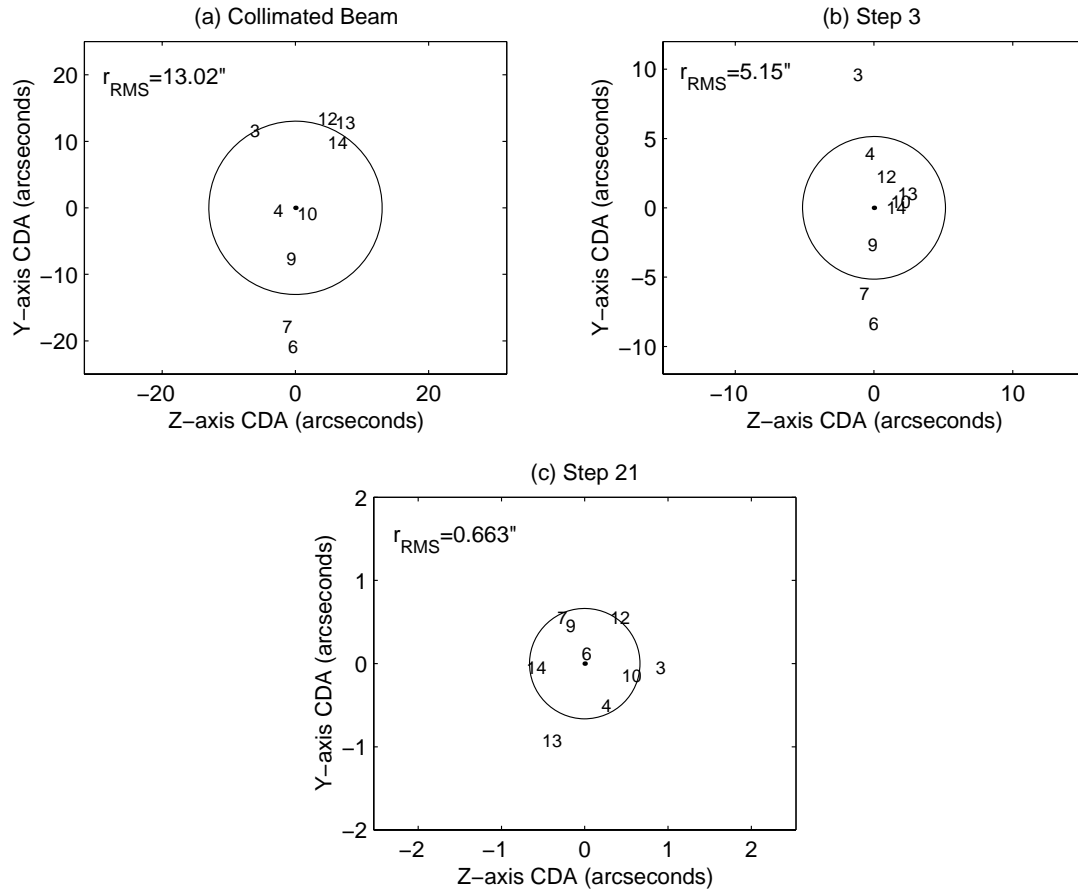


Figure 4-11. Alignment trial 1 CDA spot locations for several alignment steps

The alignment of the optic was repeated by turning off all piezoelectric actuators and starting over from the alignment achieved during collimated beam testing. Figure 4-12 shows several alignment steps in the repeatability testing of the alignment.

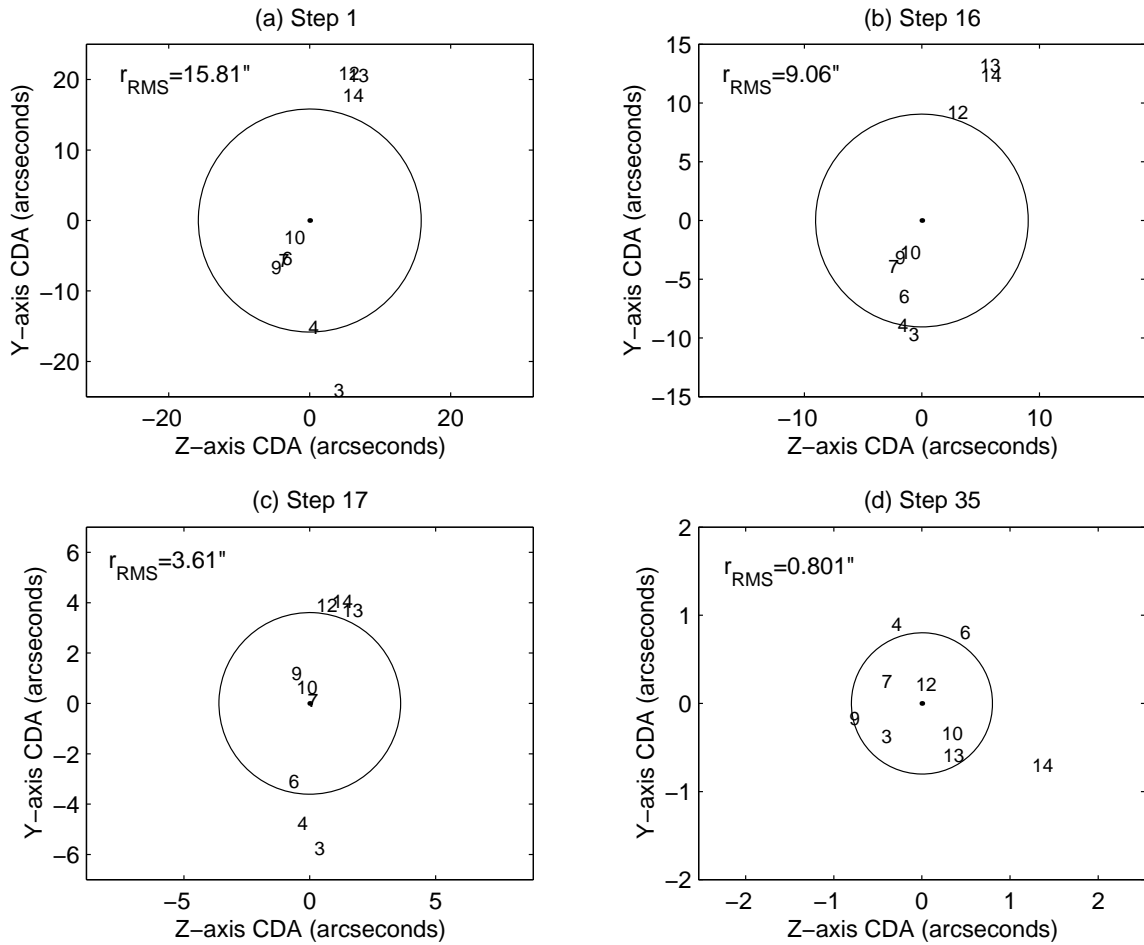


Figure 4-12. Alignment trial 2 CDA spot locations for several alignment steps

Initial differences in the position of the CDA spots are due to the hysteresis of the actuators from cycling them from zero voltage and back to the collimated beam positions. The main source of the difference between the final RMS spot return radiuses is attributed to the dynamic error of the return spots during data acquisition, which will be discussed. Table 4-3 summarizes the RMS radius of the CDA spot return from the mirror segment after collimated beam testing and CDA alignment. The significance of the CDA alignment results is that after rigid body alignment motions have been achieved, non-rigid body alignment using piezoelectric actuators can significantly improve CDA alignment results.

Table 4-3. Comparison of r_{RMS} for CDA spot returns

Alignment Trial	r_{RMS} (arcseconds) – CDA Spot Return	
	Collimated Beam Testing	Post-CDA Alignment
1	13.02	0.663
2	15.81	0.801

There are number of sources of error during the CDA alignment which must be characterized for the actual mirror performance. The CDA alignment errors can be broken down into several sources within two categories of static errors and random dynamic errors [56]. These errors result in a discrepancy between the CDA alignment and actual performance of an x-ray test. The static errors are attributed to the CDA internal components, metrology setup, and pointing performance of the CDA beam. The static errors for the CDA internal components are due to the maximum error from an internal beam splitter, which may be eliminated in the future by using a reference beam internal to the CDA [56]. The static errors attributed to the metrology setup are a result of the quality and number of fold flats used in the metrology setup, which have a surface figure error which deviates from a perfect flat. The pointing performance error is if the CDA beam is not concentric with the telescope focus.

The dynamic errors are seen in the movement of CDA point returns during data acquisition. The dynamic errors result from the internal components of the CDA (beam stability), environmental vibrations, and air currents. These errors ultimately limit the resolution achieved with the actuator system as well as the alignment that can be achieved using both a closed or open-loop configuration. The dynamic error motions of the CDA points were observed during testing of the secondary optic in PPI. Table 4-4 gives the observed random error motion in RMS diameter of the spot returns as well as

the diameter encompassing plus or minus three standard deviations ($\pm 3\sigma$) of the mean error motion, which encompasses 99.73% of the possible point locations for a normal distribution [39].

Table 4-4. Observed dynamic error on CDA points

Point	3	4	6	7	9	10	12	13	14
d_{RMS} (arcseconds)	0.414	0.438	0.559	0.476	0.506	0.466	0.523	0.462	0.462
$d_{\pm 3\sigma}$ (arcseconds)	0.610	0.648	0.831	0.730	0.759	0.687	0.781	0.756	0.733

The range given by the $\pm 3\sigma$ value of error motion should be considered when the precise alignment as shown in the last alignments of Figure 4-11 and Figure 4-12. At this point in alignment, the possible spot positions due to random error motion are nearly as large as the focus of all aperture points, making further alignment difficult.

4.4 Axial Interferometry

The purpose of axial interferometry is to investigate the effects of actuators on the second-order axial figure, or axial sag, of the mirror segments, as shown in Figure 1-2. A discussion of various methods of optical metrology for the segmented optics is given by Content, et al. [57].

4.4.1 Axial Interferometry Test Setup

The axial interferometry performed uses collimated beam interferometry which measures the profile over a narrow azimuthal position, and therefore only allows metrology on small subsections of the mirror at a time. The narrow azimuthal measurement is due to the part curvature, which results in a return beam only from a small section which is perpendicular to the outgoing beam, as shown in Figure 4-13.

Different azimuthal sections are measured by rotating the mirror segment about the optical axis. The interferometry performed for testing of actuator movements uses a Zygo GPI interferometer with a 24 inch beam-expander. Figure 4-14 shows the PPI during testing.

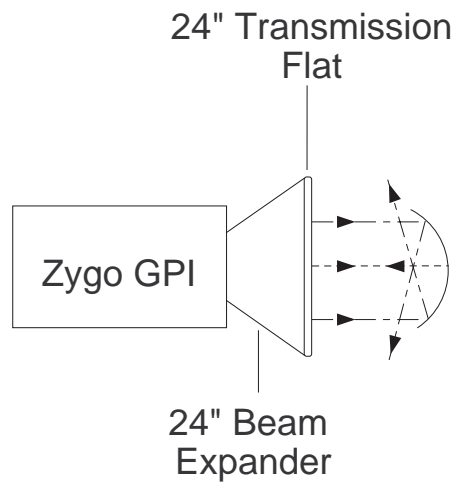


Figure 4-13. Collimated beam interferometry schematic

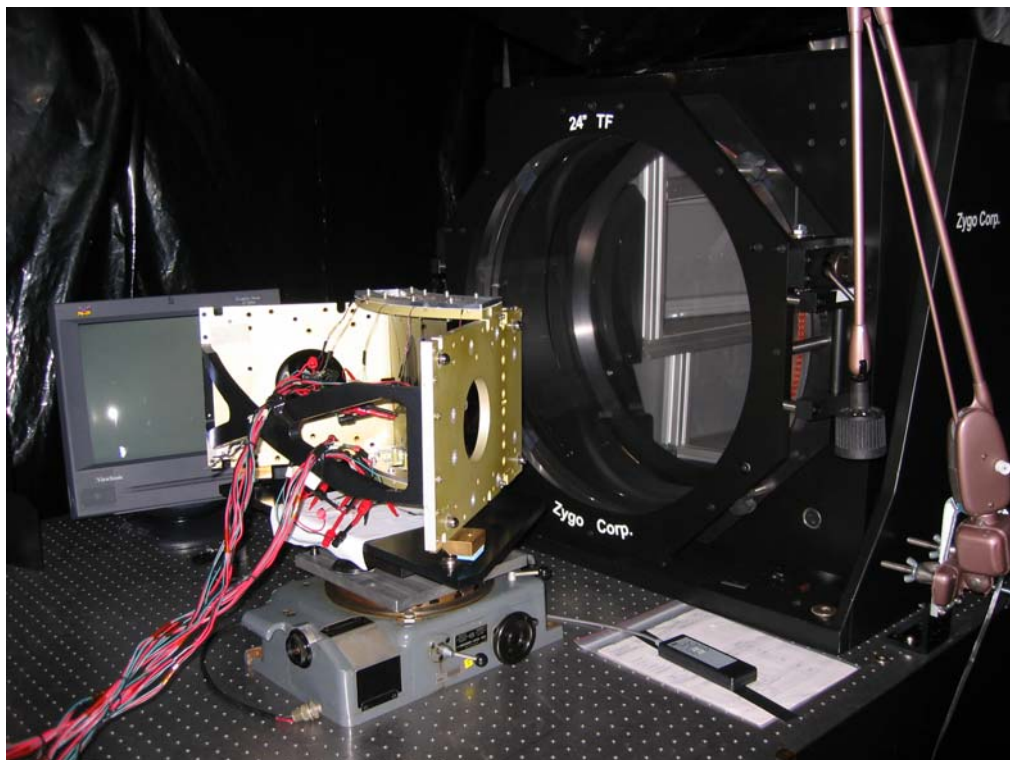


Figure 4-14. PPI during interferometry testing

4.4.2 Axial Interferometry Test Results

The design of the optics specifies that the axial sag of the mirrors is a smooth curve with a P-V of $1.107\ \mu\text{m}$ for a 494 series. For the purposes of the testing with the PPI, the majority of the testing investigates the azimuth positions which correspond to the actuator locations. Due to the over constraint of the optics, these locations are the most likely areas of induced deformations from installation and assembly which must be corrected. The axial profiles between actuator locations are also included, though significantly less manipulation is available at these points.

For the manipulation of the second-order axial figure, the primary motion utilized at azimuthal positions is the movement of the bottom and upper actuator in the same direction. This is referred to as a common-mode adjustment. This is shown in Figure 4-15. The constraints allowing the change in shape are the remaining attachment points. Ideally, this does not greatly affect the local cone angle of the optic and therefore has minimal impact on the CDA alignment. However, any actuator movement propagates to nearby mirror regions, and therefore an iterative process is still necessary to ensure alignment. Since only one set of actuators is moved for common mode adjustments with the remaining actuation points acting as constraints, it is not possible to affect the axial figure of the whole mirror. This common mode motion assumes that there is a nearly linear translation of motion between the slight curvilinear motion at the end of the bending piezoelectric actuator and the tip interface. As previously mentioned, the mirror must remain free to move in the axial direction to avoid imparting additional axial figure errors. The figure of the mirror is a second-order figure. Constraint of the optic or

constraint through excessive friction between the actuator and mirror surface may impart third-order errors or additional errors near the points of actuation.

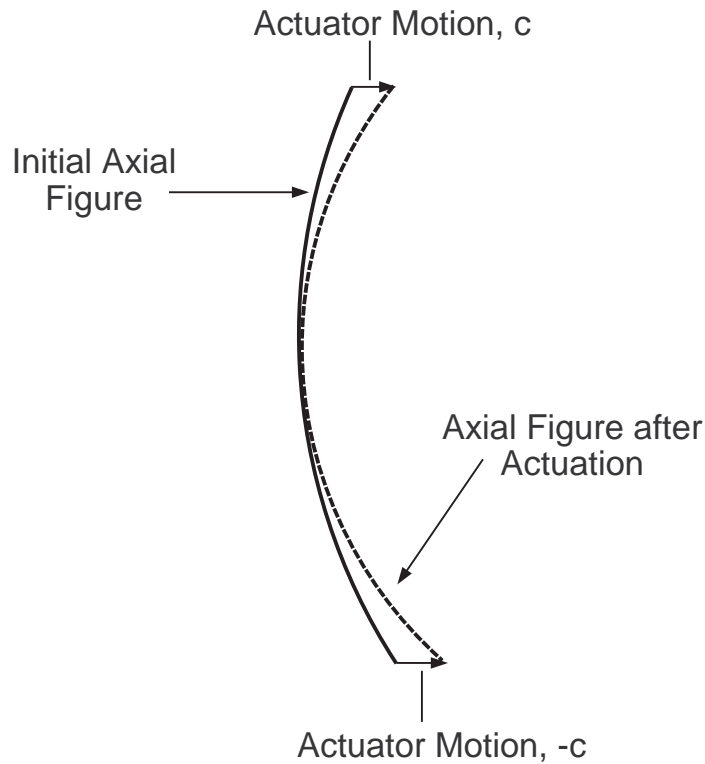


Figure 4-15. Common mode adjustment of actuators for axial figure manipulation

The initial interferometry on the mirror segment prior to installation or alignment is used as a comparison point for the axial interferometry taken during actuator movements, and is designated by “original data”. The initial interferometry on the mirror segment was taken of the mirror in its freestanding position, with two support points on the bottom of the mirror and one point at the center azimuth on the top of the mirror. For more information, see [58]. A direct comparison to the initial measurements is difficult for the presented data, as the difference in metrology used for initial measurements and measurements taken with actuation may result in slight deviations in the azimuth location measured on the mirror. The presentation of this data primarily represents the possibility of the actuators and tips to correct for the installation errors, as the initial measurements

were not compared against the various profiles during alignment but rather after actuator movements. For a true alignment, the use of an iterative process involving the use of the CDA and in-situ interferometry is necessary. However, this was not available at the time of testing, but will be used in future testing for complete alignments. Since in-situ interferometry was not available, the actuator locations are placed at the positions from the CDA alignment, and are annotated as “Initial CDA” on interferometry plots. Due to the hysteresis inherent in piezoelectric actuators and the lack of CDA feedback during interferometry, the actuators will not return to the precise alignment previously achieved.

The interferometry plots show two figures each. The first plot is the actual axial profile data from the interferometry. The second plot is the residual error from a second order polynomial curve fit of the axial profile. The RMS value given is the RMS of the residual, which is the difference between the data and the curve-fit, expressed in μm . The sag term given in the legend of the axial profile plot is the coefficient of the second order polynomial term, expressed in $\mu\text{m}/\text{m}^2$. For comparison, the ideal 494 secondary mirror sag in a zero-g environment of $1.107 \mu\text{m}$ has a second order coefficient of $110.7 \mu\text{m}/\text{m}^2$.

The B1 actuator was unavailable during interferometry testing. As a result, the data collected begins with the azimuth position P2. The axial interferometry at point P2 is given in Figure 4-16. The initial profile is significantly deformed from the desired concave up curvature. A large contributing factor to this deformation is the effect of the distortions at the neighboring point, P1, which was not actuated. However, the shape was manipulated to a similar configuration as the initial profile. The reason for the “step” annotation is that the data presented represents only several of the manipulation steps

using common mode actuator movements. As a note, each line on the axial profile plots contains several hundred data points, as opposed to limited number of markers shown, which are included to distinguish between interferometry profiles.

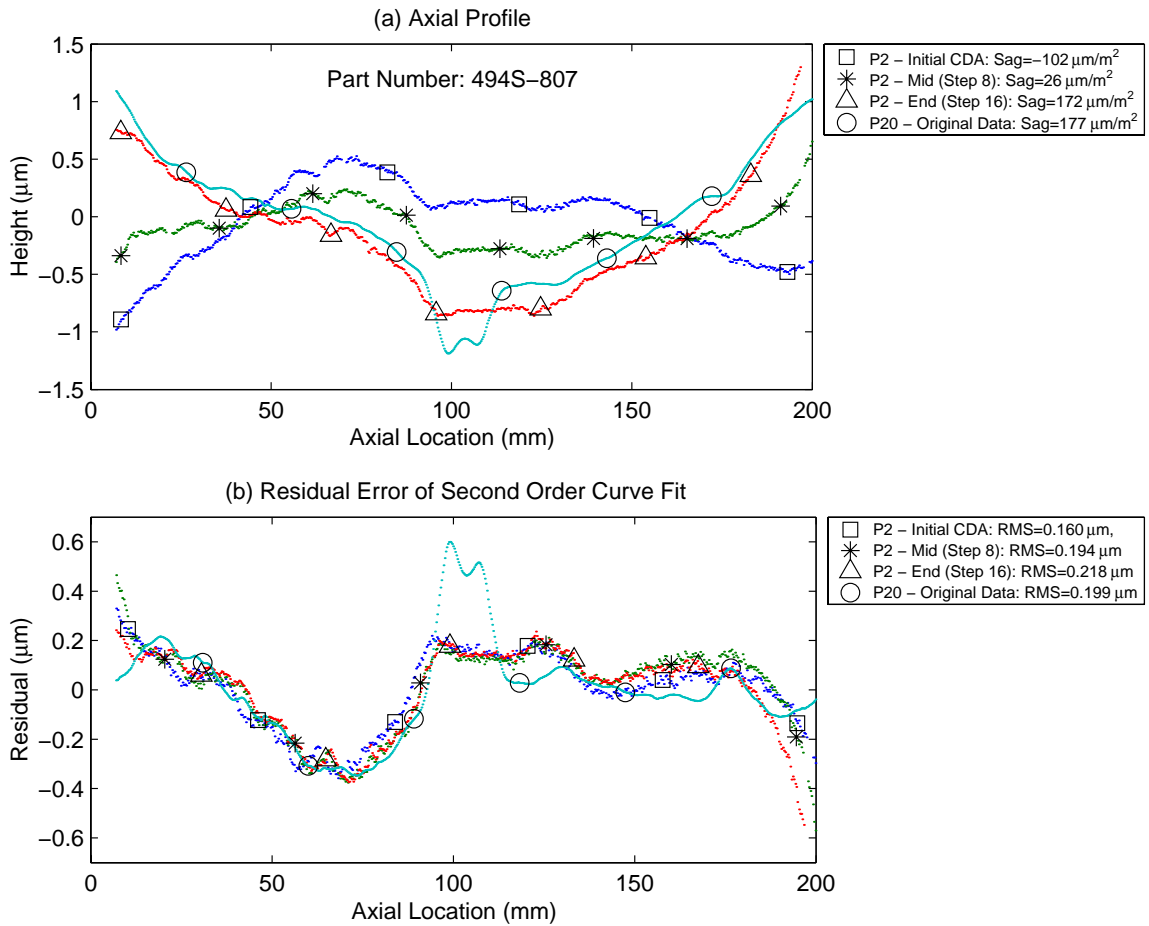


Figure 4-16. Axial interferometry plots for point P2

The axial interferometry at point P3 is given in Figure 4-17. As a note, there was a visible surface defect on the mirror coating which contributed to the abnormality on the plot near the location of 155 mm. In other actuator steps, the P-V of the profile could be affected as seen in other points, though it was unnecessary to deviate significantly from the initial CDA alignment for comparison of the pre-installation profile.

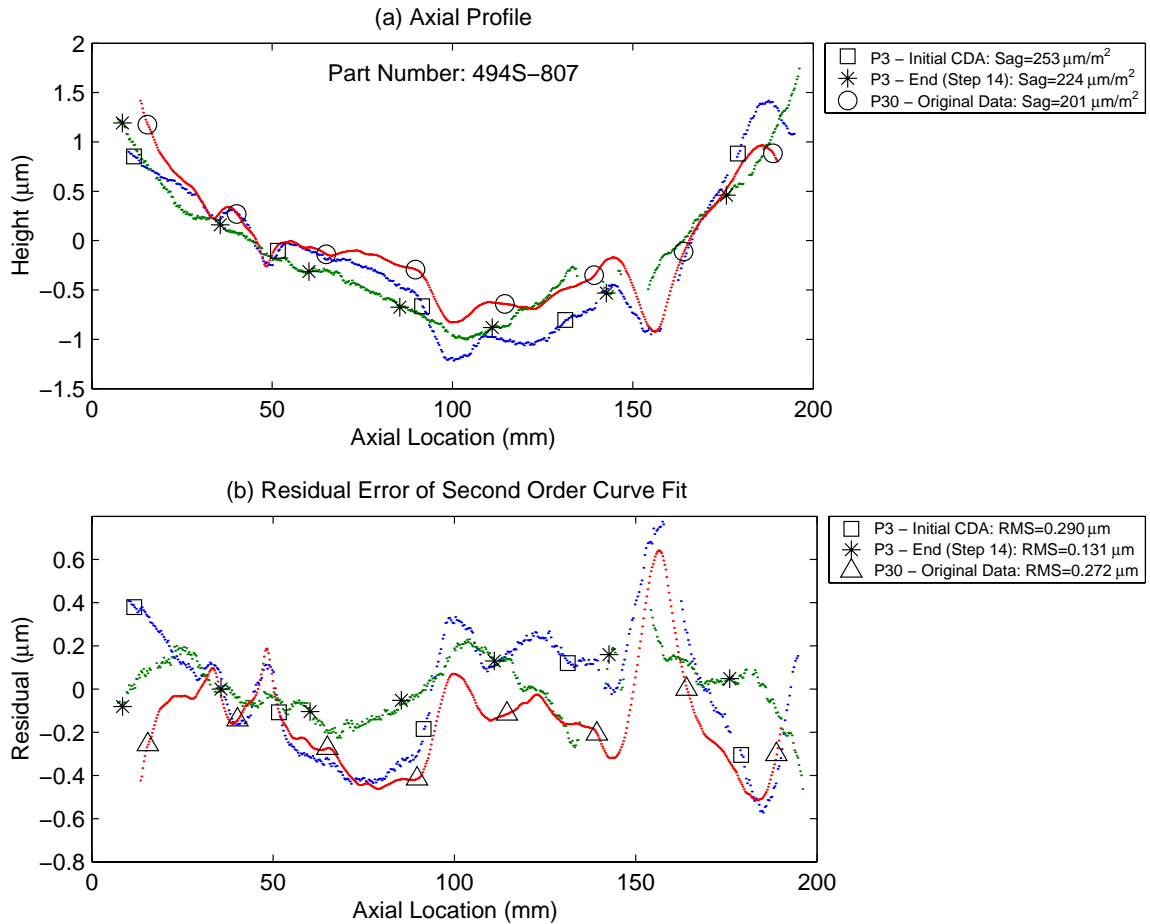


Figure 4-17. Axial interferometry plots for point P3

The axial interferometry at point P4 is given in Figure 4-18. Minimal movement was necessary at this point to resemble the initial interferometry profile. The discrepancy between the residual for the actuated profiles and the residual on the original data is likely due to a difference between the original measurement azimuth location and the actuated azimuth location.

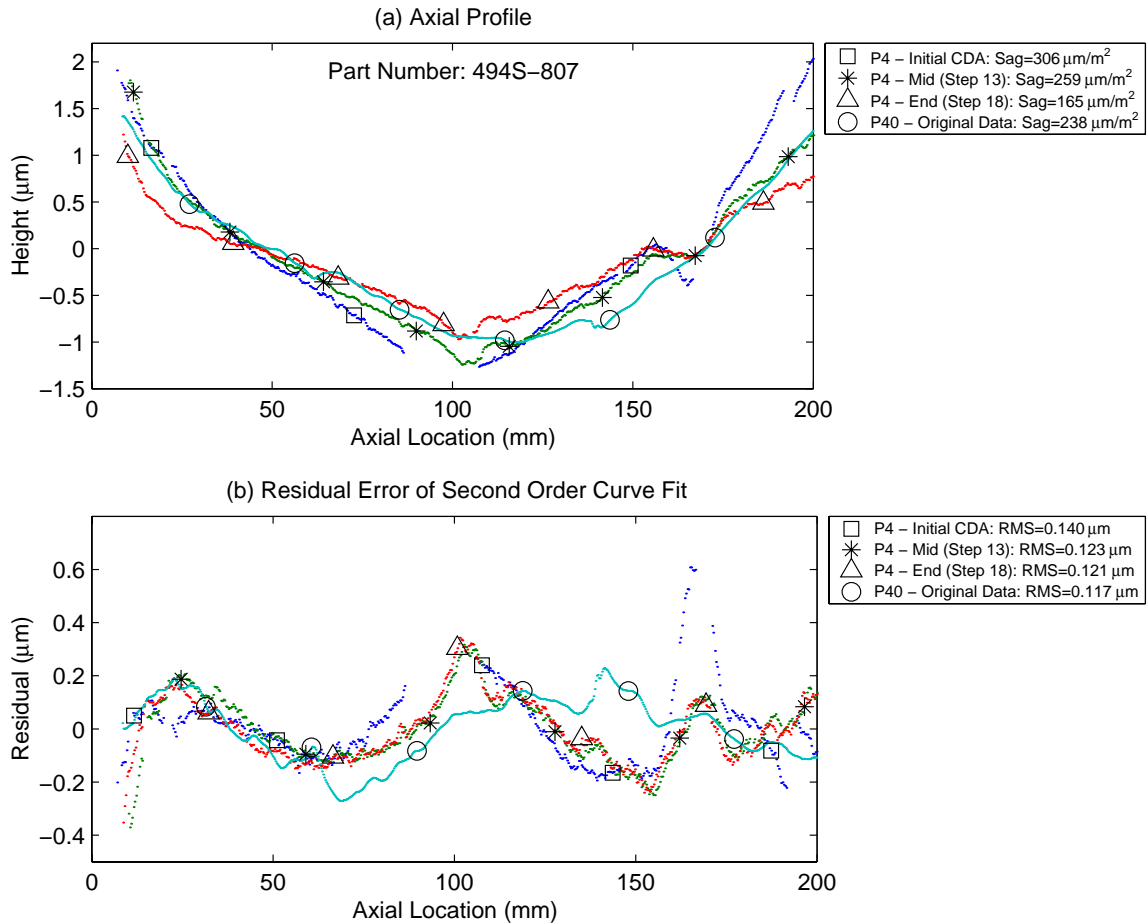


Figure 4-18. Axial interferometry plots for point P4

The axial interferometry at point P5 is given in Figure 4-19. This point showed the greatest discrepancy between the desired P-V curvature and the actual curvature shown after CDA alignment positions. This discrepancy is expected due to the increased compliance of the mirror ends and lack of the constraint of adjacent points seen at the other azimuth locations. However, the axial profile at the actuation point remains adjustable through common mode actuations. If the original data was utilized during the actuator alignment, additional steps would have been taken to further match the initial profile. In comparison with the other points, the need for axial interferometry during alignment, especially near the mirror ends, is apparent if that section of the mirror is going to be considered for x-ray collection.

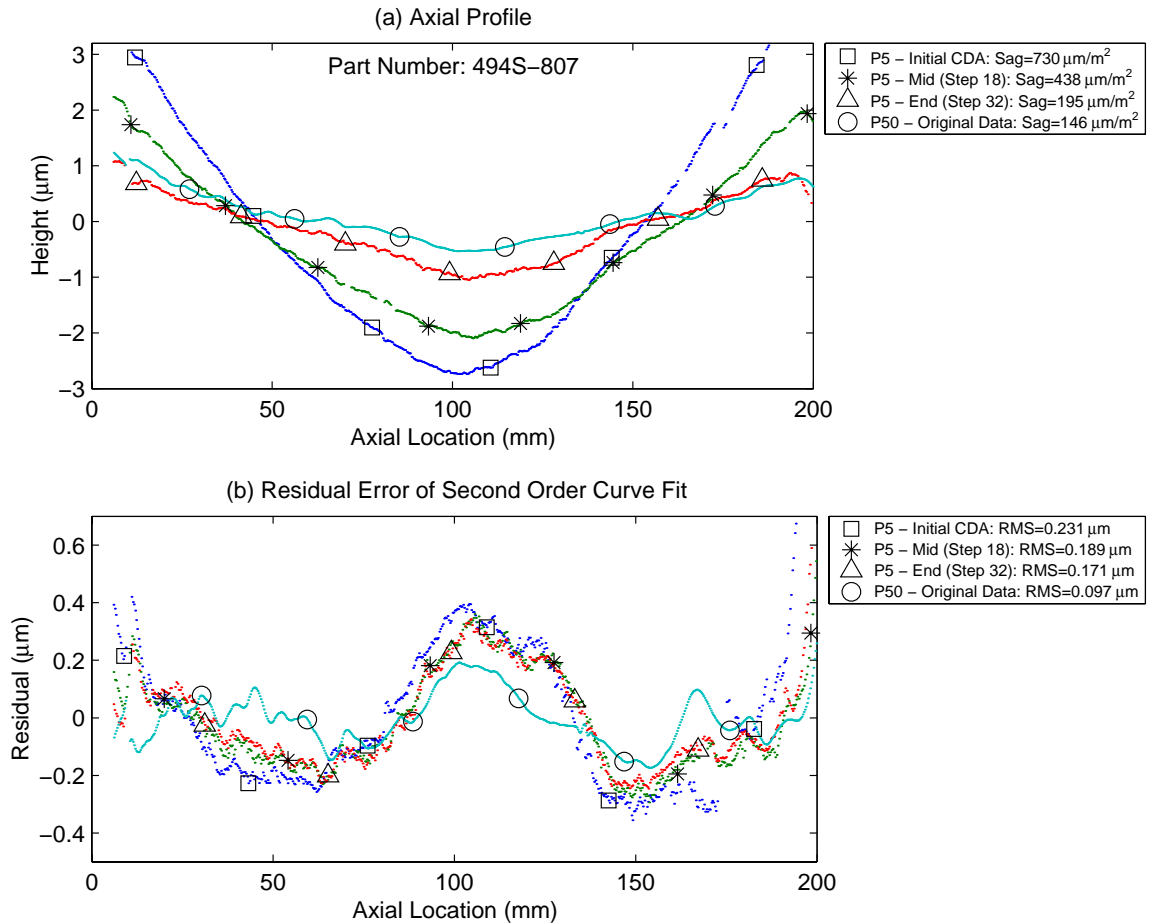


Figure 4-19. Axial interferometry plots for point P5

The axial interferometry at azimuth positions midway between points P2, P3, P4, and P5 is given in Figure 4-20. Initial interferometry was not available for comparison. However, it should be of note that there are not discrepancies along the curvature as large as was seen in other points. The plots are shifted in the vertical direction of the plots for clarity, and the scale remains the same.

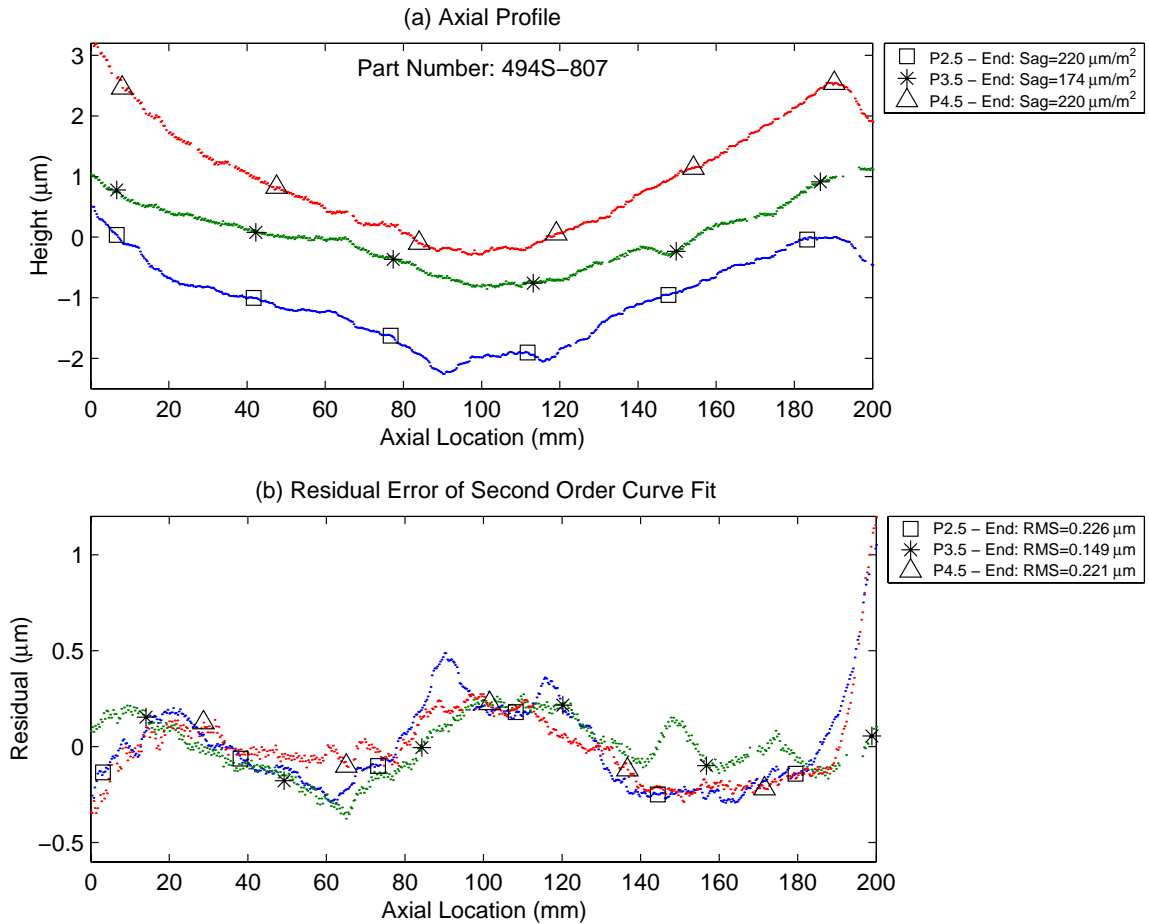


Figure 4-20. Axial profiles of intermediate positions

The greatest amount of adjustability was exhibited at the actuator locations on the mirror. The effects of the actuator movements decrease as the azimuth location of the interferometry profile move away from the actuator locations. The significance of this is that the distortion of the initial mirror profile due to installation is not as significant between actuator location, which is beneficial if the correct axial profile curvature can be produced during the mirror forming and replication process. The other significance of the intermediate positions is that if the correct axial profile curvature cannot be produced in the mirror forming process, the ability to influence the axial profile is minimal for locations in between actuator azimuths.

As previously discussed, the movements shown were intended for a general profile and demonstration of movement using the actuators. The significance of the axial interferometry results is that the errors induced during mirror installation and constraint may be minimized. However, there will likely be a tradeoff between the alignment of the axial sag and the quality of the CDA alignment. Additional research with simultaneous interferometry and CDA feedback will be beneficial in understanding the relationship between the common mode adjustments for axial sag adjustment and differential mode adjustments for local cone angle adjustment. This information can be utilized in the iterative alignment process necessary between the CDA alignment and interferometry alignment until the predicted mirror performance is within specifications.

4.4.3 Future Alignment Characterization

In order to determine the expected performance of an aligned mirror segment, information on the radial distances of all points on the mirror segment surface is needed in addition to the CDA and axial interferometry measurements. Normal incidence metrology which looks at the entire mirror surface is one method of accomplishing this. The normal incidence metrology selected uses interferometry in conjunction with a computer generated hologram (CGH) or null lens to allow for the characterization of the mirror surface. Future alignment work, including the alignment of PPII, will utilize this type of metrology for a complete understanding of the mirror segment alignment and expected performance.

CHAPTER 5

CONCLUSIONS

The design and testing of a piezoelectric actuator assembly has been completed for a single thin foil mirror segment. The second generation piezoelectric actuator assembly design is complete for the alignment of a mirror segment pair. The use of piezoelectric actuators has shown promise in its capability to adjust the local cone angle at azimuths on a mirror segment for alignment using CDA techniques. The CDA alignment achieved is currently the best alignment achieved out of the actuator alignment techniques tested for Constellation-X, although it should be noted this was only for a single mirror segment. It should be also of note that the CDA alignment is only a small contribution to the overall achievable imaging resolution [59]. The use of piezoelectric actuators has shown the ability to adjust the second order axial profile of the mirror segments at the actuator azimuth positions to minimize installation error. The next step of testing utilizing CDA alignment and in-situ interferometry to align a mirror pair in the PPII assembly will be an important step in the demonstration of using piezoelectric actuators to align thin foil segmented x-ray optics.

5.1 Recommendations

The use of piezoelectric actuators has shown great potential in aligning segmented optics. Further development in the possibility of assembly and alignment of many thinly nested mirrors is needed. The use of flexural elements for struts creates an intricate assembly which is effective for the location of piezoelectric actuators for one mirror pair. In order to develop this concept further, it may be advised to utilize a flexural positioning strut frame with piezoelectric actuators as an alignment tool that is used only during the

assembly and alignment of the mirror segments within the SXT mirror assembly. A separate and simplified bonding frame can be utilized to secure the mirrors within a flight assembly. After bonded, the flexural positioning strut frame and piezoelectric actuators can be removed. This configuration allows the design to have the desired bonding points which are not limited to the points of actuation, which may allow the bonding points to be optimized for thermal, structural, and collecting area considerations. This was the case for the design which incorporates flexural struts with integrated bonding slots as used in the PPII. A separate bonding frame allows the mechanical elements to have greater stiffness than the flexural elements. Also, the use of a separate bonding frame may increase the effective collecting area by utilizing rigid struts which are not as wide as the piezoelectric actuator struts, whose size is dictated by the actuator size.

If more consistent behavior is needed for the flexural translation stage, the use of a double compound rectilinear spring may be utilized as the increased collecting area blockage will not be an issue once the flexural positioning stage is removed after alignment. The integration of tilt adjustments for individual mirrors will be necessary as the number of mirror pairs is increased. Currently, the rigid body tip and tilt motions are accomplished through housing rotations with at the kinematic mount interface points. Individual mirror alignment capability is therefore necessary, which should be integrated into the assembly structure which is removed after alignment and bonding.

5.2 Future Work

The testing that was accomplished with a single mirror is only the start of the development of using piezoelectric actuators for the alignment of segmented mirrors. Near term future work includes the assembly and testing of the second generation

piezoelectric actuator assembly, which is in progress as of this writing. The use of full aperture interferometry for normal incidence metrology will be beneficial in looking at the piezoelectric actuator effects on the axial figure across the entire surface of the mirror during alignment and a better characterization of the alignment of PPII. The alignment, bonding, and x-ray testing of the PPII assembly are the next steps in using piezoelectric actuators for mirror alignment.

Further work on the discussion on piezoelectric actuators given in section 3.4 will be beneficial to the development of an efficient closed loop system for driving the movements of the actuators with relation to stiffness of a mirror segment. This closed loop system can also take into account the necessary cone angle adjustments as determined by the location of CDA spots and the desired second order axial figure. Further analysis and experimentation will also be beneficial in validating the stiffness models of both the positioning system and mirror segments. The further development of tips and piezoelectric actuators with decreasing size will be necessary to adapt the alignment techniques and assemblies to mirror assemblies with small clearances between mirror segments. Future in-depth analysis includes studying the fundamental frequencies of the entire flexure strut frame assembly with actuators. This is important from a metrology perspective. Finally, the further development of the collimated light testing utilizing CCD cameras for analysis and alignment during testing could improve the achievable alignment before using CDA methods.

Appendix A: Matlab Scripts

The first two Matlab scripts may be utilized for the determination of Hertzian contact stresses in the selection of tip curvature sizing for tips of the configuration described in section 3.2.2. The third Matlab script may be utilized for the determination of flexure dimensions for a parallel-two beam flexure strut, as described in section 3.3.

A.1 Tip Design for Crossed Cylinders

```
%-----  
% Cylinders crossed at a right angle  
% Author: Thomas Meagher  
% Description: For the Hertzian contact problem of two cylinders crossed  
% at right angles, this script solves for and plots the maximum contact  
% pressure and tensile stresses at the ends of the semimajor and semiminor  
% axes of the contact area. This is plotted for varying sizes of the  
% interface tip and varying loads  
%-----  
  
% Clear all previous variables  
clear all;  
close all;  
  
% Define the material properties of the two cylinders  
E1=78e9; % Pa - Young's Modulus for Body #1 (Allvac Ti-15Mo)  
v1=.33; % Poisson's Ratio for Body #1 (Allvac Ti-15Mo)  
E2=72.9e9; % Pa - Young's Modulus for Body #2 (Mirror Substrate)  
v2=0.208; % Poisson's Ratio for Body #2 (Mirror Substrate)  
  
% Define the loads of actuation between the cylinders  
P1=[0.0002 0.001 0.007]; % N  
  
% Define the range of diameters of interest  
D1_1=linspace(0.000000001,0.005,100); % m  
  
% Define the diameter of the second cylinder (this is approximated as  
% the diameter of the mirror segments at the P-H intersection of the  
% 494 series mirror)  
D2=0.4943001236; % m  
  
% Create a mesh of the possible diameters and loads  
[D1,P]=meshgrid(D1_1,P1);  
% Get the number of combinations for loops  
[r,c]=size(D1);  
  
% Calculate the term, K  
K=D1.*D2./(D2+D1);  
  
% Calculate the inverse of the equivalent Young's modulus  
gam=(1-v1^2)/E1+(1-v2^2)/E2;  
  
% Calculate the A and B matrices for the two cylinders  
A=1./D2*ones(r,c);  
B=1./D1;
```

```

A_B=A./B;

% Calculate coefficients based on a curve fit determined using Excel
% of the tabulated data available in Table 9-3, p. 446 from Pilkey, Walter.
% Formulas for Stress, Strain, and Structural Matrices. 2nd Ed. Hoboken:
% John Wiley & Sons, 2005.

for i=1:r
    for j=1:c
        if A_B==1
            n_a(i,j)=1;
            n_b(i,j)=1;
            n_c(i,j)=1;
            n_d(i,j)=1;
        elseif A_B<0.05
            n_a(i,j)=0.9727*A_B(i,j)^(-0.3927);
            n_b(i,j)=0.8266*A_B(i,j)^0.2006;
            n_c(i,j)=1.2329*A_B(i,j)^0.1909;
            n_d(i,j)=1.4192*A_B(i,j)^0.2462;
        else
            n_a(i,j)=0.9727*A_B(i,j)^(-0.3927);
            n_b(i,j)=2.2461*A_B(i,j)^5-6.7483*A_B(i,j)^4+7.8948*A_B(i,j)^3-4.6986*A_B(i,j)^2+1.9333*A_B(i,j)+0.3761;
            n_c(i,j)=3.9737*A_B(i,j)^5-11.856*A_B(i,j)^4+13.797*A_B(i,j)^3-8.081*A_B(i,j)^2+2.5799*A_B(i,j)+0.595;
            n_d(i,j)=4.7254*A_B(i,j)^5-14.043*A_B(i,j)^4+16.227*A_B(i,j)^3-9.3705*A_B(i,j)^2+2.9111*A_B(i,j)+0.5607;
        end
    end
end

% Calculate the elliptical contact area dimensions
a=0.909*n_a.*(gam*P.*K).^(1/3);
b=0.909*n_b.*(gam*P.*K).^(1/3);

% Calculate the eccentricity of the contact area
ecc=sqrt(1-(b./a).^2);

% Calculate the rigid distance of approach
d=0.825*n_d.*(gam^2*(P.^2)./(K)).^(1/3);

% Calculate the maximum contact pressure
p_o=3*P./(2*pi*a.*b);

% Calculate the tensile normal stress at the ends of the semimajor axis in glass
stress_semimaj=p_o*(1-2*v2).*b./(a.*ecc.^2).*(1./ecc.*atanh(ecc)-1);
% Calculate the tensile normal stress at the ends of the semimajor axis in glass
stress_semimin=p_o*(1-2*v2).*b./(a.*ecc.^2).*(1-b./(a.*ecc).*atan(ecc.*a./b));

% Specify conversion factors used for plotting
mm=1000;
MPa=1e6;

% Specify an interval of data points for plotting markers
n=10:25:100;

% Plot the maximum contact pressure
plot(D1(1,:)*mm,p_o(1,:)/MPa,'k',D1(2,:)*mm,p_o(2,:)/MPa,'k',D1(3,:)*mm,p_o(3,:)/MPa,'k');
hold on;
p=plot(D1(1,n)*mm,p_o(1,n)/MPa,'kd',D1(2,n)*mm,p_o(2,n)/MPa,'k*',D1(3,n)*mm,p_o(3,n)/MPa,'ks');
xlabel('D_1 (mm)'); ylabel('p_o (MPa)');
axis([0 5 0 160]);
legend(p, [num2str(P1(1)) ' N'], [num2str(P1(2)) '0 N'],[num2str(P1(3)) '0 N'],1);

```

```

text(0.5,152,'Material 1:Allvac Ti-15Mo');
text(0.5,145,'Material 2:Schott D-263 Glass');
text(0.5,136,'D_2=494 Series P-H Intersection Diameter (~494 mm)');

% Save the file as a .png figure
print right_cylinders_pressure.png -dpng
% Save file as a .eps figure
print right_cylinders_pressure.eps -deps2

% Open a new figure
figure

% Plot the maximum tensile stress in the glass at the edge of contact at the semimajor axis
% This is where the maximum tensile stress occurs
plot(D1(1,:)*mm,stress_semimaj(1,:)/MPa,'k',D1(2,:)*mm,stress_semimaj(2,:)/MPa,'k',D1(3,:)*mm,stress_semimaj(3,:)/MPa,'k');
hold on;
% Plot markers to distinguish the lines
p=plot(D1(1,n)*mm,stress_semimaj(1,n)/MPa,'kd',D1(2,n)*mm,stress_semimaj(2,n)/MPa,'k*',D1(3,n)*mm,stress_semimaj(3,n)/MPa,'ks');
xlabel('D_1 (mm)'); ylabel('\sigma_t (MPa)');
axis([0 5 0 3]);
legend(p, [num2str(P1(1)) ' N'], [num2str(P1(2)) '0 N'],[num2str(P1(3)) '0 N'],1);
text(0.1,2.85,'Material 1:Allvac Ti-15Mo');
text(0.1,2.70,'Material 2:Schott D-263 Glass');
text(0.1,2.53,'D_2=494 Series P-H Intersection Diameter (~494 mm)');

% Save file as a .png figure
print right_cylinders_stress_semimajor.png -dpng
% Save file as a .eps figure
print right_cylinders_stress_semimajor.eps -deps2

% Open a new figure
figure

% Plot the maximum tensile stress in the glass at the edge of contact at the semiminor axis
plot(D1(1,:)*mm,stress_semimin(1,:)/MPa,'k',D1(2,:)*mm,stress_semimin(2,:)/MPa,'k',D1(3,:)*mm,stress_semimin(3,:)/MPa,'k');
hold on;
% Plot markers to distinguish the lines
p=plot(D1(1,n)*mm,stress_semimin(1,n)/MPa,'kd',D1(2,n)*mm,stress_semimin(2,n)/MPa,'k*',D1(3,n)*mm,stress_semimin(3,n)/MPa,'ks');
xlabel('D_1 (mm)'); ylabel('\sigma_t (MPa)');
axis([0 5 0 1]);
legend(p, [num2str(P1(1)) ' N'], [num2str(P1(2)) '0 N'],[num2str(P1(3)) '0 N'],1);
text(0.1,0.95,'Material 1:Allvac Ti-15Mo');
text(0.1,0.90,'Material 2:Schott D-263 Glass');
text(0.1,0.84,'D_2=494 Series P-H Intersection Diameter (~494 mm)');

% Save file as a png figure
print right_cylinders_stress_semiminor.png -dpng
% Save file as a .eps figure
print right_cylinders_stress_semiminor.eps -deps2

```

A.2 Tip Design for a Sphere within a Cylindrical Race

```

%-----
% Sphere within a spherical race
% Author: Thomas Meagher
% Description: For the Hertzian contact problem of a sphere within a
% spherical race, this script solves for and plots the maximum contact
% pressure and tensile stresses at the ends of the semimajor and semiminor

```

```

% axes of the contact area. This is plotted for varying sizes of the
% interface tip and varying loads
%-----

% Clear all previous variables
clear all;
close all;

% Define the material properties of the two cylinders
E1=344.7e9; % Pa - Young's Modulus for Body #1 (Synthetic Sapphire)
v1=.33; % Poisson's Ratio for Body #1 (Synthetic Sapphire)
E2=72.9e9; % Pa - Young's Modulus for Body #2 (Mirror Substrate)
v2=0.208; % Poisson's Ratio for Body #2 (Mirror Substrate)

% Define the loads of actuation between the cylinders
P1=[0.0002 0.001 0.007]; % N

% Define the range of diameters of interest
D1_1=linspace(0.000000001,0.005,100); % m

% Define the diameter of the cylindrical race (this is approximated as
% the diameter of the mirror segments at the P-H intersection of the
% 494 series mirror)
D2=0.4943001236; % m

% Create a mesh of the possible diameters and loads
[D1,P]=meshgrid(D1_1,P1);
% Get the number of combinations for loops
[r,c]=size(D1);

% Calculate the term, K
K=(0.5*D1).*(0.5*D2)/(D2-0.5*D1);

% Calculate the inverse of the equivalent Young's modulus
gam=(1-v1^2)/E1+(1-v2^2)/E2;

% Calculate the A and B matrices for the two cylinders
A=0.5*(1./(0.5*D1)-1./(0.5*D2));
B=1./D1;
A_B=A./B;

% Calculate coefficients based on a curve fit determined using Excel
% of the tabulated data available in Table 9-3, p. 446 from Pilkey, Walter.
% Formulas for Stress, Strain, and Structural Matrices. 2nd Ed. Hoboken:
% John Wiley & Sons, 2005.

for i=1:r
    for j=1:c
        if A_B==1
            n_a(i,j)=1;
            n_b(i,j)=1;
            n_c(i,j)=1;
            n_d(i,j)=1;
        elseif A_B<0.05
            n_a(i,j)=0.9727*A_B(i,j)^(-0.3927);
            n_b(i,j)=0.8266*A_B(i,j)^0.2006;
            n_c(i,j)=1.2329*A_B(i,j)^0.1909;
            n_d(i,j)=1.4192*A_B(i,j)^0.2462;
        else
            n_a(i,j)=0.9727*A_B(i,j)^(-0.3927);
            n_b(i,j)=2.2461*A_B(i,j)^5-6.7483*A_B(i,j)^4+7.8948*A_B(i,j)^3-4.6986*A_B(i,j)^2+1.9333*A_B(i,j)+0.3761;
        end
    end
end

```

```

n_c(i,j)=3.9737*A_B(i,j)^5-11.856*A_B(i,j)^4+13.797*A_B(i,j)^3-8.081*A_B(i,j)^2+2.5799*A_B(i,j)+0.595;
n_d(i,j)=4.7254*A_B(i,j)^5-14.043*A_B(i,j)^4+16.227*A_B(i,j)^3-9.3705*A_B(i,j)^2+2.9111*A_B(i,j)+0.5607;
end
end
end

% Calculate the elliptical contact area dimensions
a=1.145*n_a.*(gam*P.*K).^(1/3);
b=1.145*n_b.*(gam*P.*K).^(1/3);

% Calculate the eccentricity of the contact area
ecc=sqrt(1-(b./a).^2);

% Calculate the rigid distance of approach
d=0.655*n_d.*(gam^2*(P.^2)./(K)).^(1/3);

% Calculate the maximum contact pressure
p_o=3*P./(2*pi*a.*b);

% Calculate the tensile normal stress at the ends of the semimajor axis in glass
stress_semimaj=p_o*(1-2*v2).*b./(a.*ecc.^2).*(1./ecc.*atanh(ecc)-1);
% Calculate the tensile normal stress at the ends of the semimajor axis in glass
stress_semimin=p_o*(1-2*v2).*b./(a.*ecc.^2).*(1-b./(a.*ecc).*atan(ecc.*a./b));

% Specify conversion factors used for plotting
mm=1000;
MPa=1e6;

% Specify an interval of data points for plotting markers
n=10:25:100;

% Plot the maximum contact pressure
plot(D1(1,:)*mm,p_o(1:)/MPa,'k',D1(2,:)*mm,p_o(2:)/MPa,'k',D1(3,:)*mm,p_o(3:)/MPa,'k');
hold on;
p=plot(D1(1,n)*mm,p_o(1,n)/MPa,'kd',D1(2,n)*mm,p_o(2,n)/MPa,'k*',D1(3,n)*mm,p_o(3,n)/MPa,'ks');
xlabel('D_1 (mm)'); ylabel('p_o (MPa)');
axis([0 5 0 500]);
legend(p, [num2str(P1(1)) ' N'], [num2str(P1(2)) '0 N'],[num2str(P1(3)) '0 N'],1);
text(1.1,475,'Material 1:Synthetic Sapphire');
text(1.1,450,'Material 2:Schott D-263 Glass');
text(1.1,420,'D_2=494 Series P-H Intersection Diameter (~494 mm)');

% Save the file as a .png figure
print sphere_in_race_pressure.png -dpng

% Save file as a .eps figure
print sphere_in_race_pressure.eps -deps2

% Open a new figure
figure

% Plot the maximum tensile stress in the glass at the edge of contact at the semimajor axis
% This is where the maximum tensile stress occurs
plot(D1(1,:)*mm,stress_semimaj(1:)/MPa,'k',D1(2,:)*mm,stress_semimaj(2:)/MPa,'k',D1(3,:)*mm,stress_semimaj(3:)/MPa,'k');
hold on;
% Plot markers to distinguish the lines
p=plot(D1(1,n)*mm,stress_semimaj(1,n)/MPa,'kd',D1(2,n)*mm,stress_semimaj(2,n)/MPa,'k*',D1(3,n)*mm,stress_semimaj(3,n)/MPa,'ks');
xlabel('D_1 (mm)'); ylabel('\sigma_t (MPa)');

```

```

axis([0 5 0 100]);
legend(p, [num2str(P1(1)) ' N'], [num2str(P1(2)) '0 N'],[num2str(P1(3)) '0 N'],1);
text(.8,95,'Material 1:Synthetic Sapphire');
text(.8,90,'Material 2:Schott D-263 Glass');
text(.8,84,'D_2=494 Series P-H Intersection Diameter (~494 mm)');

% Save file as a .png figure
print spher_in_race_stress_semimajor.png -dpng

% Save file as a .eps figure
print spher_in_race_stress_semimajor.eps -deps2

% Open a new figure
figure

% Plot the maximum tensile stress in the glass at the edge of contact at the semiminor axis
plot(D1(1,:)*mm,stress_semimin(1,:)/MPa,'k',D1(2,:)*mm,stress_semimin(2,:)/MPa,'k',D1(3,:)*mm,stress_semimin(3,:)/MPa,'k');
hold on;
% Plot markers to distinguish the lines
p=plot(D1(1,n)*mm,stress_semimin(1,n)/MPa,'kd',D1(2,n)*mm,stress_semimin(2,n)/MPa,'k*',D1(3,n)*mm,stress_semimin(3,n)/MPa,'ks');
xlabel('D_1 (mm)'); ylabel('\sigma_t (MPa)');
axis([0 5 0 100]);
legend(p, [num2str(P1(1)) ' N'], [num2str(P1(2)) '0 N'],[num2str(P1(3)) '0 N'],1);
text(.8,95,'Material 1:Synthetic Sapphire');
text(.8,90,'Material 2:Schott D-263 Glass');
text(.8,84,'D_2=494 Series P-H Intersection Diameter (~494 mm)');

% Save file as a png figure
print sphere_in_race_stress_semiminor.png -dpng

% Save file as a .eps figure
print sphere_in_race_stress_semiminor.eps -deps2

```

A.3 Parallel Two-beam Flexure Strut Design

```

%-----
% Symmetrical Parallel Two-Beam Flexure Strut Design
% Author: Thomas Meagher
% Description: Contour plot of the possible t and L combinations for
% the design of a parallel beam flexure system with 4 flexure hinges
%-----

% Clear all previous variables
clear all;
close all;

% Define the material properties
E=78E9; % Pa - Modulus of Elasticity (Allvac Ti-15Mo)
Sy=483E6; % Pa - Yield Stress (Allvac Ti-15Mo)

% Desired factor of safety on stress
FS_s=2;
% Calculate the desired design stress
stress_d=Sy/FS_s;

% Specify the depth, b, of the flexure
b=0.010; % meters

% Specify the desired displacement of the entire flexure
y=0.0003; % meters

```

```

% Specify the maximum axial force of the actuator or adjuster for the
% desired travel. For this application, a fine pitch screw
% (M3.0-0.20 mm) is used, and the maximum desired axial force is
% specified in lbf and converted to Newtons
F_max_lb=15; % lbf
F_max_N=F_max_lb*4.448221615; % N

% Specify a factor of safety for the actuator/adjuster applied force
FS_f=1.2;

% Calculate the desired force from actuator/adjuster
F=F_max_N/FS_f; % N

% Specify the number of flexure pairs
% This is four, as the design is symmetric, with two pairs on each end
n=4;

% Target stiffness in the direction of motion per flexure pair
k_m_target=F/y/n;

% Define the length and thickness values for the beam to look at
L1=linspace(0.0001,0.010,50);
t1=linspace(0.00001,0.0003,50);

% Create a mesh of possible length and thickness values
[L,t]=meshgrid(L1,t1);

% Specify conversion factors used for plotting
f=1000; % mm

% Calculate the out-of plane stiffness for the flexure
k_z=2*E*t.*b^3./L.^3;

% Define parameters for the area moment of inertia and equivalent
% stiffness in the direction of desired movement
I=1/12*b*t.^3;
k_eq=(6*E*I./L.^3).*n;

% Plot a contour of out-of plane stiffness (N/m)
v=[8e6 2e7 4e7 6e7 8e7 1e8 1.5e8 2e8 3e8 5e8 8e8 2e9 3e9 1e10 5e10];
v_1=length(v);
[c,h]=contour(t*f,L*f,k_z,v);
xlabel('t (mm)'); ylabel('L (mm)');
axis([0*f 0.0003*f 0*f .01*f]);
h=clabel(c,h,v,'labelspacing',500);
set(h,'FontSize',8);
for i=1:v_1
set(h(i),'String',[num2str(v(i),3)])
end

% Keep the figure open
hold on;

% Plot the constraint on the length from the stiffness and actuator force
% The length must be greater than this line (above it)
L_st=(n*E*b*t.^3.*y./F).^(1/3);
p1=plot(t1*f,L_st*f,'r-');
set(p1,'LineWidth',2)

% Plot the constraint on the length from a design stress standpoint
% The length must be greater than this line (above it)

```

```

L_t=sqrt(3*E*t.*y./2./stress_d);
p2=plot(t1*f,L_t*f,'k--');
set(p2,'LineWidth',2)

% Add additional constraints for machining considerations
% Specify that t should be greater than 0.0001 m
t_m=0.0001*ones(1,length(L1));
p3=plot(t_m*f,L1*f,'k');
set(p3,'LineWidth',2)

% For space restrictions, there may be a limit on L
% L should be less than this (below it)
L_space=0.008*ones(1,length(t1));
p4=plot(t1*f,L_space*f,'k');
set(p4,'LineWidth',2)

% Create a legend for the different constraints
% legend([p1(1),p2(1),p3,p4],'Stiffness','Design Stress','Machining','Space Limit',4);
legend([p1(1),p2(1),p3,p4],'Stiffness - Eqn. 3-53','Design Stress - Eqn. 3-54','Machining','Space Limit',4);

% Annotate the constants used
rectangle('Position',[.155,8.15,.149,1.8],'FaceColor','w');
text(.16,9.6,'Material: Allvac Ti-15Mo');
text(.16,9.1,['Depth = 'num2str(b*1000) ' mm']);
text(.25,9.6,['\sigma_d = 0.5*\sigma_y']);
text(.25,9.1,['F_y = 'num2str(F,3) ' N']);
text(.16,8.6,['Contour Line Units: N/m']);

% Add lines for design space
xx=linspace(0.0001,0.0002213,10);
plot([xx*f,xx*f],[sqrt(3*E*xx.*y./2./stress_d)*f,ones(1,length(xx))*0.008*f],'k-');
xx=linspace(0.000235,0.0003,7);
plot([xx*f,xx*f],[(n*E*b*xx.^3.*y./F).^(1/3)*f,ones(1,length(xx))*0.008*f],'k-');

% Save file as a png figure
print flexure_design_space.png -dpng
% Save file as a .eps figure
print flexure_design_space.eps -depsc2

```

Appendix B: Actuator Movements for CDA Alignment Steps

The following tables show all of the voltage changes and resulting I_{RMS} values for the CDA alignment trials given in section 4.3.3. The voltage settings for each alignment trial started with the voltage settings obtained during the collimated beam testing, as given in Table B-1.

Table B-1. Starting voltage settings from collimated beam testing

Actuator	U1	U2	U3	U4	U5	B1	B2	B3	B4	B5
Voltage (V)	84.2	75.0	122.8	102.2	105.1	110.6	80.0	63.7	75.0	90.0

The alignment trial tables contain the step number of the voltage changes. The spot movement column denotes the aperture mask position that was the focus of the motion. The channel, sign, and voltage give the movements for the step. The I_{RMS} is given in terms of the radial value for the focal length and accounting for the double pass system as well as given in the actual value from the quad-cell detector of the CDA. The steps where “Adjust Mask” is listed refers to the verification that the CDA beam is centered on the aperture mask spot for each point. The “Calibration” refers to points where the CDA was calibrated. This is typically done once the spread of CDA spots is decreasing to ensure accurate results over the smaller distances on the CDA detector.

B.1 CDA Alignment Trial 1 Movements

The “Verify Results” entries were used to check the alignment results. The variation in them is due to the dynamic error noise of the spots causing random error motions during measurements.

Table B-2. Alignment steps for CDA alignment trial 1

Step	Spot Movement	Channel	+/-	Voltage Change	Channel	+/-	Voltage Change	r _{RMS} (arcsec)	r _{RMS} (mm)
1	14	B1	+	3.0	U1	-	3.0	11.043	0.5924
2	3	B5	+	5.0	U5	-	5.0	8.696	0.4665
3	12	B2	+	3.0	U2	-	3.0	5.146	0.2760
4	3	B5	+	1.0	U5	-	1.0	3.822	0.2050
5	3	B5	+	1.0	U5	-	1.0	2.814	0.1509
6	Adjust Mask							2.527	0.1355
7	6	B4	-	1.0	U4	+	1.0	2.529	0.1356
8	3	B5	+	1.0	U5	-	1.0	1.867	0.1001
9	3	B5	+	0.5	U5	-	0.5	1.734	0.0930
10	12	B2	+	0.5	U2	-	0.5	1.707	0.0916
11	14	B1	-	0.5	U1	+	0.5	1.465	0.0786
12	13	B1	-	0.5	U1	+	0.5	1.274	0.0683
13	Adjust Mask							2.096	0.1125
14	9	B3	-	1.0	U3	+	1.0	1.352	0.0725
15	7	Calibration						1.370	0.0735
16	14	B1	-	0.3	U1	+	0.3	1.193	0.0640
17	6	B4	-	0.5	U4	+	0.5	1.628	0.0873
18	12	B2	-	0.5	U2	+	0.5	1.054	0.0566
19	Adjust Mask							0.789	0.0423
20	Verify Results							0.816	0.0438
21	Verify Results (2)							0.664	0.0356

B.2 CDA Alignment Trial 2 Movements

The second trial showed a significantly higher number of steps as this was also used for experimentation in the effects of different actuator movements, as is seen in the first few steps and several others in which differential movements were not utilized.

Table B-3. Alignment steps for CDA alignment trial 2

Step	Spot Movement	Channel	+/-	Voltage Change	Channel	+/-	Voltage Change	r _{RMS} (arcsec)	r _{RMS} (mm)	
1	13,14	B1	+	1.0	U1	+	1.0	15.813	0.8482	
2	13,14	B1	+	7.0	U1	+	7.0	16.326	0.8757	
3	13,14	B1	+	11.0	U1	+	7.0	15.461	0.8293	
4	3	B5	-	2.0	U5	+	2.0	14.917	0.8001	
5	12	B2	+	2.0	U2	-	2.0	13.155	0.7056	
6	10	B3	-	2.0	U3	+	2.0	11.995	0.6434	
7	9,10	B3	-	4.0	U3	+	4.0	12.016	0.6445	
8	9,10	B3	-	3.0	U3	+	3.0	12.370	0.6635	
9	10	B3	-	3.0	U3	+	3.0	12.243	0.6567	
10	10	B2	-	2.0	U2	+	2.0	14.281	0.766	
11	10	B2	-	0.0	U2	+	3.0	16.149	0.8662	
12	3	B5	-	2.0	U5	+	2.0	14.790	0.7933	
13	4	B4	-	4.0	U4	+	4.0	11.190	0.6002	
14	3	B5	-	2.0	U5	+	2.0	9.476	0.5083	
15	4	B4	+	2.0	U4	-	2.0	10.869	0.583	
16	3	B5	-	3.0	U5	+	3.0	9.055	0.4857	
17	14	B1	+	6.0	U1	+	1.0	3.607	0.1935	
18	3	B5	-	1.0	U5	+	1.0	2.933	0.1573	
19	4	B4	-	0.5	U4	+	0.5	2.588	0.1388	
20	14	B1	+	0.5	U1	-	0.5	1.713	0.0919	
21	14	B1	+	0.5	U1	-	0.5	1.434	0.0769	
22	3	B5	-	0.5	U5	+	0.5	1.288	0.0691	
23	6	B4	-	0.5	U4	+	0.5	1.214	0.0651	
24	7	Calibration							1.419	0.0761
25	14	B1	-	0.3	U1	+	0.3	1.316	0.0706	
26	13,14	B2	-	0.3	U2	+	0.3	1.318	0.0707	
27	6	B4	-	0.3	U4	+	0.3	1.167	0.0626	
28	14	B1	-	0.3	U1	+	0.3	1.275	0.0684	
29	14	B1	-	0.3	U1	+	0.3	1.093	0.0586	
30	10	B2	-	-	U2	+	0.2	1.072	0.0575	
31	3	B5	-	0.3	U5	+	0.3	1.238	0.0664	
32	3	B5	-	0.3	U5	+	0.3	0.919	0.0493	
33	10,12	B2	+	0.3	U2	+	0.1	0.887	0.0476	
34	14	B1	-	0.2	U1	+	0.2	1.053	0.0565	
35	10,12	B2	+	0.4	U2	+	0.1	0.801	0.043	
36	14	B1	-	0.5	U1	+	0.4	0.744	0.0399	
37	10	B2	+	0.1	U2	+	0.1	0.973	0.0522	
38	3	B5	-	0.2	U5	+	0.2	0.981	0.0526	
39	4	B4	+	0.2	U4	-	0.1	0.759	0.0407	
40	4	B4	+	0.3	U4	-	0.3	0.835	0.0448	

Appendix C: Wiring Schematic for PPI and PPII Actuators

The following wiring schematic was used to allow for the differential voltage control of ten piezoelectric bending actuators with the use of eleven power supplies during the testing of PPI. Each channel contains a switch which may be used to cut all voltage to an individual actuator. While this wiring setup is fairly simple, it provides a starting point for the design of an integrated circuit within an alignment strut frame which could be utilized to control a large number of piezoelectric actuators within an assembly which could eliminate the substantial wiring that is currently necessary. The input to the piezoelectric bending actuators is given by the constant voltage (+_c), adjustable voltage (+), and common ground (-).

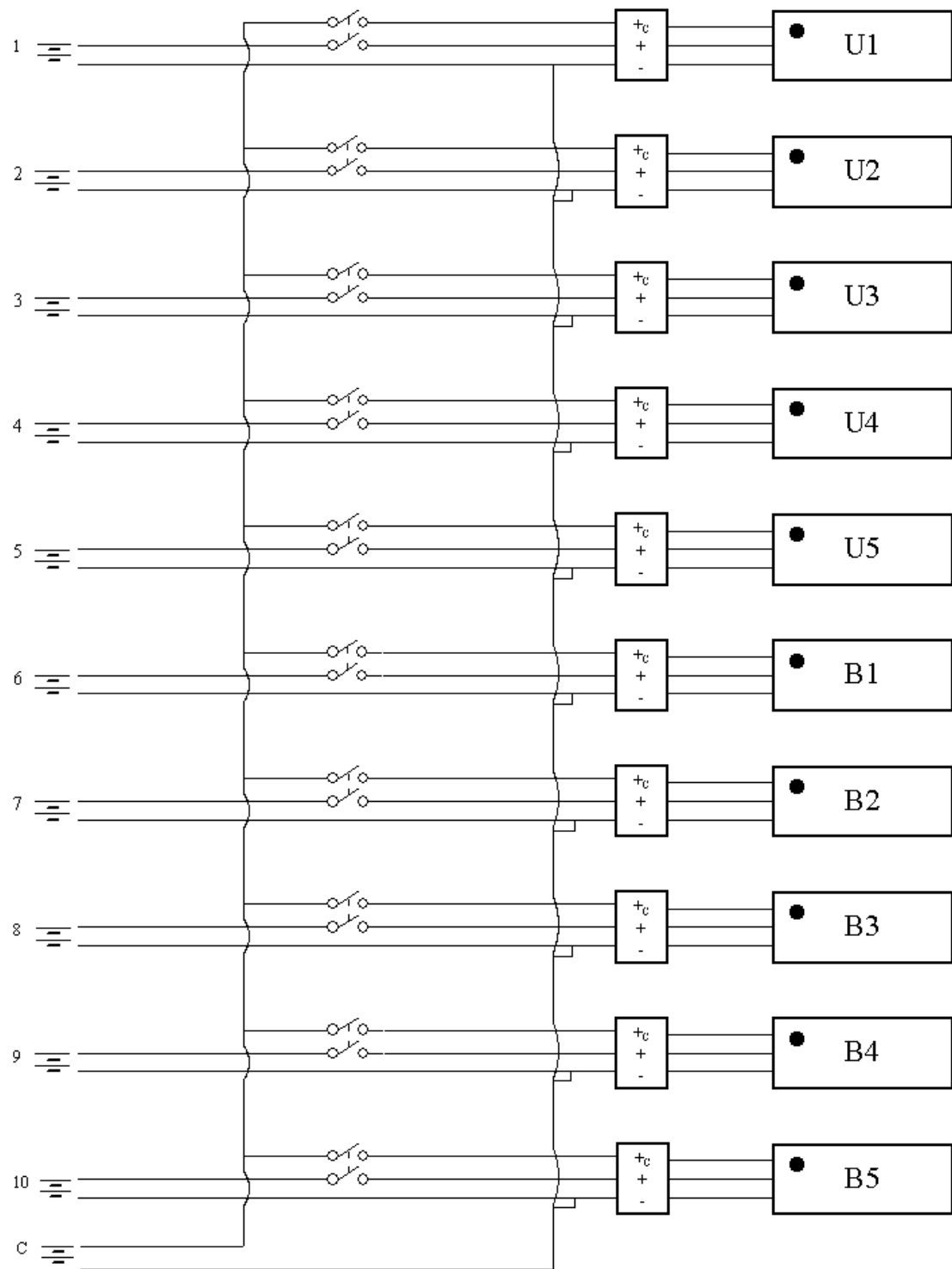


Figure C-1. Wiring schematic for PPI and PPII piezoelectric bending actuators

Appendix D: Finite Element Analysis for Azimuthal Stiffness [60]

Due to the geometry of the reflectors, the stiffness opposing the actuator varies for different actuation points. Finite element analysis is used to determine the stiffness by determining the amount of force necessary to move an azimuthal point a certain radial distance. For modeling, it is assumed that the stiffness is linear over the small distance (63.5 μm). In addition, symmetry about the center azimuth is assumed for the 50 degree mirror segment. The mechanical properties of Schott D-263 glass are used. The constraints imposed on the displaced position and the remaining actuation points have a large effect on the results. Table D-1 gives the constants used for the analysis.

Table D-1. Constants used for finite element analysis

Term	Value
Modulus of Elasticity (GPa)	72.9
Poisson's Ratio	0.208
Total Segment Azimuth (degrees)	50
Top Segment Radius (mm)	246.620523
Bottom Segment Radius (mm)	242.202272
Axial Length (mm)	200
Reflector Thickness (mm)	0.400
Radial Movement Distance (μm)	63.5

For the analysis, the displaced position has no additional constraints, which is assuming that the mirror interface tips are not clamping the mirror. All other points are constrained in the three translational degrees of freedom. Table D-2 gives the results for the analysis.

Table D-2. Mirror segment stiffness results for finite element analysis

Location	θ (°)	Force (lbf)	Force (N)	$k_{g\theta}$ (N/m)
B1	-24.50	4.180E-05	0.00019	2.93
B2	-12.25	1.441E-03	0.00641	100.94
B3	0	1.571E-03	0.00699	110.05
B4	12.25	1.441E-03	0.00641	100.94
B5	24.50	4.180E-05	0.00019	2.93
U1	-24.50	4.053E-05	0.00018	2.84
U2	-12.25	1.395E-03	0.00621	97.72
U3	0	1.520E-03	0.00676	106.48
U4	12.25	1.395E-03	0.00621	97.72
U5	24.50	4.053E-05	0.00018	2.84

REFERENCES

- [1] Mattson, Barbara. Official NASA Constellation-X Home Page. 2 Nov 2004. NASA Goddard Space Flight Center. 8 May 2005 <<http://constellation.gsfc.nasa.gov/>>.
- [2] Weisskopf, M.C., et al. "Chandra X-Ray Observatory (CXO): Overview." Proc. SPIE 4012 (2000): 2-16.
- [3] White, Nicholas E., et al. "The Science Goals of the Constellation-X Mission." Proc. SPIE 5488 (2004): 382-387.
- [4] Petre, Robert, et al. "Recent Progress on the Constellation-X Spectroscopy X-Ray Telescope (SXT)." Proc. SPIE 5168 (2004): 196-206.
- [5] Hailey, Charles J., et al. "Fabrication and Performance of Constellation-X Hard X-ray Telescope Prototype Optics Using Segmented Glass." Proc. SPIE 5168 (2004): 90-99.
- [6] Kelley, R.L. "The X-Ray Microcalorimeter Spectrometer for the Constellation-X Mission." HEAD (2003), #35, 22.06
- [7] McEntaffer, R., W. Cash, and A. Shipley. "Off-plane gratings for Constellation-X." Proc. SPIE 4851 (2003): 549-556.
- [8] Saha, Timo T., and William Zhang. "Equal-curvature grazing-incidence x-ray telescopes." Applied Optics 42 (2003): 4599-4605.
- [9] Saha, Timo T., David A. Content, and William W. Zhang. "Equal-curvature x-ray telescope designs for Constellation-X mission." Proc. SPIE 5168 (2004): 346-351.
- [10] Zhang, William, et al. "Development of X-Ray Reflectors for the Constellation-X Observatory." Proc. SPIE 5168 (2004): 168-179.
- [11] Zhang, William, et al. "Development of lightweight X-Ray mirrors for the Constellation-X mission." Proc. SPIE 5488 (2004): 820-828.
- [12] Podgorski, William A., et al. "Constellation-X Spectroscopy X-ray Telescope Assembly and Alignment." Proc. SPIE 4851 (2003): 491-502.
- [13] Petre, Robert, et al. "The Constellation-X Spectroscopy X-Ray Telescope." Proc. SPIE 5488 (2004): 505-514.
- [14] Vorndran, Stefan, ed. "Tutorial: Piezoelectrics." Physik Instrumente: MicroPositioning, NanoPositioning, NanoAutomation Product Catalog. Karlsruhe: PI, 2001.
- [15] Huang, C., Y. Y. Lin, and T.A. Tang. "Study on the tip-deflection of a piezoelectric bimorph cantilever in the static state." J. Micromech. Microeng. 14 (2004): 530-534.
- [16] Thor Labs, Inc. 435 Route 206 North, Newton, NJ 07860.

- [17] Awtar, Shorya. “Synthesis and Analysis of Parallel Kinematic XY Flexure Mechanisms.” Ph. D. Thesis. Massachusetts Institute of Technology. Cambridge, MA, 2004.
- [18] Cohen, L. “Segmented Optics #1” Smithsonian Astrophysical Observatory Memorandum to the NASA/GSFC Constellation-X SXT Design Team. 4 Feb 1999.
- [19] Cohen, L. “Segmented Optics #2” Smithsonian Astrophysical Observatory Memorandum to the NASA/GSFC Constellation-X SXT Design Team. 17 Feb 1999.
- [20] Soong, Yang, Kai-Wing Chan, and Peter J. Serlemitsos. “Recent advance in segmented thin-foil X-ray optics.” Proc. SPIE 4496 (2002): 54-61.
- [21] Newman, Phil. Suzaku Guest Observer Facility. 4 Oct 2005. NASA Goddard Space Flight Center. 30 Oct 2005
<<http://heasarc.gsfc.nasa.gov/docs/astroe/astroegof.html>>.
- [22] Monnelly, Glen P., et al. “High-Accuracy X-ray Foil Optic Assembly.” Proc. SPIE 4138 (2000): 164-173.
- [23] Bergner, Henry W., Jr., et al. “Precision Assembly Station for High Resolution Segmented Optics.” Proc. SPIE 4138 (2000): 134-146.
- [24] Forest, Craig Richard. “X-ray Telescope Foil Optics: Assembly, Metrology, and Constraint.” Master’s Thesis. Massachusetts Institute of Technology. Cambridge, MA, 2003.
- [25] Hair, Jason H., et al. “Constellation-X Soft X-Ray Telescope Segmented Optic Assembly and Alignment Implementation.” Proc. SPIE 4851 (2003): 696-707.
- [26] Owens, Scott M., et al. “The Constellation-X SXT Optical Alignment Pathfinder 2 – Design, Implementation, and Alignment.” Proc. SPIE 5168 (2004): 239-247.
- [27] Davis, William N. “Constellation-X SXT Engineering Unit Mechanical Status: Effect of moving 2 outboard struts inline with the optical axis.” E-mail from Smithsonian Astrophysical Observatory to NASA/GSFC Constellation-X SXT Design Team. 24 Sep 2003.
- [28] Podgorski, W. and Davis, W. “Finite Element Results from OAP2 Model Update, December 2002.” Smithsonian Astrophysical Observatory Memorandum to NASA/GSFC Constellation-X SXT Design Team. 8 Dec 2002.
- [29] Tiodize Co., Inc. 5858 Engineer Drive, Huntington Beach, CA 92649.
- [30] Boyer, Howard E. and Timothy L. Gall, eds. Metals Handbook: Desk Edition. Metals Park: American Society for Metals, 1985.
- [31] Sovinski, M. “Coefficient of Thermal Expansion (CTE) Analysis of Titanium 15% Mo Alloy.” Materials Engineering Branch Code 541 Laboratory Report for the James

Webb Space Telescope Design Team. NASA-Goddard Space Flight Center.
Greenbelt, MD. 9 Jun 2004.

- [32] Allvac. 2020 Ashcroft Avenue, Monroe, NC 28110 USA.
- [33] Swiss Jewel Company. "Synthetic Sapphire Properties." 325 Chestnut St. , Constitution Place No. 509, Philadelphia, PA 19106 USA.
- [34] Schott North America. 555 Taxter Road, Elmsford, NY 10523, USA.
- [35] "Glass D263: Thermal expansion without shrinkage correction." Materials Analysis Report. Schott North America. 14 Jul 1997.
- [36] Vallance, R. Ryan, Morgan, Chris, and Slocum, Alexander H. "Precisely positioning pallets in multi-station assembly systems." Precision Engineering 28 (2004): 218-231.
- [37] Varshneya, Arun A. Fundamentals of Inorganic Glasses. San Diego: Academic Press, Inc., 1994.
- [38] He, Charles and Len Wang. "Strength of slumped glass shells for Constellation-X." NASA-GSFC. Code 541. 17 Dec 2003.
- [39] Korn, Granino and Theresa Korn. Mathematical Handbook for Scientists and Engineers. Second Edition. New York: McGraw-Hill, 1968.
- [40] Johnson, K.L. Contact Mechanics. Cambridge: Cambridge University Press, 1985.
- [41] Hii, King-Fu. "Kinematically Constrained Spindles." Master's Thesis. University of Kentucky. Lexington, KY, 2002.
- [42] Slocum, Alexander H. Precision Machine Design. Englewood Cliffs: Prentice Hall, 1992.
- [43] Smith, S.T. and D.G. Chetwynd. Foundations of Ultraprecision Mechanism Design. Philadelphia: Gordon and Breach, 1992.
- [44] Pilkey, Walter D. Formulas for Stress, Strain, and Structural Matrices. 2nd Edition. Hoboken: Wiley & Sons, 2005.
- [45] Smith, S.T, D.G. Chetwynd, and D.K. Bowen. "The design and assessment of high precision monolithic translation mechanisms." J. Phys. E: Sci. Instrum. 20 (1988): 977-983.
- [46] Becker, P., P. Seyfried, and H. Siegert. "Translation stage for a scanning x-ray optical interferometer." Rev. Sci. Instrum 58 (1987): 207-211.
- [47] Smith, Stuart T. Flexures: Elements of Elastic Mechanisms. Amsterdam: Gordon and Breach, 2000.

- [48] Weinberg, Marc S. "Working equations for piezoelectric actuators and sensors." ASME/IEEE Journal of Microelectromechanical Systems 8.4 (1999): 529-533.
- [49] Bickford, John H. and Sayed Nassar, eds. Handbook of Bolts and Bolted Joints. New York: Marcel Dekker, 1998.
- [50] Noliac A/S. Hejreskovvej 18, Kvistgaard DK-3490, Denmark.
- [51] O'Dell, Stephen L., et al. "X-ray testing Constellation-X optics at MSFC's 100-m facility." Proc. SPIE 5168 (2004): 306-317.
- [52] Saha, Timo T. Personal communications. NASA-GSFC. Code 551. 7 Sep 2005.
- [53] Owens, Scott M. Personal communications. NASA-GSFC. Code 551. 30 Aug 2005.
- [54] Chan, Kai-Wing. "DiffractionCal_051109." NASA-GSFC. Code 662. 9 Nov 2005.
- [55] Glenn, Paul. "Centroid detector assembly for the AXAF-I alignment test system." Proc. SPIE 2515 (1995): 352-360.
- [56] Glenn, Paul. "Alignment System Performance Analysis." Letter to Bill Podgorski and Bob Rasche. 23 Oct 2002.
- [57] Content, David, et al. "Optical metrology for the segmented optics on the Constellation-X Soft X-ray telescope." Proc. SPIE 5168 (2004): 207-218.
- [58] Content, David, et al. "Optical metrology for the segmented optics on the Constellation-X spectroscopy x-ray telescope." Proc. SPIE 5488 (2004): 272-282.
- [59] Podgorski, William A., et al. "Constellation-X spectroscopy x-ray telescope optical assembly pathfinder image error budget and performance prediction." Proc. SPIE 5168 (2004): 318-333.
- [60] Squires, Janet. "494 Secondary Reflector Analysis." Swales Aerospace. 2 Nov 2005.